OUKA
The University of Osaka
Institutional Knowledge Archive

Title	Study of Laser Ablation Mechanism and Its Application to the Formation of Multilayered Oxide Thin Films
Author(s)	西川, 博昭
Citation	大阪大学, 1998, 博士論文
Version Type	VoR
URL	https://doi.org/10.11501/3143753
rights	
Note	

The University of Osaka Institutional Knowledge Archive : OUKA

https://ir.library.osaka-u.ac.jp/

The University of Osaka

Study of Laser Ablation Mechanism and Its Application to the Formation of Multilayered Oxide Thin Films.

Dissertation
Submitted to the Department of Chemistry,
Osaka University
for the Degree of Doctor of Science

January 1998

The Institute of Scientific and Industrial Research
Osaka University

Hiroaki NISHIKAWA

Contents.

General Introduction. 1.

Chapter 1

Mechanism of Excimer Laser Ablation for Metal. 13.

Abstract 14.

1-1. Introduction. 15.

1-2. Experimental. 17.

1-3. Results and Discussion. 22.

1-3-1. The TOF spectra and the amount of the desorbed monovalent ion on the laser ablation of alkaline earth metal. 22.

1-3-2. The influence of the variation of the effective pulse duration by using double pulsed laser ablation technique. 34.

1-3-3. General remarks and the consideration on the mechanism of the laser ablation for the metallic bond crystal. 41.

1-4. Conclusion. 47.

References 49.

Chapter 2

Surface Morphology of Oxide Thin Film Crystals Grown by Laser Molecular Beam Epitaxy. 52.

Abstract 53.

2-1. Introduction. 54.

2-2. Experimental. 56.

2-3. Results and Discussion. 58.

2-3-1. $SrTiO_3(100)$ substrate. 58.

2-3-2. Heteroepitaxial growth of $CaTiO_3$ on atomically flat $SrTiO_3(100)$ surface. 61.

2-3-3. Growth of $La_{0.7}Sr_{0.3}MnO_3$ and $La_{0.7}Sr_{0.3}MnO_3/CaTiO_3$ bilayer on atomically flat $SrTiO_3(100)$ surface. 69.

2-3-4. In-situ monitoring of SrO growth on the atomically flat $SrTiO_3(100)$ surface. 72.

2-4. Conclusion. 81.

References 82.

Chapter 3

Measurements of Bloch Wall Width via Transport Property in Multilayered System of $CoFe_2O_4/Fe_3O_4/CoFe_2O_4$ Thin Film Crystals. 84.

Abstract 85.

3-1. Introduction. 86.

3-2. Experimental. 92.

3-3. Results and Discussion. 93.

3-3-1. Structures and properties of Fe_3O_4 and $CoFe_2O_4$ single layered thin film crystals. 93.

3-3-2. The magnetic and magnetotransport properties of the trilayered system of $CoFe_2O_4/Fe_3O_4/CoFe_2O_4$ thin film crystal. 100.

3-4. Conclusion. 106.

References 107.

Chapter 4

General Conclusion. 109.

Acknowledgments. 113.

List of Publications. 114.

Appendix A

The Proposed Models for UV Laser Ablation Mechanism. 115.

A-1. Ionic Bond Crystal. 116.

A-2. Covalent Bond Crystal. 118.

A-3. Metallic Bond Crystal. 120.

References 122.

Appendix B

Observation of Thin Film Growth by Using RHEED. 123.

B-1. RHEED Pattern of the Typical Surfaces. 124.

B-2. Typical Growth Modes of Thin Film Crystals and Intensity Oscillation of RHEED Specular Spot. 127.

References 131.

General Introduction.

When the high density laser pulse is focused onto solid, the surface layer of the solid (called *target*) decomposes expansively into atoms, ions, molecules and clusters (Fig. 1). Such decomposition is called "laser ablation". By the application of the ultraviolet (UV) laser ablation as "pulsed laser deposition (PLD) technique", thin film crystals of various materials have been fabricated in the last decade [1]. Especially, multi-element oxides have been widely prepared by the PLD technique because of the features of this method, i.e.,

1. The stoichiometry between the grown film and the target agrees well. It is effective for the construction of multi-element systems.
2. It is possible to use in oxidation atmosphere for the crystal growth since the laser beam can pass through it. It is useful for the preparation of oxide crystals.

On these backgrounds, the PLD technique has been rapidly developed as one of the most powerful preparation method for the single crystals of oxide thin film.

During the development of the PLD technique, the characteristic features of the laser ablation phenomenon to be solved have been recognized. Namely, the fundamental process of the UV laser ablation in many materials

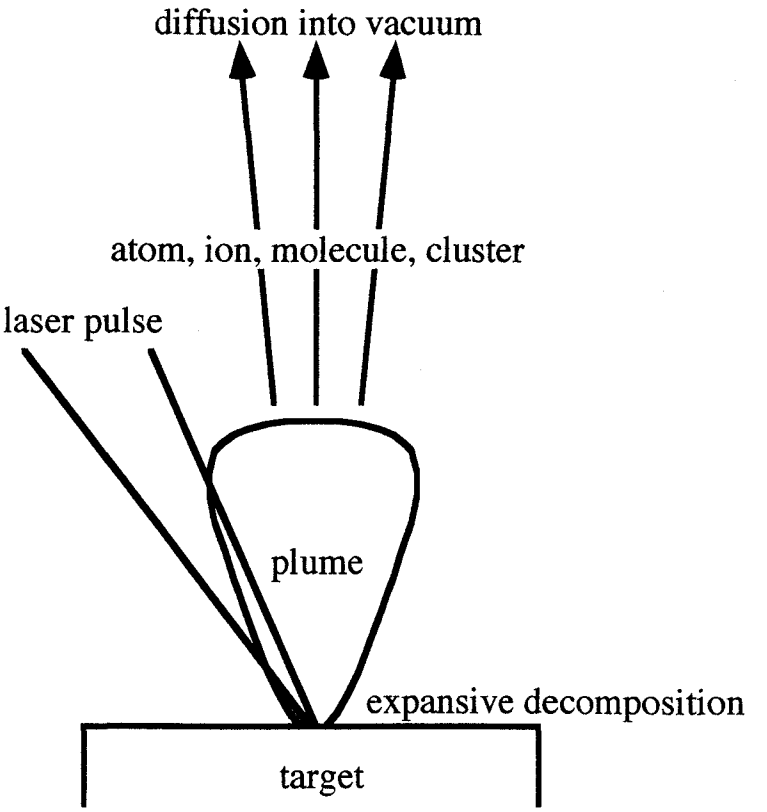

Fig. 1 The schematic illustration of the laser ablation phenomenon.

is not simple thermal evaporation [2] but photochemical reaction [3]. This recognition has made the study of the laser ablation mechanism be important as a new subject in the field of the photochemistry. The mechanism is, however, complicated because the phenomenon is a transient process caused in very small area. Furthermore, this phenomenon involves complex physical processes governed by so many parameters such as wavelength, pulse duration and fluence of the laser and irradiated material itself [2, 3]. The goal of this study as a subject of the photochemistry seems to be understood mainly two processes. One is the excitation process and the other is the energy transfer process to the translation energy of the chemical species (see Fig. 2). The problems to be answered are summarized as follows.

1. Which system in the solid state target is directly excited by the incident photon?
2. What is the final state after the excitation?
3. What does occur during the relaxation process and how is the relationship between this relaxation and the driving force of the desorption?

With respect to these problems, the mechanisms for ionic and covalency crystal have been understood [4-7], while that for metal has still problems in

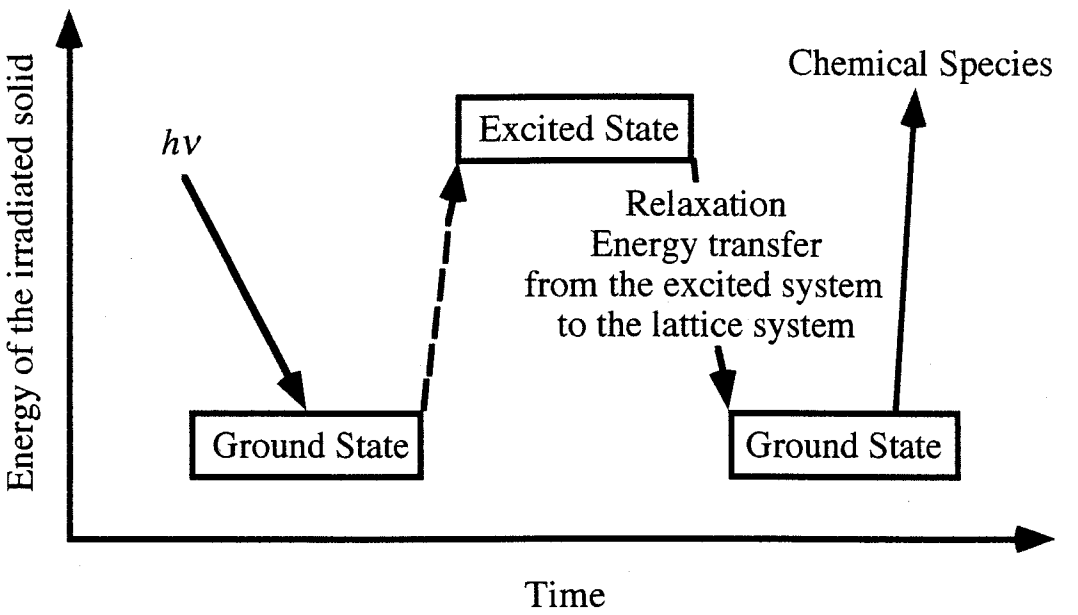

Fig. 2 The schematic profile of the laser ablation phenomenon separated into each elementary process. The vertical and horizontal axes are energy of the system and time, respectively. The target irradiated by photon is excited from the ground state. The energy of the excited state is transferred into lattice system during the relaxation process.

the proposed model based on not only the simple thermal evaporation model [8, 9] but also various electronic excitation models [10, 11]. The proposed model for the laser ablation mechanism is presented at Appendix A in order to introduce the details of the models proposed previously. The most serious problem seems that the initial stage of the excitation has not been understood clearly. Thus, the laser ablation mechanism of the metal is investigated in the present work.

The formation of the thin film crystals of transition-metal oxides is one of the popular applications for the laser ablation phenomenon as mentioned above. Since the discovery of high T_c superconductor [12], the transition-metal oxides have been quite noted because of their functional properties, such as di- and ferroelectricities and magnetic properties. Generally, many of those functional oxides have similar crystal structures, i.e., "perovskite type structure (Fig. 3)". This similarity is convenience for epitaxial growth of heterostructure system with the various functional oxides. Thus, the recent trends have been the studies of superlattice or multilayered system of oxide materials on the concept that the interlayer interaction, e.g., lattice strain [13], interlayer exchange interaction [14] and so on, is utilized and controlled. In the growth of the superlattice or multilayered oxide system, it is important to control the surface (interface) flatness on the atomic level. The randomness on the surface (interface) causes disorder of the lattice coherency which is the most important for the

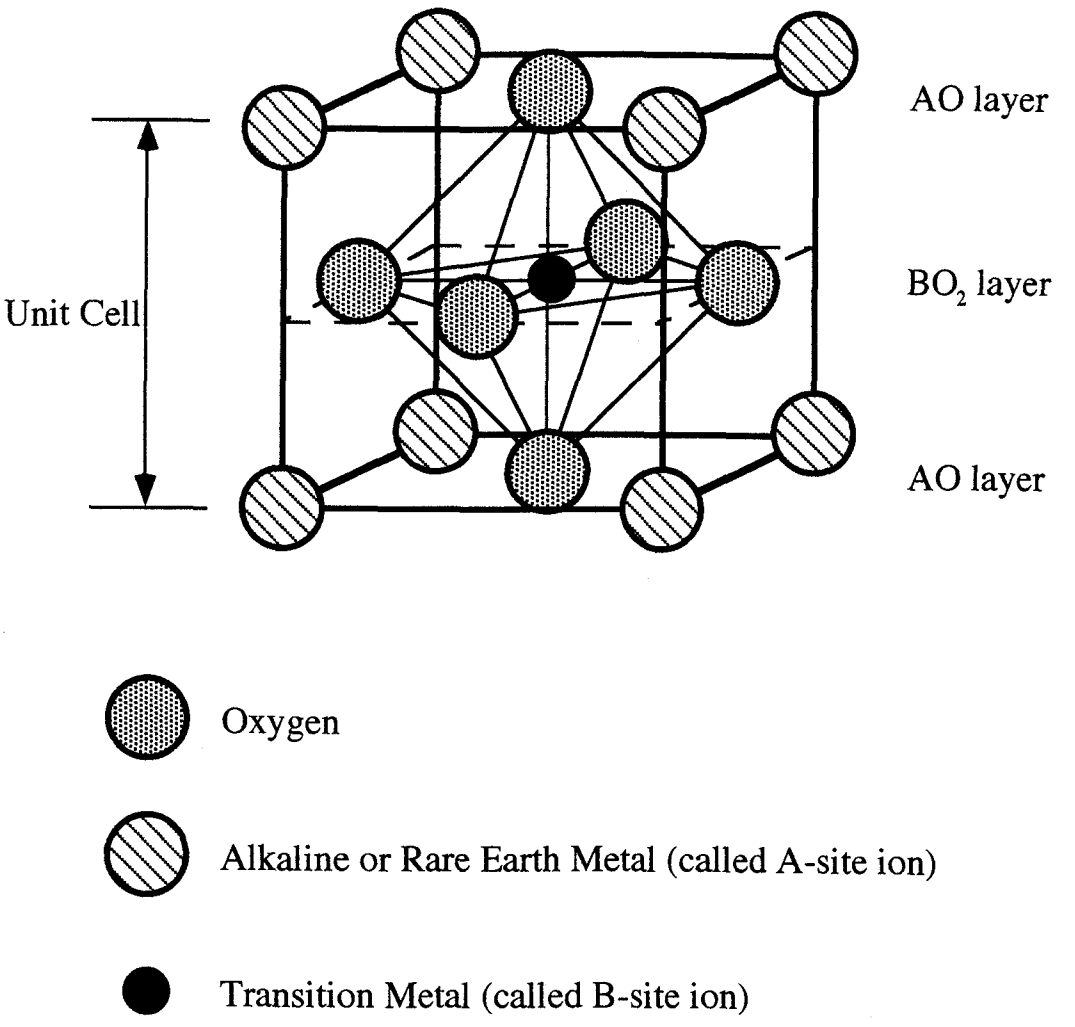

Fig. 3 The schematic illustration of the perovskite type structure.

superlattice. The randomness also disturbs the electronic potential and band structure which govern the various electronic properties of material. Namely, the intrinsic electronic properties in such system may be screened by the surface randomness. In the oxide materials, however, the growth technique is not enough developed in the present stage compared with that in the semiconducting materials [15]. The difference of the oxide crystals from the semiconducting materials is the ionic character including many elements. The typical semiconducting materials, the nature of the chemical bond is covalency and only two or three kinds of element are included. The important factors are elucidated concerning above difference in order to keep the surface flatness with the atomic level for the transition-metal oxides of the perovskite type structure.

As one of the examples for the result on the realization of the surface flatness, the control of the spin configuration in magnetic materials will be possible taking advantage of the superexchange interaction at the interface of the multilayered oxide system. The spin ordering states of many oxides are governed by the superexchange interaction between two metal ions via an oxygen ion. This interaction can work between two metal ions beyond the interface. The spin ordering state will be propagated from the interface to the inside of the layer via the superexchange interaction between each metal ion. Thus, the superexchange interaction ordering the spin in a layer can affect the whole

spin ordering state in the other layer beyond the interface. Since this interaction is short range correlation [16], the atomically flat interface is needed. While the studies on the spin configuration has been performed by the superlattice system of ferromagnetic metals [17-21], similar studies by the oxide system has a following merit. Namely, the combination of the various magnetic materials with the similar crystal structure is available, i.e., ferro-, ferri-, antiferro-, soft, hard, conductive and insulative magnets. In the study of such artificial spin control, the propagation manner in the inside of the crystal should be clarified, i.e., the detail of the spin configuration in the crystal in order to control completely. The subject has, however, not been enough revealed because the typical methods for magnetic measurement are difficult to "observe" the spin configuration in the inside of the crystal directly. The multilayered oxide system consisting of such various functional materials may make new study be possible for the spin configuration. In this work, the variation of the spin configuration from the interface to the inside of the crystal is studied via the transport property with the multilayered oxide system of insulative and conductive ferrimagnets.

The contents of this thesis are following. In chapter 1, the mechanism of the laser ablation for alkaline earth metal is investigated in order to understand the process systematically. In chapter 2, the important factors are clarified to maintain the surface flatness with the

atomic level. In chapter 3, the measurement of the spin configuration in the inside of the crystal is examined via transport properties. Finally, these investigations are summarized in chapter 4.

References

[1] K. L. Saenger: *Pulsed Laser Deposition of Thin Films*, eds. D. B. Chrisey and G. K. Hubler (John Wiley & Sons, Inc., New York, 1994), Appendix, p. 582.

[2] N. Bloembergen: *AIP Conf. Proc. 288*, eds. J. C. Millor and D. B. Geohegan (American Institute of Physics, New York, 1994) p. 3.

[3] R. Kelly and A. Miotello: *Pulsed Laser Deposition of Thin Films*, eds. D. B. Chrisey and G. K. Hubler (John Wiley & Sons, Inc., New York, 1994), p. 55.

[4] M. L. Knotek and P. J. Feibelman: Phys. Rev. Lett. **40** (1978) 964.

[5] R. L. Webb, L. C. Jensen, S. C. Langford and J. T. Dickinson: J. Appl. Phys. **74** (1993) 2323.

[6] N. Itoh and T. Nakayama: Phys. Lett. A **92** (1982) 471.

[7] M. L. Knotek: *PHYSICS TODAY SEPTEMBER 1984* (1984) 24.

[8] A. Vertes, R. W. Dreyfus and D. E. Platt: IBM J. Res. Develop. **38** (1994) 3.

[9] R. Kelly, J. J. Cuomo, P. A. Leary, J. E. Rothenberg, B. E. Braren and C. F. Aliotta: Nucl. Instrum. & Methods B **9** (1985) 329.

[10] I. Lee, J. E. Parks II, T. A. Callcott and E. T. Arakawa: Phys. Rev. B **39** (1989) 8012.

[11] H. Helvajian and R. Welle: J. Chem. Phys. **91** (1989) 2616.

[12] J. G. Bednorz and K. A. Müller: Z. Phys. B **64** (1986) 189.

[13] For example, H. Tabata, T. Kawai and S. Kawai: Phys. Rev. Lett. **70** (1993) 2633.

[14] For example, Y. Suzuki, R. B. van Dover, E. M. Gyorgy, J. M. Phillips and R. J. Felder: Phys. Rev. B **53** (1996) 14016.

[15] Y. Shiraki: *Physics and the Application of Semiconductor Superlattices*, ed. The Physical Society of Japan (Baifu-kan, Tokyo, 1984), p. 108 [in Japanese].

[16] J. Kanamori: *Magnetism* (Baifu-kan, Tokyo, 1969), p. 53 [in Japanese].

[17] M. N. Baibich, J. M. Broto, A. Fert, F. N. V. Dau, F. Petroff, P. Eitenne, G. Creuzet, A. Friederich and J. Chazelas: Phys. Rev. Lett. **61** (1988) 2472.

[18] G. Binasch, P. Grünberg, F. Saurenbach and W. Zinn: Phys. Rev. B **39** (1989) 4828.

[19] T. Ono and T. Shinjo: J. Phys. Soc. Jpn. **64** (1995) 363.

[20] S. S. P. Parkin, N. More and K. P. Roche: Phys. Rev. Lett. **64** (1990) 2304.

[21] J. Unguris, R. J. Celotta and D. T. Pierce: Phys. Rev. Lett. **67** (1991) 140.

Chapter 1

Mechanism of Excimer Laser Ablation for Metal.

Abstract

The time-of-flight (TOF) distribution and the amount of the desorbed monovalent ion have been measured in the laser ablation of alkaline earth metal. The experiment is performed under the various laser condition, i.e., two kinds of wavelength (193nm by ArF excimer laser and 248nm by KrF excimer laser), fluence in the region of 0~500mJ/cm^2 and effective pulse width of 14ns~20ns. The ion desorption occurs with the lower fluence than the prediction of the thermal evaporation model. Furthermore, the temperature obtained by the fitting of TOF spectra to Maxwell-Boltzmann distribution corrected by the center-of-mass velocity is much higher than the prediction of the thermal model. The relationship between the amount of the desorbed ion and the fluence shows highly nonlinear behavior. In the case that the effective pulse width of ArF excimer laser is broadened from 14ns to 20ns for the ablation of Ca metal, the total amount of Ca^+ decreases to ~0.1 times. On the basis of the results, it is discussed that the laser ablation of the alkaline earth metal is caused by the core electron excitation with the multiphoton photochemical process.

1-1. Introduction.

The studies of the ultraviolet (UV) laser ablation mechanism is a new subject for photochemistry as the interaction between condensed matter and photon. In the last decade, the lack of sufficient study of the fundamental processes of the laser ablation has been masked by the success in applications of the phenomena for the thin film formation as pulsed laser deposition (PLD). It has been now revealed, however, that further progress in the control and optimization of PLD technique in order to improve the quality of the deposited films will require a deeper insight into the underlying fundamental phenomena that govern the laser ablation. Such recognition has made the studies be popular. This work is, however, complicated because the laser ablation is a transient process involving complex physics which is depending on several parameters such as the wavelength, pulse duration, fluence of the laser beam and the material irradiated by the laser (so called *target*). Obviously, classification by those parameters is needed in the studies. Since the laser ablation can be considered as the local breaking of the chemical bond, the process will strongly depend on the nature of the chemical bond. Thus, the largest class seems the difference of the bond character of each target.

On the classification by the nature of the chemical bond, there will be typical three classes, i.e., ionic bond crystal, covalent bond crystal and metallic bond crystal. The reliable model has been already proposed

for the former two classes (see Appendix A). In those crystals, the nascent process of the laser ablation has been concluded as not the thermal evaporation but the electronic excitation mechanism. The essential requirement in such model seems the localization of the electronic excited state. The mechanism for the metallic bond crystal is, however, not enough understood compared with other crystals. It is believed that the laser ablation of the metal is caused by the thermal evaporation [1]. So far, a lot of thermal evaporation mechanism has been proposed, e.g., the thermal evaporation with the solution of the one-dimensional heat-conduction equation [2], exfoliational sputtering with the thermal shock [3], hydrodynamic process with thermal melting [3], and so on. On the previous model (see Appendix A), it seems that the first stage of the ablation has not been understood. Generally, it has been considered that the free electron is accelerated by the absorption of photon via inverse Bremsstrahlung process [1, 2, 4]. The accelerated electron is scattered by the lattice and excites the phonon with the time scale of ~ps [1, 2, 4]. This means that the energy injected into the electronic system is transferred to the lattice system within ~ps. Such absorption is, however, not so effective for the irradiation of UV light to metal [5, 6]. Since the plasma cut-off frequency for almost all metals is on UV region, the metallic bond crystal well transmits the UV laser [7]. As the previous experimental results, it has been reported that the low fluence can cause the laser ablation that the

temperature does not reach the melting point [8] which value is calculated by the one-dimensional heat-conduction equation [2]. Therefore, it can be considered that the laser ablation mechanism of metal is not simple thermal evaporation process.

In order to consistently understand the process of the laser ablation for the metal, the author has systematically investigated the laser ablation of three alkaline earth metals, i.e., Ca, Sr and Ba. These metals belonging to the same group has similar chemical character, so the systematic experiments are possible by the comparison of the results. In this study, time-of-flight (TOF) distribution and the amount of monovalent ion desorbed by the laser ablation of the alkaline earth metal are investigated using time-resolved quadrupole mass spectrometer (QMS) with two kinds of wavelength and various values of fluence. Furthermore, the effective pulse duration is also varied by using double pulsed laser ablation technique with the time delay between two laser pulses in order to study the time scale of the process. On the basis of the experimental results, a new model is proposed for the laser ablation mechanism of the metal.

1-2. Experimental.

The schematic diagram of the experimental apparatus is shown in Fig. 1-1(a). The measurement of the desorbed monovalent ion was performed in a vacuum chamber with the base pressure of ~10^{-6}Pa. Plates

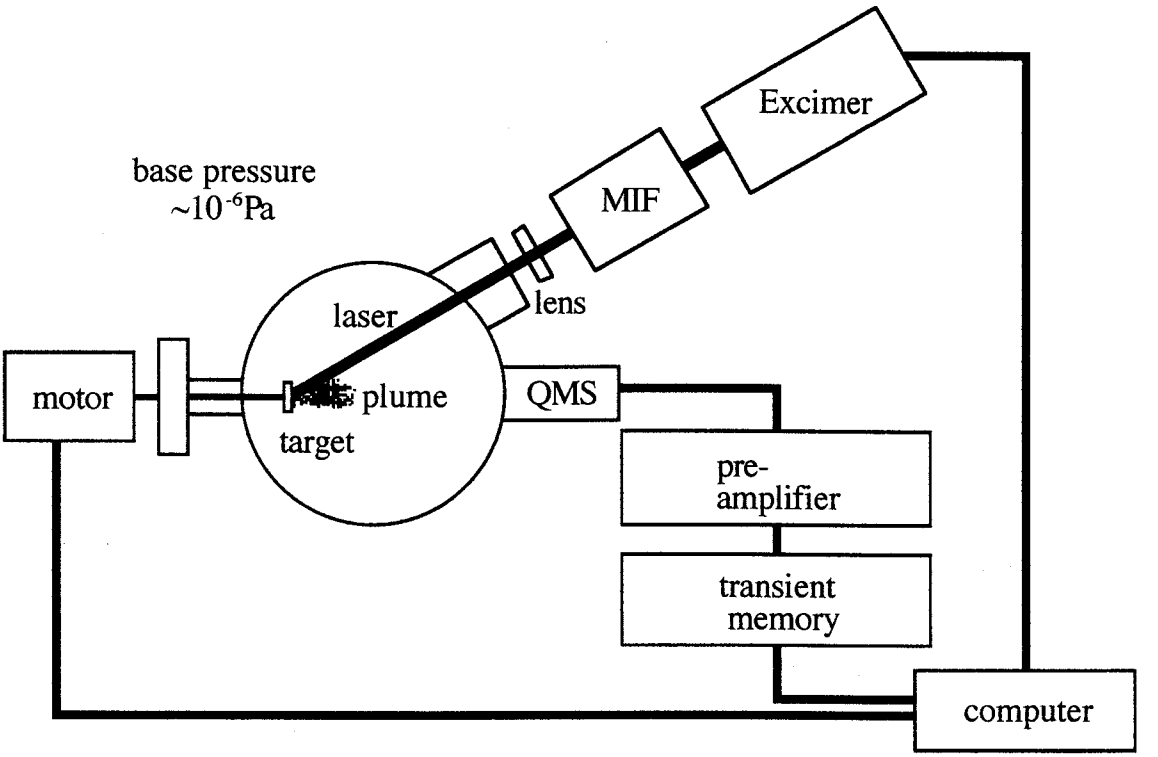

Fig. 1-1(a) The schematic diagram of the laser ablation experiments.

of Ca, Sr and Ba (Rare Metallic : polycrystalline with the purity of 99%) placed in the chamber were irradiated by an ArF excimer laser (Lumonics: EXCIMER-700, λ=193nm, FWHM of each pulse =14ns) or a KrF excimer laser (Lambda Physics: COMPEX-102, λ=248nm, FWHM of each pulse =14ns). The laser pulse was focused onto the target by an artificial silica lens with a focal length of 4.4×10^2mm (spot size of the focused beam on the target was ~2.0×0.7mm^2). The oxide layers on the plate surfaces were removed by the pre-ablation in the vacuum chamber before the measurements. The desorbed ion were detected by a QMS (VG Gas Analysis: SXP300). The distance between the target and the QMS was 5.4×10^2mm. The QMS signal was amplified by a preamplifier (NF Electronic Instruments: 5305, frequency response = DC~10MHz) and then stored in a transient memory devices (Kawasaki Electronica: MR-50E) with the sampling rate of 400ns. The zero point of the time axis was governed by a phototube (Hamamatsu Photonics: R1826, wavelength region of 185~320nm, response is much faster than ~ns) placed near the focusing lens. This means that the time delay can be negligible in the case that the sampling rate is 400ns. The sample was rotated between each laser shot by a stepping motor to ensure that the ablation was always performed on a fresh surface.

Double pulsed laser ablation technique was accomplished by two laser pulses with a various delay times between them. The two pulses were

obtained by producing two replicas of a single laser pulse in a Michelson interferometer (MIF) inserted between the excimer laser and the focusing lens. This technique makes effective pulse duration change without changing the total fluence. In the MIF, the laser beam with a fluence of 800mJ/cm^2 (this value was converted into the fluence on the target surface) was divided by a 50% beam splitter and reflected back by two 100% mirrors (Fig. 1-1(b)). Namely, the fluence of each pulse was 200mJ/cm^2 (note that the each laser pulse passes through twice the 50% beam splitter). The position of one of the mirrors (#1) was fixed while the other one was mounted on an optical rail with a maximum traveling distance of ~1m corresponding to a maximum delay of ~6ns between two pulses (The time delay was calculated from the mirror positions using $\Delta t = 2(l_2\text{-}l_1) / c$, where l_1 and l_2 are the distances between the beam splitter and the respective mirrors and c is the velocity of light).

In this experiment, special care was taken to ensure that only the delay between two pulses changed while all the other parameters remained constant. By blocking alternately one of the mirrors, it was checked whether pulses coming from the different arms of the MIF produced the same QMS signal. The losses or the focal spot diameter may change systematically as the optical path in the delayed arm changes. This may lead to serious systematic errors. In order to prevent errors, it was confirmed prior to the double pulsed measurements that the QMS signal

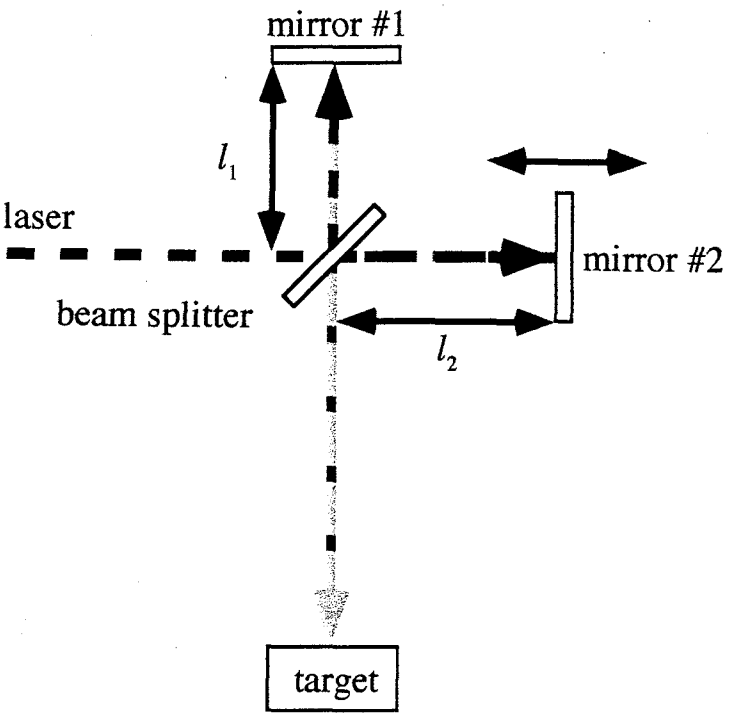

Fig. 1-1(b) The sketch of Michelson interferometer producing the two ablation pulses with various values of delay time.

produced by the beam coming from the moving mirror showing no measurable dependence on the mirror position. Changes in the overlap between the focal spots of the beams coming from the different arms of the MIF with the position of the moving mirror can be the most important source of error. This effect was eliminated for all mirror positions by consistently realigning the overlap between the spots. The realignment was accomplished with the help of a pinhole with a diameter of ~1mm that was set in front of the laser beam before it entered the MIF. Using above procedure, the lateral deviation of the two laser beams at the target surface was less than 5×10^{-2}mm. This value is the smallest scale of the ruler used in the experiment. Furthermore, the TOF spectra and the amount of the total desorbed ion did not vary depending on the mirror setup, i.e., the measurement by using only mirror #1, mirror #2 or the position of mirror #2.

1-3. Results and Discussion.

1-3-1. The TOF spectra and the amount of the desorbed monovalent ion on the laser ablation of alkaline earth metal.

Figures 1-2 and 1-3 show the TOF spectra of the monovalent ion desorbed by the ArF excimer laser ablation of Ca, Sr and Ba. The ion desorption in such fluence region can not be explained by the thermal evaporation model. It is proposed in the thermal evaporation model that

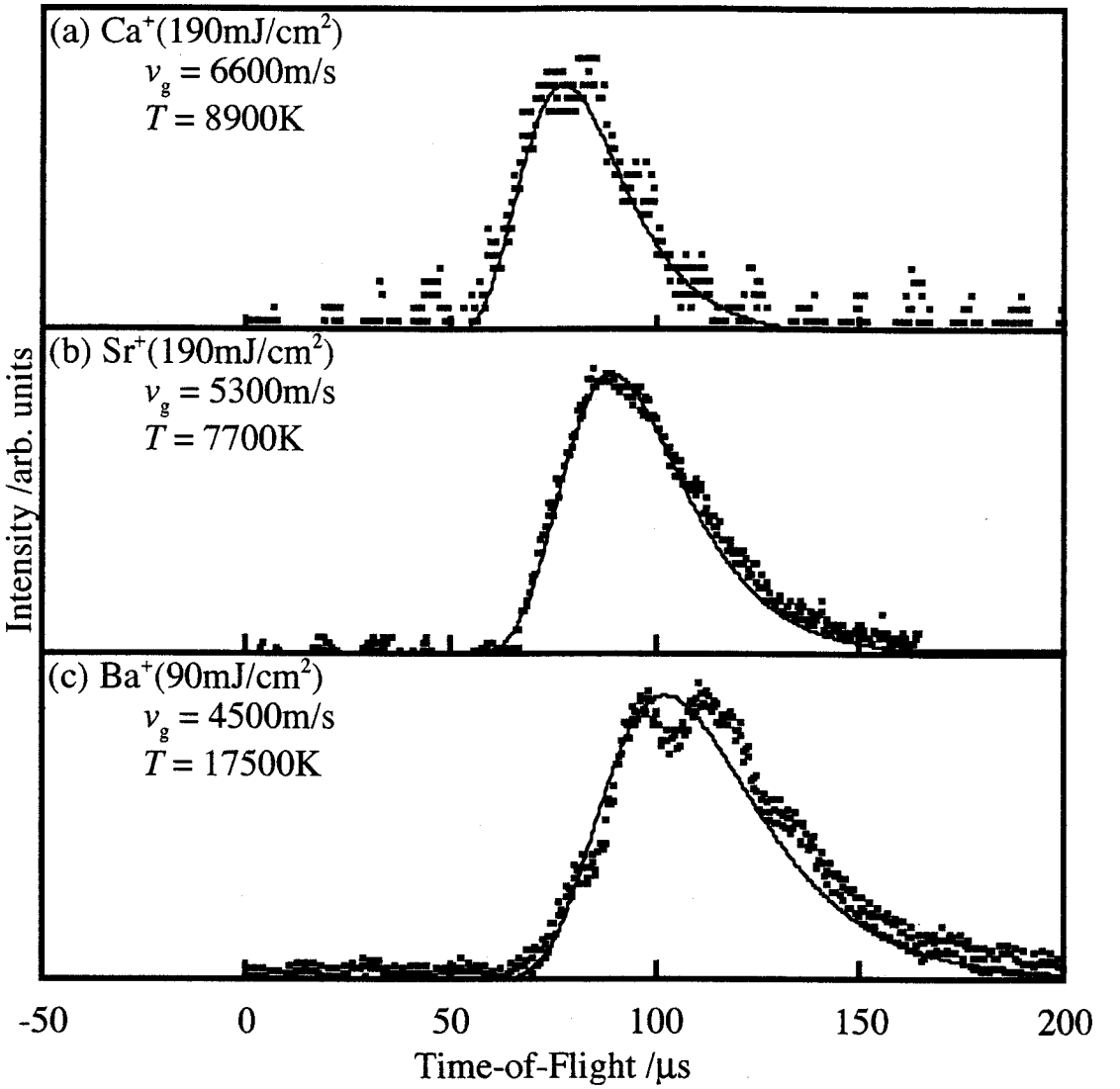

Fig. 1-2. The TOF spectra of Ca^+, Sr^+ and Ba^+ desorbed by the ArF excimer laser ablation. The laser fluence is (a) 190mJ/cm^2, (b) 190mJ/cm^2 and (c) 90mJ/cm^2. The solid lines are the theoretical curves obtained using the Maxwell-Boltzmann distribution corrected by center-of-mass velocity. Adjustable parameters are (a) v_g=6600m/s and T=8900K, (b) v_g=5300m/s and T=7700K and (c) v_g=4500m/s and T=17500K. It can be seen that the TOF spectra show good agreement with Maxwell-Boltzmann distribution.

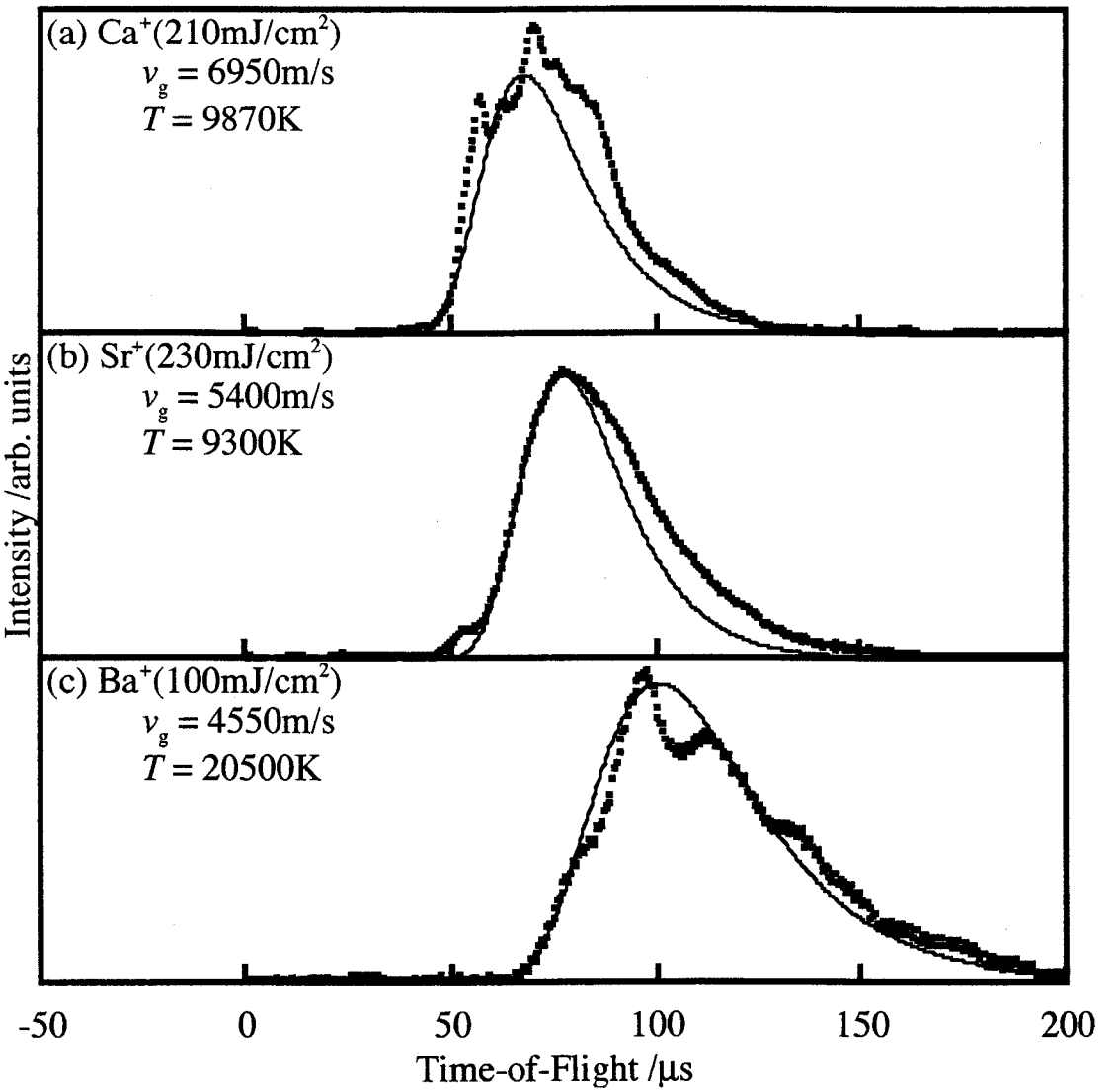

Fig. 1-3. The TOF spectra of Ca^+, Sr^+ and Ba^+ desorbed by the ArF excimer laser ablation. The laser fluence is (a) 210mJ/cm^2, (b) 230mJ/cm^2 and (c) 100mJ/cm^2. The solid lines are the theoretical curves obtained using the Maxwell-Boltzmann distribution corrected by center-of-mass velocity. Adjustable parameters are (a) v_g=6950m/s and T=9870K, (b) v_g=5400m/s and T=9300K and (c) v_g=4550m/s and T=20500K. In the higher fluence region than that shown in Fig. 1-2, the TOF spectra show deviation from Maxwell-Boltzmann distribution.

the ion desorption occurs with higher fluence than ~1J/cm^2 [2, 9]. The solid lines in Figs. 1-2 and 1-3 are theoretical curves obtained using the following Maxwell-Boltzmann distribution corrected by center-of-mass velocity [10].

$$n(t) = At^{-4} \exp\left[\frac{-m(z/t - v_g)^2}{2k_B T}\right]. \quad (1\text{-}1)$$

Here, $n(t)$ represents the ion flux observed at time t, A is a normalization constant, m is the mass of the ion, z is the distance from the target to the QMS, v_g is center-of-mass velocity, k_B is Boltzmann's constant and T is temperature. The v_g and T are used as adjustable parameters. The results show good agreement with Eq. (1-1) at the laser fluence of less than 190mJ/cm^2 (Fig. 1-2(a)), 190mJ/cm^2 (Fig. 1-2(b)) and 90mJ/cm^2 (Fig. 1-2(c)) for Ca^+, Sr^+ and Ba^+, respectively. These agreements indicate that the ion desorbed by the laser ablation reach thermal equilibrium with respect to Ca^+, Sr^+ and Ba^+. Such thermal equilibrium will result from many collisions between ion because the ion density is very high at the initial stage of the ion flight. When the fluence is higher than the above values, however, the TOF spectra begin to deviate from Maxwell-Boltzmann distribution (Fig. 1-3) and higher fluence results in larger deviation. It is considered that the deviation is caused by generation of delayed components. Namely, higher fluence than the critical fluence of each element may produce ion deep inside the solid that exhibit some time delay because of

collision with the ion desorbed from the surface region. The small contribution of this process may result in the slight deviation of the TOF spectra from Maxwell-Boltzmann distribution in Fig. 1-2. Thus it is considered that the thermal equilibrium state is realized in this experimental condition.

Figure 1-4 shows the relationship between effective temperature of the desorbed monovalent ion and the fluence for the ArF excimer laser. The graph is plotted in the region exhibiting agreement between measured TOF spectra and Eq. (1-1), i.e., Maxwell-Boltzmann distribution corrected by center-of-mass velocity. In Fig. 1-4, the temperature seems higher than that predicted by the thermal evaporation model [2, 9] (In the comparison of the temperature in Fig. 1-4 with the thermal model, it is assumed that the plume temperature is same with the ion temperature because the ion may not be desorbed in the thermal evaporation model). The results also support that the laser ablation of the metal is not simple thermal evaporation mechanism.

In Fig. 1-4, the temperature is proportional to the fluence (I) for each ion. This linear behavior will be explained by the model that the source of the thermal energy is absorbed after the desorption of chemical species. In this model, the photon which still incidents after the beginning of the desorption is absorbed by the free electron in the plume as "inverse Bremsstrahlung process" [11]. The accelerated electron can interact with

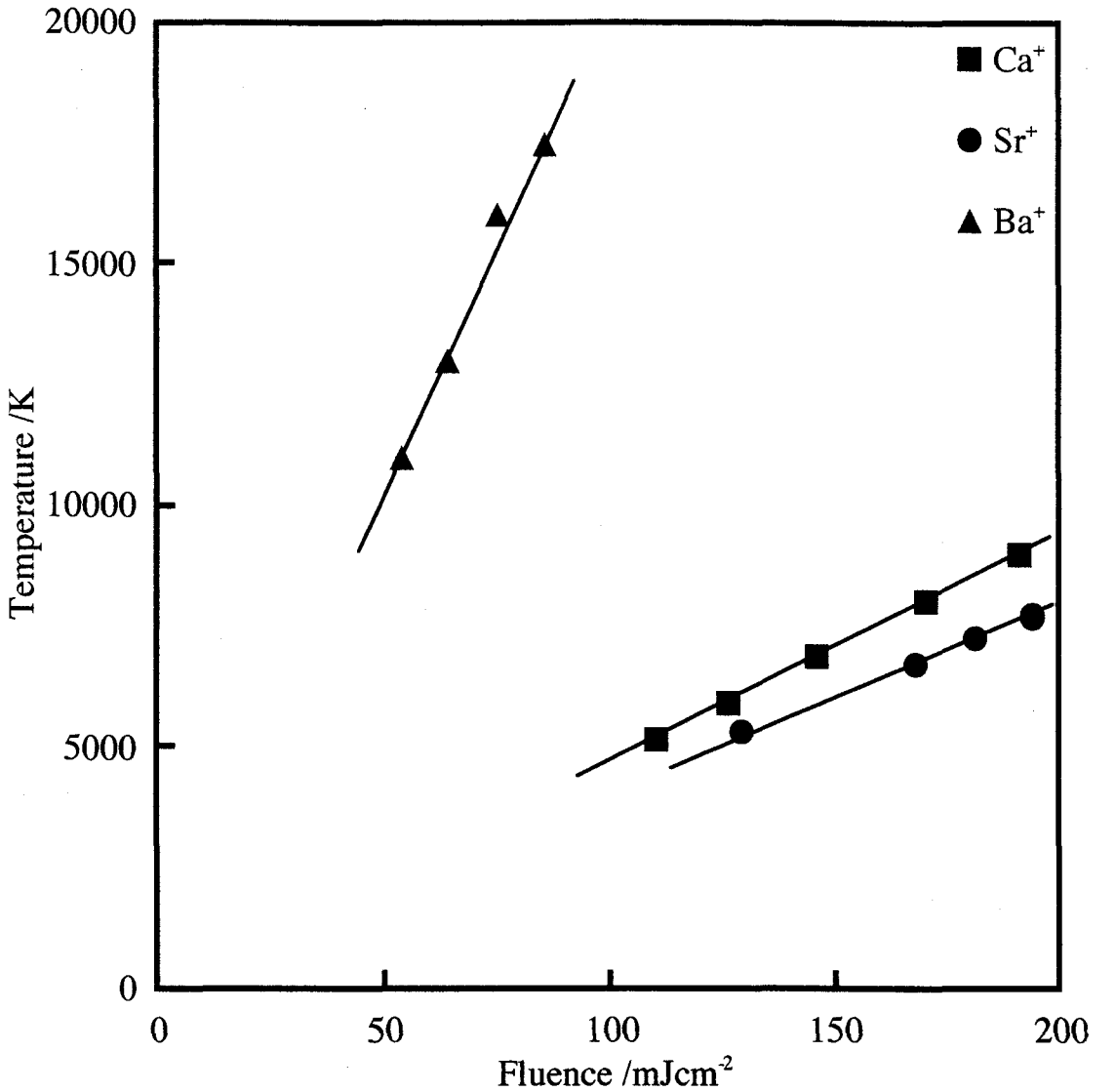

Fig. 1-4 The relationship between the temperature of the desorbed ion and the laser fluence for the ArF excimer laser ablation of Ca, Sr and Ba. The temperature is proportional to the fluence for all elements.

the ion by electrostatic force or neutral species by collision, namely the absorbed energy is redistributed among all desorbed chemical species [2, 9]. The model explains that this redistributed energy is the thermal energy, $\sim k_B T$. Since the assumption is natural that the absorbed energy is proportional to I [12], the redistributed energy is also proportional to I. In this manner, it can be shown that the temperature is proportional to the fluence.

Figures 1-5 and 1-6 show the amount of the desorbed ion vs. the fluence by using the ArF excimer laser and the KrF excimer laser, respectively. The amount is obtained by the integration of each TOF spectrum (Note that the collision apparently occur between the ion before that enters the QMS which may somewhat change the total number of ion. Although these processes may "offset" the absolute ion number, the ratio of the total ion number to the nascent ion number is expected to be approximately constant at different fluence). It is found that the amount of the desorbed ion is proportional to $I^{4.6\pm0.2}$, $I^{3.7\pm0.4}$ and $I^{2.9\pm0.3}$ for the results by the ArF excimer laser and $I^{6.4\pm1.0}$, $I^{5.3\pm1.2}$ and $I^{3.6\pm1.0}$ for the results by the KrF excimer laser with respect to Ca^+, Sr^+ and Ba^+, respectively. In the thermal evaporation model, the amount of the desorbed neutral atom will be roughly proportional to $(I-I_{th})$, where I_{th} is the threshold fluence that is the energy required for the surface heating up to melting or boiling point [12]. This simple consideration is based on that the surface temperature will be

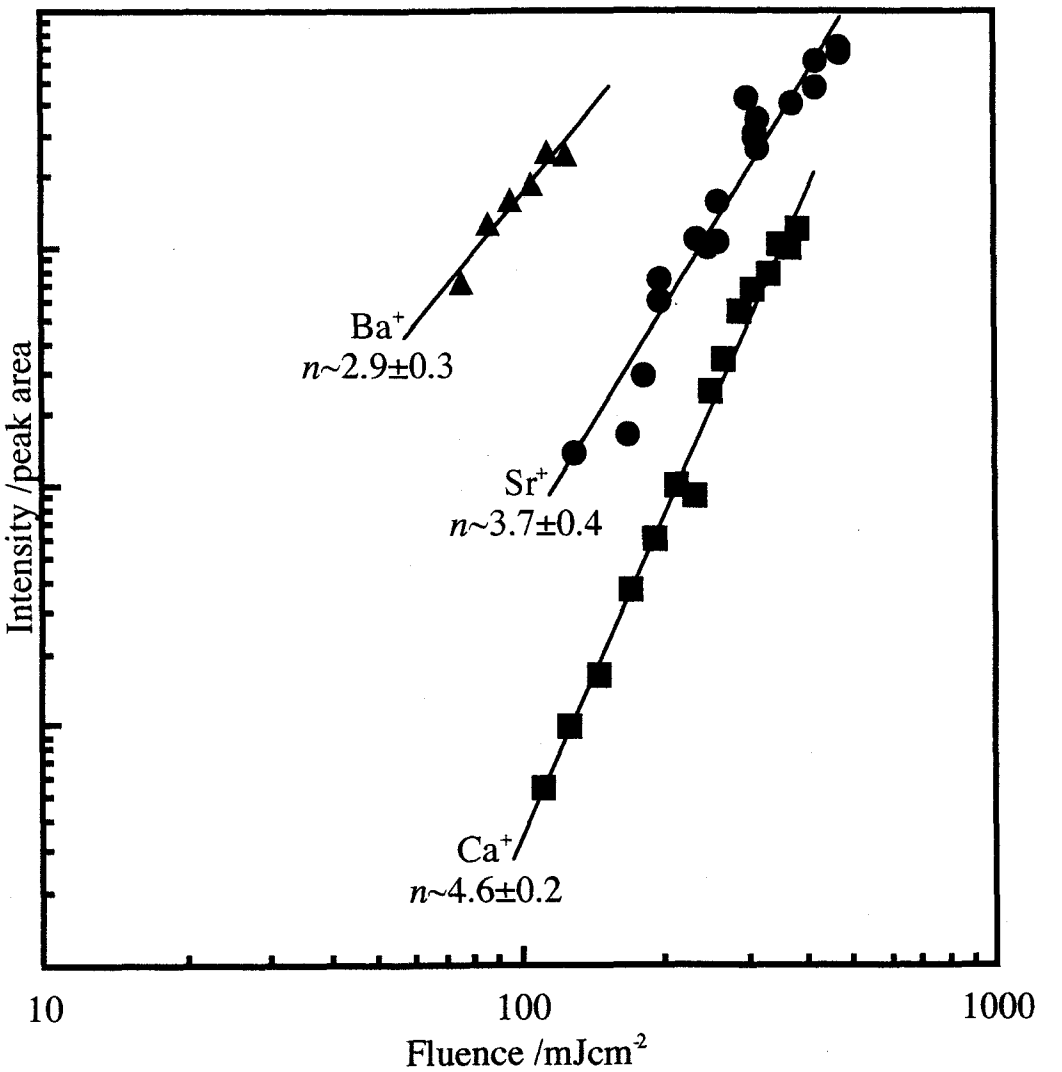

Fig. 1-5 The amount of the monovalent ion vs. the fluence using ArF excimer laser. Both axes are logarithmic scales. Each amount is obtained by integrating the TOF spectrum. It is found that the amount of the desorbed ion is proportional to $I^{4.6\pm0.2}$, $I^{3.7\pm0.4}$ and $I^{2.9\pm0.3}$ for Ca^+, Sr^+ and Ba^+, respectively. Here, "I" represents the fluence.

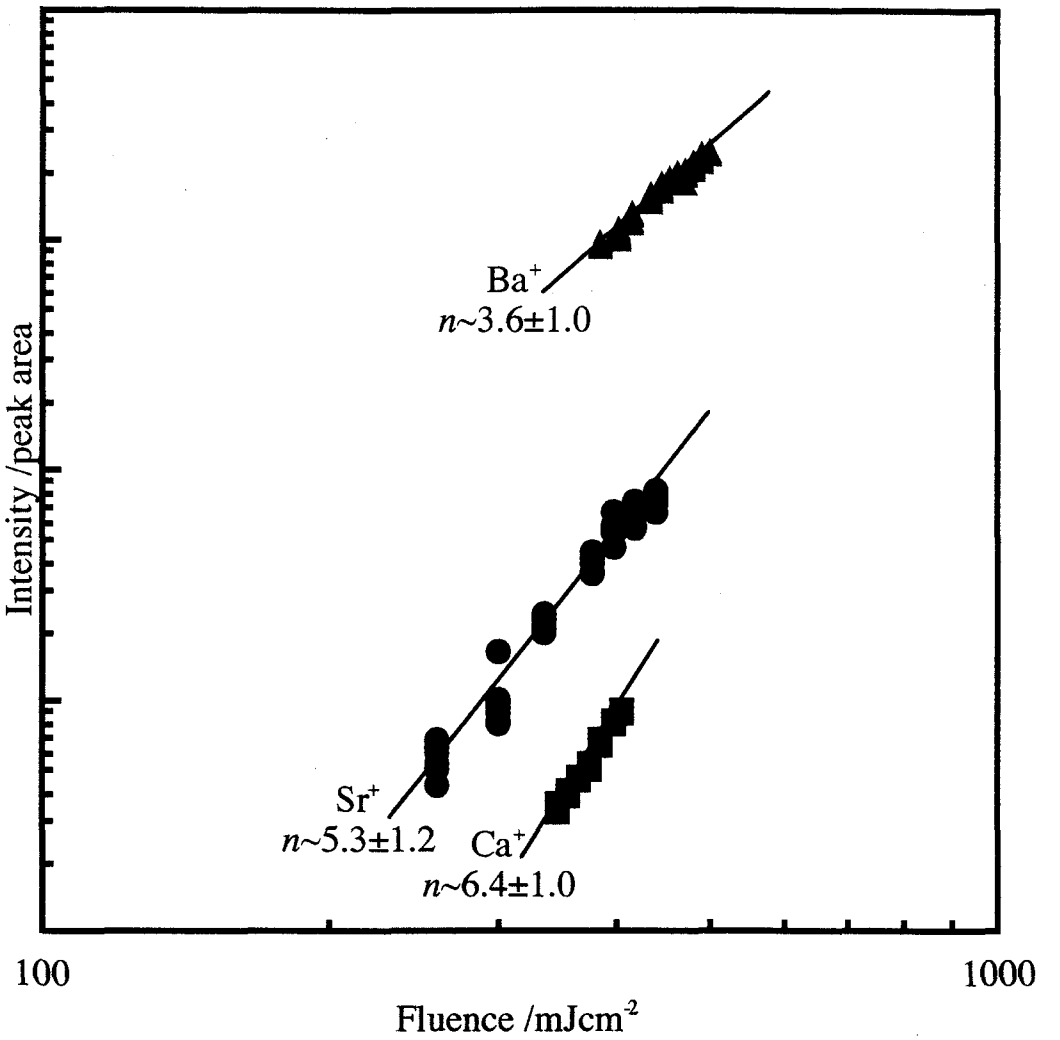

Fig. 1-6 The amount of the monovalent ion vs. the fluence using KrF excimer laser. Both axes are logarithmic scales. Each amount is obtained by integrating the TOF spectrum. It is found that the amount of the desorbed ion is proportional to $I^{6.4\pm1.0}$, $I^{5.3\pm1.2}$ and $I^{3.6\pm1.0}$ for Ca^+, Sr^+ and Ba^+, respectively.

proportional to the injected energy. Therefore, this nonlinear behavior can not be also explained by the thermal evaporation model. There is growing evidence that the fundamental phenomena for the laser ablation of the metal are not the thermal evaporation process. Since the power law can be interpreted as a multiphoton photochemical reaction, the desorption of monovalent ion may be caused by 5-, 4- and 3-photon processes (by using ArF excimer laser, 6.4eV/photon) and 6-, 5- and 4-photon processes (by using KrF excimer laser, 5.0eV/photon) for Ca^+, Sr^+ and Ba^+, respectively. On the basis of these results, a new model is constructed for the nascent process of the laser ablation of the metal on the standpoint that the direct electronic process is important.

First, the excitation of band electron is discussed. The band electron in typical metal, however, does not absorb the UV light so effectively [6]. In fact, the absorption is ~10% for typical metal at the UV region [7]. Furthermore, only 1-photon is sufficient for the excitation of the band electron, because the work function of the alkaline earth metal [13-15] is lower than 5.0eV and 6.4eV. This does not agree with the experimental results. Therefore, the excitation of core electron is discussed. In table 1-1, the binding energies of the highest core electron measured from the Fermi level [16] and the total photon energies from the experimental results, i.e., 5-, 4- and 3-photon energies of ArF excimer laser and 6-, 5- and 4-photon energies of KrF excimer laser, are shown. It is

Table 1-1 The binding energies of the highest core electron measured from Fermi level and the total photon energies from the experimental results, i.e., sum of 5-, 4- and 3-photon energies of ArF excimer laser and sum of 6-, 5- and 4-photon energies of KrF excimer laser.

orbital	binding energy /eV	photon energies for ArF /eV (6.4eV/photon)	photon energies for KrF/eV (5.0eV/photon)
Ca3p	27.7	32.0	30.0
$Sr4p_{3/2}$, $4p_{1/2}$	22.7, 23.8	25.6	25.0
$Ba5p_{3/2}$, $5p_{1/2}$	16.9, 19.1	19.2	20.0

found that those photon energies slightly exceed the binding energy of the highest core electron. The completely systematic results propose a model that the nascent process of ion desorption in the laser ablation of the alkaline earth metal is the ionization at the highest core level. The power law in Figs. 1-5 and 1-6 can not be explained in terms of the ionization after the neutral desorption by the thermal evaporation. The reason is that the photon number does not agree with the results in Figs. 1-5 and 1-6. In this process, an additional photon is needed for the desorption of the neutral atom, except for the photon needed for the core electron excitation in the atomic species which is the same photon number with the core electron excitation in the solid.

In summary of the section, the TOF spectra and the amount of the desorbed monovalent ion have been measured on the laser ablation for the alkaline earth metals by using time-resolved QMS. In the fluence region less than several hundred mJ/cm^2, the ion is desorbed while the simple thermal evaporation mechanism can not predict the ion desorption with such low fluence. The temperature obtained by the fitting of TOF spectra to Maxwell-Boltzmann distribution corrected by center-of-mass velocity is quite high than the prediction of the thermal evaporation model. The temperature is proportional to I because the energy absorbed by the free electron in the plume is proportional to I. The amount of the desorbed monovalent ion is proportional to I^n where $n > 1$. These results prove that

the ablation of the alkaline earth metal is not the simple thermal evaporation mechanism. The power law can be consistently interpreted as the highest core electron excitation by the multiphoton photochemical reaction.

1-3-2. The influence of the variation of the effective pulse duration by using double pulsed laser ablation technique.

In the previous section, a new model for the laser ablation of the metallic bond crystal has been proposed, i.e., the core electron excitation by the multiphoton process. At this point, however, the above model is considered to be somewhat tentative. Thus, further experimental evidence is needed. One of the key points is to clarify the role of thermal and nonthermal (electronic) phenomena in the ion desorption. Since thermal evaporation mechanism are normally expected to take place at typical time scale of 10ns or longer with the fluence region of less than several hundred mJ/cm^2 [2], time-resolved measurements may reveal the transient effects that is generally important for the improvement of the above model.

In this section, time-resolved studies of the ion desorption during the ArF excimer laser ablation of Ca metal. In order to perform the time-resolved studies, "double pulsed laser ablation technique" is used. By means of the technique, time profile of the laser beam is controlled with the delay time between two pulses, namely, effective pulse width and the photon number per unit time of the laser can be changed. The relationship

between the delay time and the amount of the desorbed Ca^+ is measured. On the basis of the results, the time scale of the process is clarified.

In Fig. 1-7, the squares indicate the measured dependence of the amount of the desorbed Ca^+ on the delay time. The amount of the desorbed ion was obtained by the integration of the TOF spectra for each delay condition. The TOF spectrum did not show any significant variation as a function of the delay condition. The ordinate is plotted as the ratio of the value of the signal to that of the single pulse ablation. Assuming simply that the 5th order process is responsible for the ion desorption, one would expect that the amount of the ion is proportional to the 5th order intensity autocorrelation function of the pulse, i.e.,

$$n(\Delta t) \propto \int_{-\infty}^{\infty} [I(t) + I(t-\Delta t)]^5 dt. \qquad (1\text{-}2)$$

Here, $I(t)$ is the time profile of the laser intensity and Δt is the delay between the two ablating pulses. The time profile of the laser pulse with Δt=0 is shown in Fig. 1-8 (It is found out that the scatter in the digitized experimental data causes the numerical instabilities in the evaluation of the integral; thus the analytical fit was performed using $I(t) \propto t^{2.2}\exp(-0.335t)$ indicated by the solid line). The curve corresponding to Eq. (1-2) is represented by the dashed line in Fig. 1-7. Comparing the dashed line with the measured data, it is clear that the decrease of the amount of the desorbed ion with respect to Δt is rapid than that expected from Eq. (1-2). This is quite surprising if it is considered that the ion desorption drops by

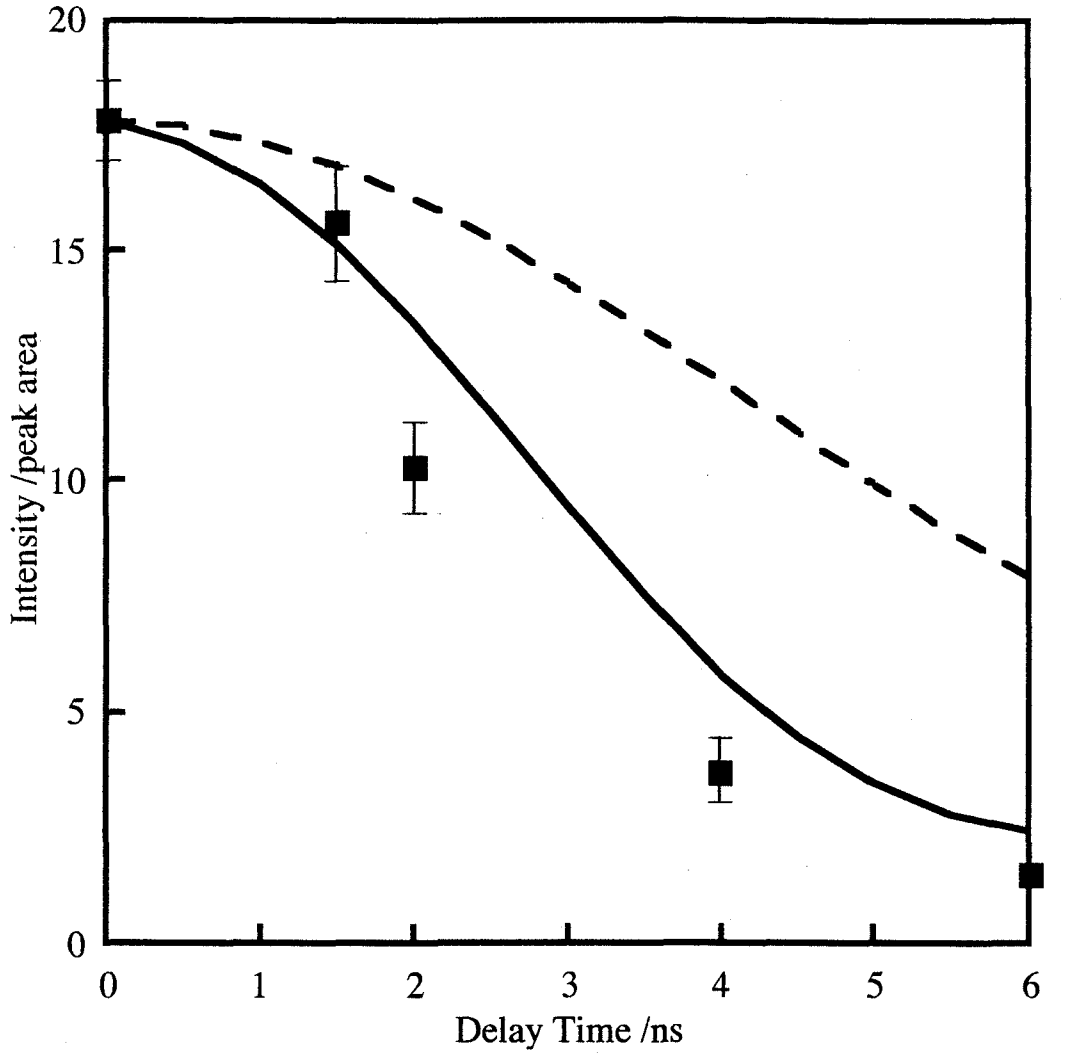

Fig. 1-7 The measured dependence of the amount of the desorbed Ca^+ on the delay time between the two ablating laser pulses (squares) for the ArF excimer laser ablation of Ca metal. The ordinate shows the ratio of the value of the signal to that of the single pulse ablation. The solid line is the best-fit line calculated using. Eqs. (1-3) and (1-4) (see text) while the dashed line is obtained assuming simply a 5-photon process i.e., Eq. (1-2).

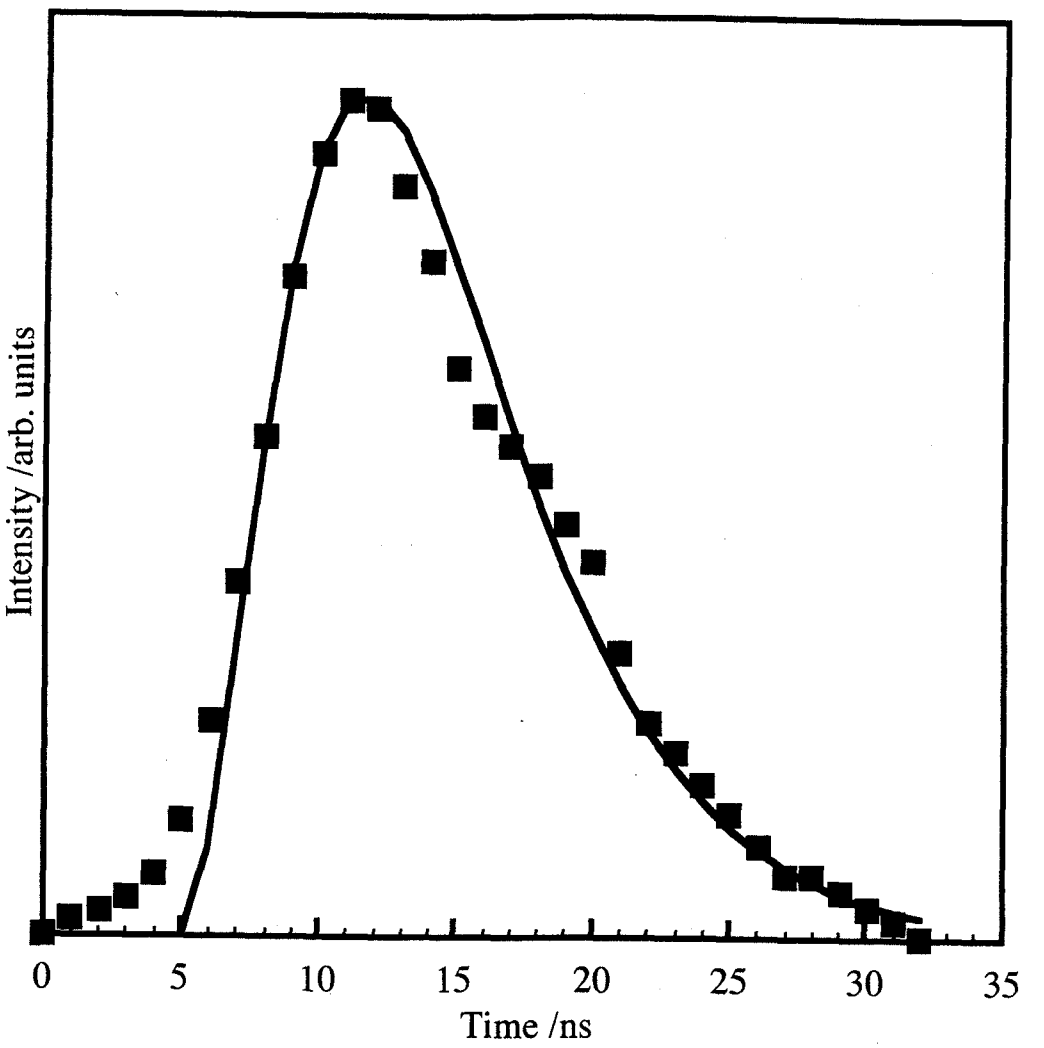

Fig. 1-8 The time profile of the experimental laser pulse (squares) and the analytical fit used for the calculation (solid line).

approximately one order of magnitude at 6ns delay where the first laser pulse barely reaches its maximum. The following explanation is suggested for this phenomenon. Considering the power law of the measured fluence-ion amount curves, it is believed that the ion is desorbed due to a 5-photon process. Therefore, it is assumed that the ion desorption occurs only as long as the laser pulse interacts with an unchanged metal surface. As the energy deposited into the metal reaches a certain threshold value (E_0), the surface changes via some abrupt process such as phase transition and plasma formation. At the same time, the changes terminate the ion desorption as well. The amount of the ion can be calculated as

$$n(\Delta t) \propto \int_{-\infty}^{\tau} [I(t) + I(t-\Delta t)]^5 dt. \qquad (1\text{-}3)$$

The τ can be obtained from evaluating

$$E_0 \propto \int_{-\infty}^{\tau} [I(t) + I(t-\Delta t)]\, dt. \qquad (1\text{-}4)$$

The solid line in Fig. 1-7 is drawn on the basis of Eqs. (1-3) and (1-4) using E_0 as a fitting parameter (Note that the only unknown parameter in Eqs. (1-3) and (1-4) is E_0). The best-fit line, i.e., the line shown in Fig. 1-7, is obtained with E_0=0.19E where E is the total energy of the laser after it passes through the MIF. Namely E corresponds to the total fluence of 400mJ/cm^2. The absolute value of E_0 can be calculated as ~100mJ/cm^2 in the consideration of the number of the significant figures. As one can see from the Fig. 1-7, the agreement between the calculations and the measured

data is satisfactory. It is proposed that the laser ablation of Ca metal using the ArF excimer laser terminates when the injected energy reaches ~100mJ/cm^2. This corresponds to the time scale of less than ~several ns while it varies as the function of the fluence.

This model deviates the relationship between the amount of the desorbed Ca^+ and the fluence from the simple 5-photon process in the condition of a single laser beam. In Fig. 1-9, the calculated result is shown for the relationship with Eqs. (1-3) and (1-4). It is found that the calculation shows better agreement with the experimental result, i.e., the higher fluence of the measured data deviates from the simple 5-photon process.

In the analysis, E_0 represents the fluence required to change the surface property and it should be correspond to the threshold fluence for the ablation of Ca metal. Since the threshold is found as ~100mJ/cm^2 in the experiment of the single beam ablation, which is equal to the value of E_0, the model discussed in this section seems to be consistent.

In summary of the section, double pulsed laser ablation has been performed in order to study the time scale for the phenomena on Ca metal with an ArF excimer laser. The amount of the desorbed Ca^+ is measured using a QMS as a function of the delay between the laser pulses. In the case of the irradiation of two equivalent laser pulses with 6ns delay, the amount of the desorbed Ca^+ is drastically decreased compared with no delay

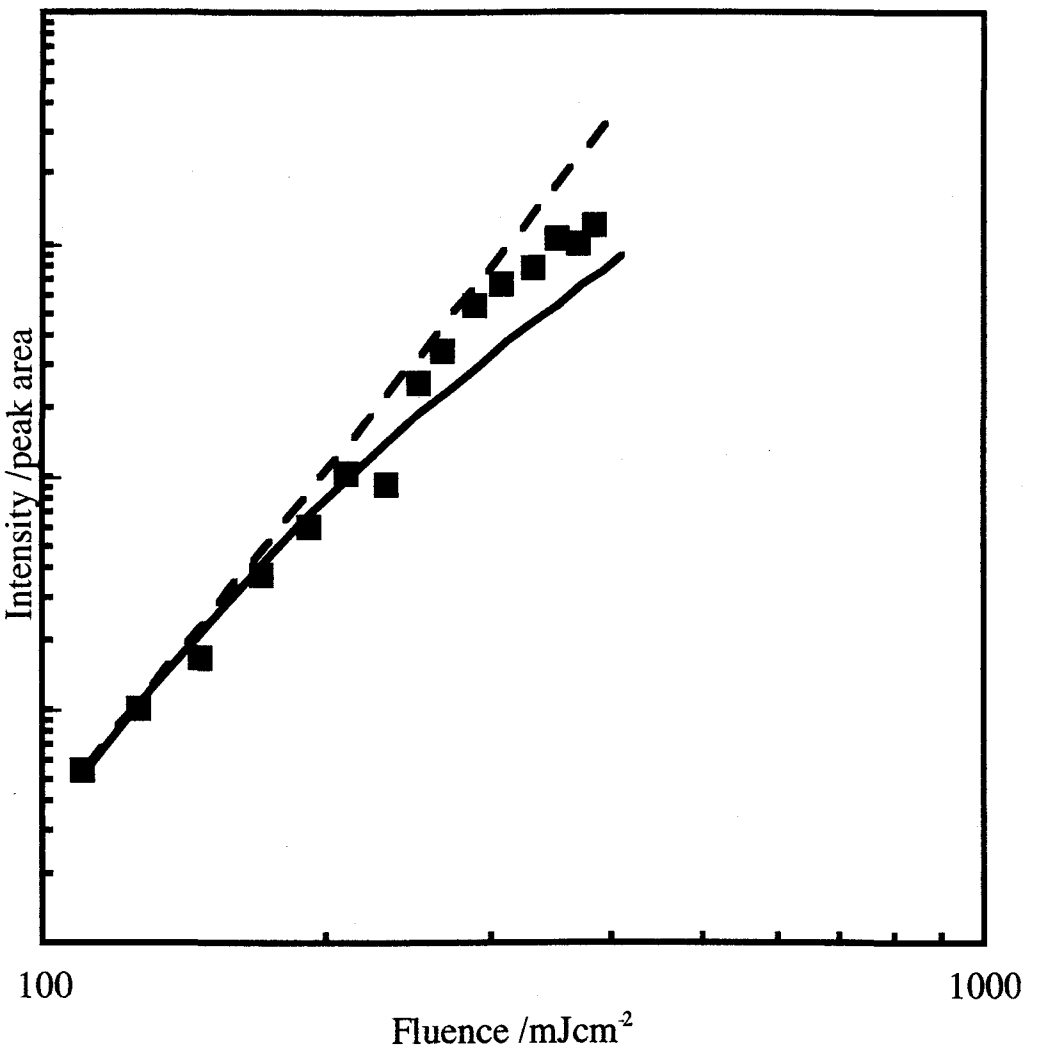

Fig. 1-9 The relationship between the amount of Ca^+ and the fluence for the simple ablation condition using ArF excimer laser for Ca metal (squares). The dashed line show the simple 5-photon process and solid line is the calculated relationship using Eqs. (1-3) and (1-4) for the single pulse ablation. The behavior of the experimental results at a higher fluence is closer to the solid line rather than dashed line.

condition. The total amount of the desorbed Ca^+ has been quantitatively analyzed as a function of the delay time on the basis of the result in previous section, i.e., 5-photon process. With respect to the analysis, it is proved that the experimental result is understood by introducing a model that the laser is cut off with the threshold fluence. It is found out that the Ca^+ are desorbed only the leading part of the laser pulse and the ion desorption practically terminates before the pulse is over, i.e., less than ~several ns. The termination of the ion desorption is considered to the abrupt changes of the surface of the Ca metal.

1-3-3. General remarks and the consideration on the mechanism of the laser ablation for the metallic bond crystal.

In the previous two sections, several experimental results have been reported. The results suggest that the laser ablation of the alkaline earth metal is not the simple thermal evaporation mechanism but the core electron excitation by the multiphoton process. In this model, however, there are two unanswered problems as follows.

1. The cross section may be too small to excite the core electron by the such high order multiphoton process.
2. The energy transfer process has not been proposed during the relaxation process.

In this section, those problems are considered. On the basis of the consideration and the results shown in the previous sections, the total model is constructed for the laser ablation of the metallic bond crystal.

First, the absolute value of cross section is discussed. There is no report for the cross section of the core electron excitation by the multiphoton process with respect to the alkaline earth metal. The cross section for the absorption of multiphoton by the core electron, however, will not be so sensitive to the element and physical phase, i.e., gas phase, liquid phase or solid state. Thus, the value is used in the report of the atomic Ar irradiated by 314.467nm photon. In the paper, the cross section is $\sim 1.4\times10^{-80}cm^6s^2$ for 3-photon process [17]. This value corresponds to the total photon density of $\sim10^{23}/cm^2$ in the time duration of laser pulse, i.e., ~10ns. The cross section is smaller than the above value in the higher order processes. Since the photon density in this study is $10^{17}/cm^2 \sim 10^{18}/cm^2$, the above requirement is not satisfied. It is found out that the simple multiphoton process via virtual level is not realistic. For this problem, the important point will be that the used targets of the alkaline earth metal are polycrystal. There are so many levels originating the defects of the crystal. Therefore, the multiphoton process in this phenomena may be the multi step excitation via the defect level.

The possible relaxation process after the producing the core hole is inferred while it is very difficult to propose a detailed model due to the

lack of the sufficient experimental data. It has been recognized that the lifetime of the charge excited state should be comparable to the typical frequency of the lattice vibration ($\sim 10^{-13}$s) on the desorption of the chemical species resulted from the interaction between the localized excitation and the lattice system [18]. Generally, the lifetime of the core hole is less than $\sim 10^{-15}$s [18, 19]. Thus it is not realistic that the core hole directly drives the desorption of the chemical species. It has been known by the experiment of x-ray photoelectron spectroscopy (XPS) that the core hole can excite the plasmon which screens the positive charge of the core hole [20, 21]. Since the diameter of the plasmon in this case will be the order of ~1Å estimated by the Thomas-Fermi screening length [22], this plasmon is quite localized excitation. The plasmon may have repulsive interaction with the ionic core after the inactivation of the core hole, the reason is that the plasmon lifetime ($\sim 10^{-14}$s [18]) is longer than that of the core hole. The above lifetime for the plasmon can be longer by the roughness of the target surface [18, 23, 24] (The used target was polished by a sandpaper, so the surface roughness will be ~μm). Thus, it is proposed that the lifetime of the excited state which can drive the ablation is close to the required value.

It should be considered that the core electron excitation on the XPS studies does not cause the ablation. The effect of the heat may be needed on the different phenomenon for the same excited state, i.e., core electron excitation. The surface of the target will be heated up on the high

density UV laser irradiation while that is not heated by the XPS. Since the absorbed UV photon by the band electron in the metal is ~10% [6] of the total incident photon, there is enough photon not to change the model of multiphoton process. The surface layer of the metal will be heated up to near 1000K [2] (This temperature is lower than the melting point of the alkaline earth metal) with the time scale of less than ~ns [2] by the typical thermal evaporation mechanism. This heating process will produce a lot of phonon excited to the higher mode. The higher mode phonon will assist the above repulsion between the plasmon and the ionic core after the inactivation of the core hole. In this way, the possible explanation is considered for the relaxation process of the core hole and the driving force of the desorption of the chemical species.

On the basis of the previous discussion and the consideration, the schematic model in the laser ablation of the alkaline earth metal is concluded in Fig. 1-10. The photon is absorbed by the electron in the highest core level via multiphoton process. In this step, the defect levels will play an important role in order to realize the core level ionization because the simple multiphoton process via virtual level is not effective (Fig. 1-10(a)). At the same time, the band electron is also excited via inverse Bremsstrahlung process. The energy absorbed by the band electron is transferred to the phonon with ~ps. The produced core hole in a site excites the plasmon which is localized near the ionic core with the diameter

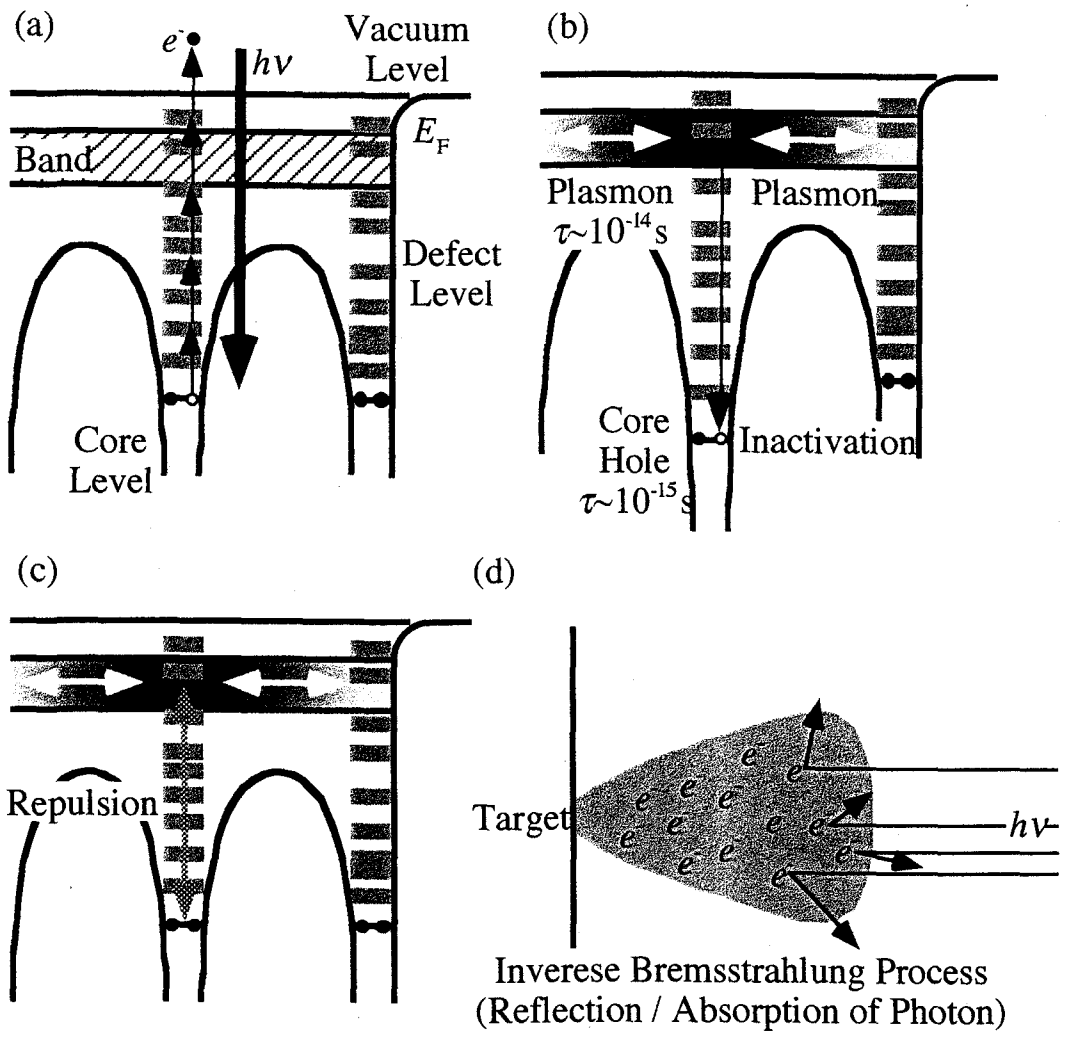

Fig. 1-10 The schematic illustration for the laser ablation mechanism of the alkaline earth metal. (a) The core electron is excited by the multiphoton process via defect level. (b) The core hole produces the plasmon near the ionic core in order to screen its positive charge. (c) After the inactivation of the core hole, the plasmon is left. The plasmon may have repulsive interaction with the ionic core which is inactivated. This repulsion is the driving force for the ion desorption in this model. (d) The laser beam is cut off by the inverse Blemsstrahlung process of the electron included in the plume.

of ~1Å (Fig 1-10(b)). The plasmon is left with the time scale of $\sim 10^{-14}$s or somehow longer while the core hole is inactivated with $\sim 10^{-15}$s. The plasmon can interact with the ionic core after the inactivation of the core hole by the Coulomb repulsive force. After ~ns from the starting of the laser irradiation, the phonon with the higher mode will be enough excited (Fig. 1-10(c)). If such phonon assists the Coulomb repulsion between the ionic core and the plasmon, the desorption of the chemical species can be possible.

The chemical species is quite dense just after the desorption from the target, so the collision is very frequent. By means of the collision, the chemical species will reach the thermal equilibrium. In this step, the energy of the laser pulse is absorbed by the plume (free electron in the plume) rather than the target surface (Fig. 1-10(d)). Once this process occurs, the desorption of the chemical species by the laser ablation is over. Since the energy absorbed by the plume is proportional to I from the simple consideration, the energy distributed to the plume as heat is also proportional to I. In this way, the model for the alkaline earth metal is proposed as "core electron excitation mechanism via multiphoton photochemical reaction".

1-4. Conclusion.

In conclusion, the TOF spectra and the amount of the desorbed monovalent ion by the laser ablation of the alkaline earth metal in order to understand the nascent process of the phenomena for the metallic bond crystal using ArF excimer laser and KrF excimer laser. The ion is desorbed with the fluence of less than several hundred mJ/cm^2 while the simple thermal evaporation mechanism predicts the ion desorption for the fluence of higher than $\sim 1J/cm^2$. The relationship between the amount of the desorbed ion and the fluence shows highly nonlinear behavior. This result also does not support the simple thermal evaporation mechanism. On the basis of the results, a new model has been proposed that the laser ablation of the alkaline earth metal is caused by the highest core electron excitation via the multiphoton photochemical reaction. The double pulsed laser ablation has been performed in order to study the time scale for the phenomena on Ca metal with an ArF excimer laser. The amount of the desorbed Ca^+ is measured using a QMS as a function of the delay between the laser pulses. The total amount of the desorbed Ca^+ has been quantitatively analyzed as a function of the delay time on the basis of the multiphoton process. With respect to the analysis, it is proved that the experimental result is understood by introducing a model that the laser is cut off with certain threshold fluence. It is found out that the Ca^+ are desorbed only the leading part of the laser pulse and the ion desorption

practically terminates before the pulse is over, i.e., less than ~several ns. The termination of the ion desorption is considered to the abrupt changes of the surface of the Ca metal. On the basis of the results, the total model has been proposed for the laser ablation of the alkaline earth metal.

References

[1] N. Bloembergen: *AIP Conf. Proc. 288*, eds. J. C. Millor and D. B. Geohegan (American Institute of Physics, New York, 1994) p. 3.

[2] A. Vertes, R. W. Dreyfus and D. E. Platt: IBM J. Res. Develop. **38** (1994) 3.

[3] R. Kelly, J. J. Cuomo, P. A. Leary, J. E. Rothenberg, B. E. Braren and C. F. Aliotta: Nucl. Instrum. & Methods B **9** (1985) 329.

[4] J. C. S. Cools: *Pulsed Laser Deposition of Thin Films*, eds. D. B. Chrisey and G. K. Hubler (John Wiley & Sons, Inc., New York, 1994) p. 455.

[5] I. Lee, J. E. Parks II, T. A. Callcott and E. T. Arakawa: Phys. Rev. B **39** (1990) L73.

[6] L. K. Ang, Y. Y. Lau, R. M. Gilgenbach and H. L. Spindler: Appl. Phys. Lett. **70** (1997) 696.

[7] C. Kittel: *Introduction to Solid State Physics* (John Wiley & Sons, Inc., New York, 1986) 6th ed., chap. 10, p. 259.

[8] H. Helvajian and R. Welle: J. Chem. Phys. **91** (1989) 2616.

[9] R. W. Dreyfus: J. Appl. Phys. **69** (1991) 1721.

[10] J. P. Zheng, Z. Q. Huang, D. T. Shaw and H. S. Kwock: Appl. Phys. Lett. **54** (1989) 280.

[11] R. K. Singh and J. Narayan: Phys. Rev. B **41** (1990) 8843.

[12] Private communication with Dr. J. J. Dubowski.

[13] K. A. Kress and G. J. Lapeyre: Solid State Commun. **9**(1971) 827 (Ca: Φ=2.9eV).

[14] L. Gaurt, P. Renucci and R. Rivoira: Phys. Rev. B **15** (1977) 3078 (Sr: Φ=2.64eV).

[15] L. Gaurt, P. Renucci and R. Rivoira: J. Appl. Phys. **49** (1978) 4105 (Ba: Φ=2.3eV).

[16] The energy difference between the core electron level and Fermi level was measured by x-ray photoelectron spectroscopy. The data are shown in: I. Ikemoto et al.: *Kagaku Binran Kiso-hen*, ed. The Chemical Society of Japan (Maruzen, Tokyo, 1984) 3rd ed., vol. 2, chap. 14, p. 582 [in Japanese].

[17] N. M. Khambatta, L. J. Radziemski and S. N. Dixit: Phys. Rev. A **39** (1989) 3842.

[18] F. Balzer, R. Gerlach, J. R. Manson and H.-G. Rubahn: J. Chem. Phys. **106** (1997) 7995.

[19] M. L. Knotek and P. J. Feibelman: Phys. Rev. Lett. **40** (1978) 964.

[20] L. I. Johansson and I. Lindau: Solid State Commun. **29** (1979) 379.

[21] L. Armand, J. L. Bouillot and L. Gaudart: Surf. Sci. **86** (1979) 75.

[22] C. Kittel: *Introduction to Solid State Physics* (John Wiley & Sons, Inc., New York, 1986) 6th ed., chap. 10, p. 266.

[23] J. M. Elson and R. H. Ritchie: Phys. Rev. B **4** (1971) 4129.

[24] M. J. Shea and R. N. Compton: Phys. Rev. B **47** (1993) 9967.

Chapter 2

Surface Morphology of Oxide Thin Film Crystals Grown by Laser Molecular Beam Epitaxy.

Abstract

Growth for thin film crystal of perovskite-type oxides, $CaTiO_3$ and $La_{0.7}Sr_{0.3}MnO_3$, on atomically smooth $SrTiO_3(100)$ substrates has been studied by *in-situ* reflection high energy electron diffraction (RHEED) and *ex-situ* atomic force microscope (AFM) in order to understand the key points to keep the surface flatness. It is found out that the termination of substrate surface by AO layer of perovskite structure (ABO_3), i.e., CaO, SrO and BaO, is quite effective to prepare the atomically flat thin films. Among these top layers, the SrO termination gives the best result. $CaTiO_3$ film on $SrTiO_3(100)$ can keep the atomically flat surface in spite of large lattice mismatch (~2.3%), while $La_{0.7}Sr_{0.3}MnO_3$ needs more strict lattice matching to keep the flat surface. Structure and orientation of SrO are analyzed by only *in-situ* RHEED observation as the first step of real-time growth control. Furthermore, the migration process of Sr supplied by laser ablation is studied by time-resolved measurement of RHEED intensity. The migration process of chemical species supplied by laser ablation method is discussed during the thin film growth.

2-1. Introduction.

Recently, transition-metal oxides are attracting researchers' interests because of their characteristic property such as high T_c superconductivity, di- and ferroelectricity, colossal magnetoresistivity, and so on. Device applications of such oxides have been investigated by many workers using heterostructure or superlattice [1]. One of the most important point for the device application is realization of the atomically smooth interfaces. The control of the interface must be also important in the field of the fundamental material science, because frequent electron scattering resulting from randomness of interlayer screens the intrinsic electronic properties of multilayer systems. In the present stage, however, the ultimate growth technology, i.e., growth control with the accuracy of atomic scale, is not enough achieved for oxides, nevertheless technique of the heteroepitaxial growth of oxides has been rapidly developed [2, 3] since the discovery of high T_c superconductors [4].

For the growth control with the atomic accuracy, the surface flatness of substrate is quite important. If the surface of the substrate is not atomically flat, the film grown on such substrate usually does not have the flat surface. With respect to $SrTiO_3$(100) of perovskite type structure (see Fig. 1 in General Introduction) which is a popular substrate for various oxide films, effective treatments for the surface improvement have been discovered recently. One is oxygen-annealing [5] and the other is wet

etching by buffered-HF solution [6]. By such treatments, the atomically flat terraces separated by steep step with the height of an unit cell appear. Therefore, the next step is realization of the growth of various single- and multilayered thin films on the atomically smooth $SrTiO_3(100)$ with keeping the surface flatness.

In this chapter, the surface flatness is studied of $CaTiO_3$ film and $La_{0.7}Sr_{0.3}MnO_3$ film, here both crystals have the perovskite type structure, grown on atomically flat $SrTiO_3(100)$ substrate by using *in-situ* reflection high energy electron diffraction (RHEED, see Appendix B) and *ex-situ* atomic force microscope (AFM). $CaTiO_3$ is a good insulator for a tunneling junction. $La_{1-x}Sr_xMnO_3$ has recently very noted because of its colossal magnetoresistance [7]. In the heteroepitaxy of these oxides, two factors have been noted concerning the surface flatness. The first factor is surface stability during the growth. To study this point, four types of surface that are terminated with TiO_2, CaO, SrO and BaO are used as substrates . By the comparison of the films on above four types of surface, the termination effect of the substrate surface is clarified. The second factor is lattice mismatch. By using the single- and multilayered system of $CaTiO_3$ (a=3.82Å with pseudo cubic) and $La_{0.7}Sr_{0.3}MnO_3$ (a=3.88Å with pseudo cubic) on $SrTiO_3$ (a=3.905Å), the study is possible for the growth manner of several systems with lattice mismatch from ~0.38% ($La_{0.7}Sr_{0.3}MnO_3/SrTiO_3$) to ~2.3% ($CaTiO_3/SrTiO_3$). On the basis of above

experimental results, the important factors for keeping the atomically smooth surface during the oxide film growth are discussed. In addition, structure and orientation of SrO on TiO_2 terminated $SrTiO_3(100)$ are analyzed by only *in-situ* RHEED pattern observation as the first step of RHEED utilization for real-time growth control. Furthermore, the migration process of Sr supplied by the laser ablation method is discussed from the standpoint of the reaction rate by means of the time-resolved measurement of RHEED intensity [8]. The growth process of thin film with atomic level by laser ablation method is discussed with this experiment.

2-2. Experimental.

$CaTiO_3$ and $La_{0.7}Sr_{0.3}MnO_3$ thin film crystals were prepared by laser molecular beam epitaxy (laser MBE) method in a vacuum chamber with the base pressure of about 10^{-6}Pa (Fig. 2-1). An ArF excimer laser (Lumonics: EX-700, λ=193nm) was used as a light source with the fluence of about 1J/cm^2. The substrates were $SrTiO_3(100)$ single crystal (Shinkosha: one side polished) which was annealed in oxygen atmosphere with the pressure of 1atm at 1000°C for 10 hours. During the deposition, the substrate was heated up to the temperature (T_{sub}) of 350~700°C. The temperature was monitored by an optical pyrometer (MINOLTA: IR-308). In order to oxidize the thin films, NO_2 gas was introduced to the growth chamber with the pressure (P_{NO2}) of 5×10^{-4}~5×10^{-3}Pa. RHEED (Tosei

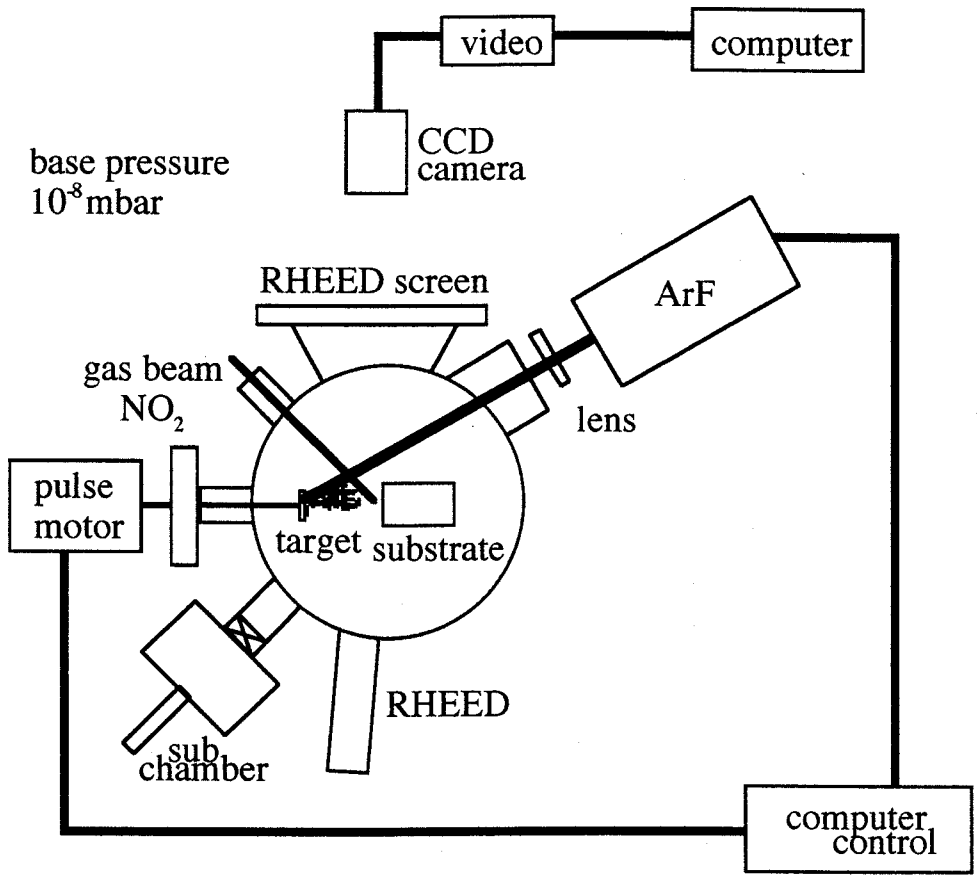

Fig. 2-1 The schematic diagram of the laser MBE apparatus.

Engineering: RHG-1000) with the acceleration energy of 15keV was used for the *in-situ* monitoring of the surface structure and morphology of the growing films. The RHEED pattern on fluorescent screen was acquired by a CCD camera (Hamamatsu photonics: C3077) and then digitized and analyzed by a personal computer (NEC: PC-9801ns) with an image digitizer (Photoron: FRM1-512). The sampling interval of the RHEED intensity monitoring was 1s for the usual measurement, while it was 50ms for the time-resolved measurement. Real-space measurement of the surface morphology of the grown film was performed by an *ex-situ* AFM (Digital Instruments: Nanoscope E) in air.

2-3. Results and Discussion.

2-3-1. $SrTiO_3$(100) substrate.

Typical two types of AFM images of the oxygen-annealed $SrTiO_3$(100) are shown in Figs. 2-2(a) (type #1) and 2-2(b) (type #2). These two images in Figs. 2-2(a) and 2-2(b) have large difference. The surface of #1 consists of atomically flat terraces separated by long steps with the height of ~4Å corresponding to the height of a unit cell. The terrace width is ~5000Å. On the other hand, the steps on #2 surface are short and random with respect to the direction, while the terrace is also atomically flat. The height of steps distributes from a unit cell to ten and several unit cells. Since the treatment procedure is completely same, the difference of the step

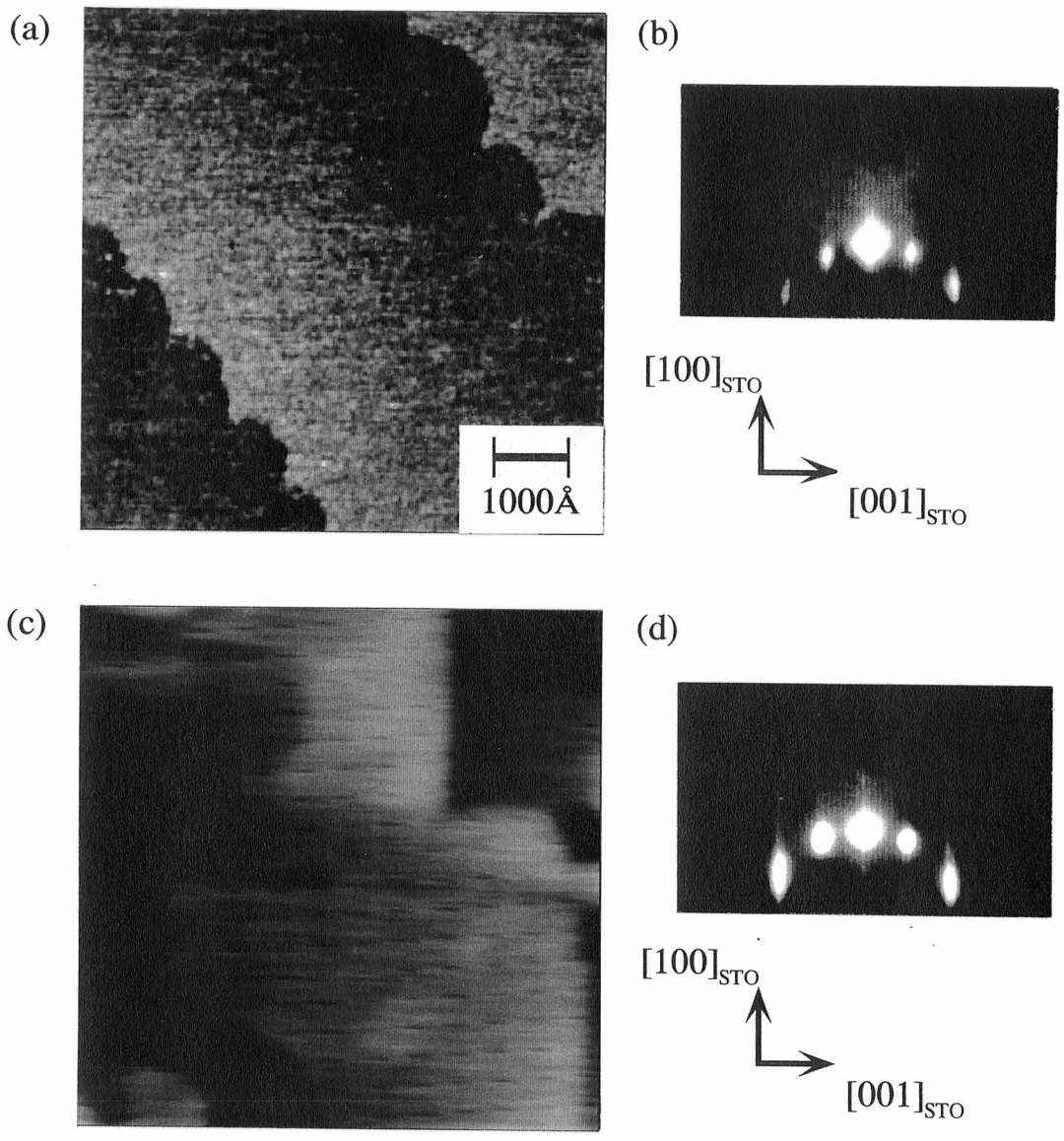

Fig. 2-2 The AFM images and RHEED patterns of the oxygen-annealed $SrTiO_3$(100) for type #1 [(a) and (c)] and type #2 [(b) and (d)]. The electron beam of RHEED incidents from [010] direction. It is found out that the surface observed by AFM is different between type #1 and type #2, while the anneal condition is same. The flatness of the terrace region is, however, similar. In both RHEED patterns, Laue spots of superstructure with the periodicity of 2 times can be seen.

length and the step height between #1 and #2 will depend on the surface condition of as-delivered substrates. Generally, outermost surface of the as-delivered crystal becomes amorphous due to the damage by mechanical polishing. The annealing will result in the migration and evaporation of the atoms in such amorphous surface layer. With the migration, the atoms will crystallize at step site of undamaged crystal under the amorphous. Because the step formed at the undamaged surface of each substrate is different, such difference causes the different step shape as shown in Figs. 2-2(a) and 2-2(b). Namely, the step shapes depend on polishing condition of the substrate. On the other hand, the terraces of the both substrates are atomically flat. It shows that the atomically flat (100) surface is very stable under the annealing condition. So the terrace flatness of the annealed $SrTiO_3$(100) does not depend on the form of undamaged layer.

RHEED patterns of #1 and #2 are shown in Figs. 2-2(c) and 2-2(d), respectively. The patterns of both types have very clear 0th Laue spots and short streaks (see Appendix B). It shows good crystallinity and flatness. This result agrees well with the AFM images that show the presence of atomically flat terraces.

2-3-2. Heteroepitaxial growth of $CaTiO_3$ on atomically flat $SrTiO_3(100)$ surface.

Figure 2-3 shows the AFM image of $CaTiO_3$ film with thickness of 10 unit cell grown on the oxygen-annealed $SrTiO_3(100)$ of type #2. The T_{sub} and P_{NO2} were 700°C and 1×10^{-3}Pa, respectively. The surface of $CaTiO_3$ is very rough and does not keep the flatness of the substrate at all. During the film growth, the intensity of RHEED specular beam did not oscillate (see Appendix B). These results show that the direct deposition of $CaTiO_3$ is not suitable for the preparation of atomically flat film on the oxygen-annealed $SrTiO_3(100)$. Concerning this problem, it should be recognized that the stability of the outermost surface during the film growth is important. It has been reported that the surface layer changes from TiO_x (or CuO_x) to SrO_x in the epitaxial growth of $SrTiO_3$ (or $SrCuO_2$) on $SrTiO_3(100)$ substrates [9]. This fact indicates that the AO surface is more stable than that of the BO_2 surface in the perovskite structure (ABO_3). Since the outermost surface of oxygen-annealed $SrTiO_3(100)$ is terminated with TiO_2 layer [9], an atomic AO layer have been deposited on the atomically flat $SrTiO_3(100)$ as the buffer layer in order to stabilize the surface during the growth. The reason for the TiO_2 termination of $SrTiO_3(100)$ has been explained as follows [10]. Namely, the SrO layer on the surface was dissolved by the surface rinse using water before the delivery while the most stable is SrO surface rather than TiO_2 surface.

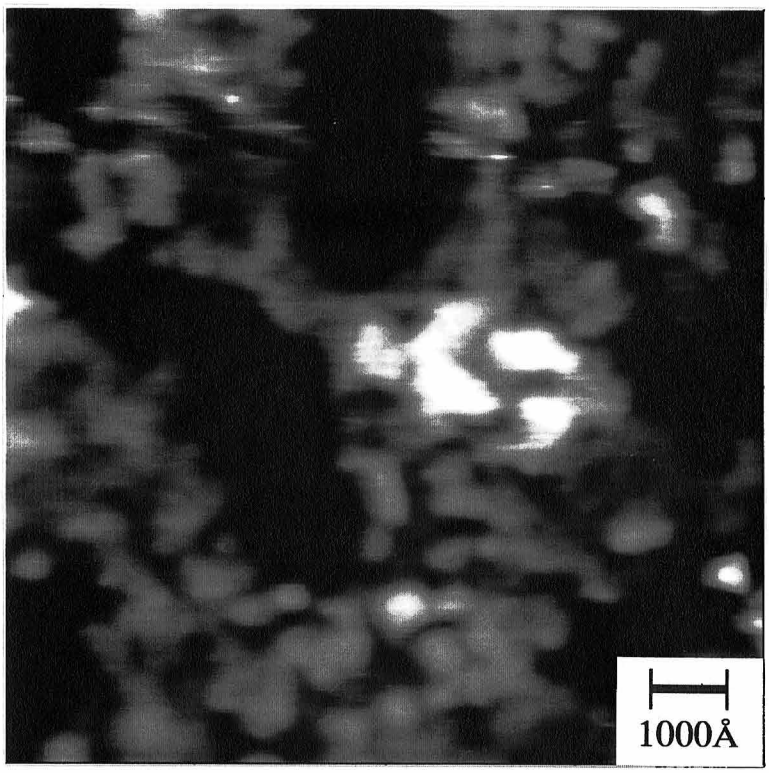

Fig. 2-3 The AFM images of $CaTiO_3$ thin films prepared on the oxygen-annealed $SrTiO_3(100)$ of type #2. The surface flatness is not maintained for the film surface.

CaO, SrO and BaO are chosen as the buffer layer because they are able to be AO layer of perovskite structure. Further, there are stable oxide compounds with the rock salt structure that have same atomic alignments with perovskite AO layer in $ABO_3\{100\}$ plane. The variations of RHEED intensity are shown in Figs. 2-4 and 2-5 during the $CaTiO_3$ deposition. The experimental condition is T_{sub}=700°C and P_{NO2}=1×10^{-3}Pa for Fig. 2-4, and T_{sub}=630°C and P_{NO2}=5×10^{-4}Pa for Fig. 2-5, respectively. The film thickness is 10 unit cell. For the SrO and BaO buffer, clear RHEED oscillation continues till the end of film growth at lower T_{sub} of 630°C, while the oscillation is damped at higher T_{sub} of 700°C. Such damping is also seen during the film deposition on CaO buffer even if the T_{sub} is 630°C. Namely, the CaO buffer is not so good compared with SrO and BaO buffer from the viewpoint of RHEED oscillation, because the RHEED oscillation is the characteristic behavior of two-dimensional layer-by-layer growth. The factor of such difference between the film growth on CaO buffer and that on others may be considered that the CaO buffer has the tendency to be rough surface. The roughening of CaO buffer will be caused by the large lattice mismatch between bulk CaO and $SrTiO_3$ (~13%). The three-dimensional islands of the CaO can become three-dimensional core of the $CaTiO_3$ growth. With respect to the other buffer layers, the lattice mismatch for $SrTiO_3$ is much smaller than that for CaO buffer, i.e., ~6.5% for SrO and ~0.38% for BaO. This result shows

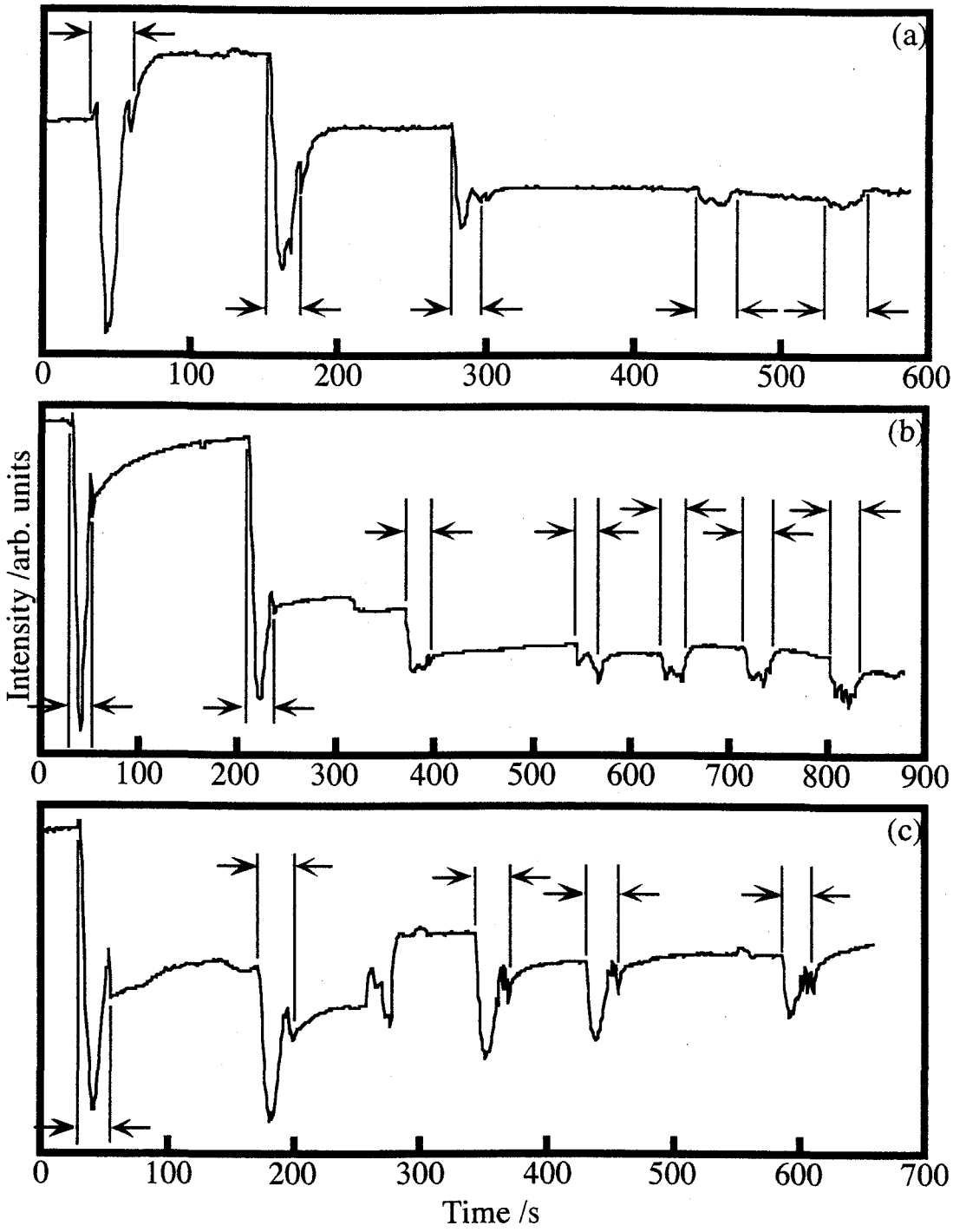

Fig. 2-4 The variation of RHEED intensity during the deposition of $CaTiO_3$ on oxygen-annealed $SrTiO_3(100)$ with an atomic layer of CaO (a), SrO (b) and BaO (c), respectively, at T_{sub}=700°C and P_{NO2}=1×10^{-3}Pa. The time regions sandwiched by two arrows show deposition and the others are interval time. Several times oscillation can be seen.

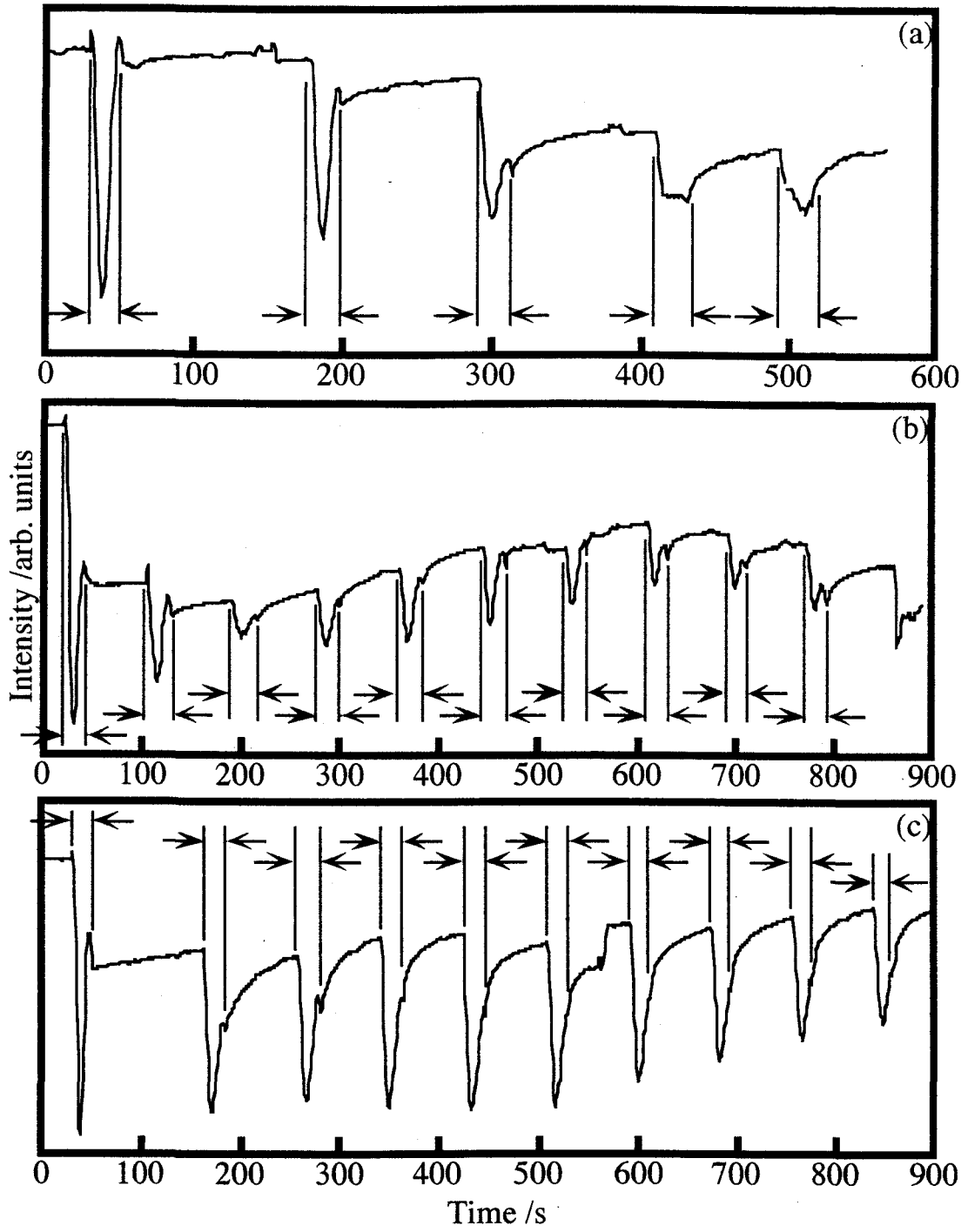

Fig. 2-5 The variation of RHEED intensity during the deposition of $CaTiO_3$ on oxygen-annealed $SrTiO_3$(100) with an atomic layer of CaO (a), SrO (b) and BaO (c), respectively, at T_{sub}=630°C and P_{NO2}=5×10^{-4}Pa. The time regions sandwiched by two arrows show deposition and the others are interval time. For (b) and (c), the continuous oscillations can be seen.

that the lattice matching with the substrate is important factor for the suitable buffer. The reason why the low T_{sub} condition brings good result can be considered as follows. In the higher T_{sub} condition, the three-dimensional growth by the condensation of materials will be mixed with two-dimensional growth mode because the surface migration is activated by the higher temperature.

AFM images of above samples are shown in Figs. 2-6 and 2-7. In all images, flat terrace and steep step can be seen. On the BaO buffer, however, there are several particles with the diameter of about several hundreds Å. The BaO buffer is not so good compared with other two buffers from the AFM results. Such particles may be generated by means of the reaction between Ba diffused into the $CaTiO_3$ film and H_2O etc. in air. The reason of the diffusion will be much lower melting point of BaO (1920°C at 1atm, following data is same condition of the pressure) than that of CaO (2570°C) and SrO (2430°C). Furthermore, the BaO sublimates at ~1380°C of quite low temperature. Such large differences of thermodynamical property will cause the above AFM results. On the basis of the RHEED and AFM results, it is found that the SrO termination of $SrTiO_3$(100) is the most effective for the film growth with atomically flat surface.

In conclusion, it has been succeeded to prepare the atomically flat $CaTiO_3$ ultrathin film by the A-site termination of oxygen-annealed

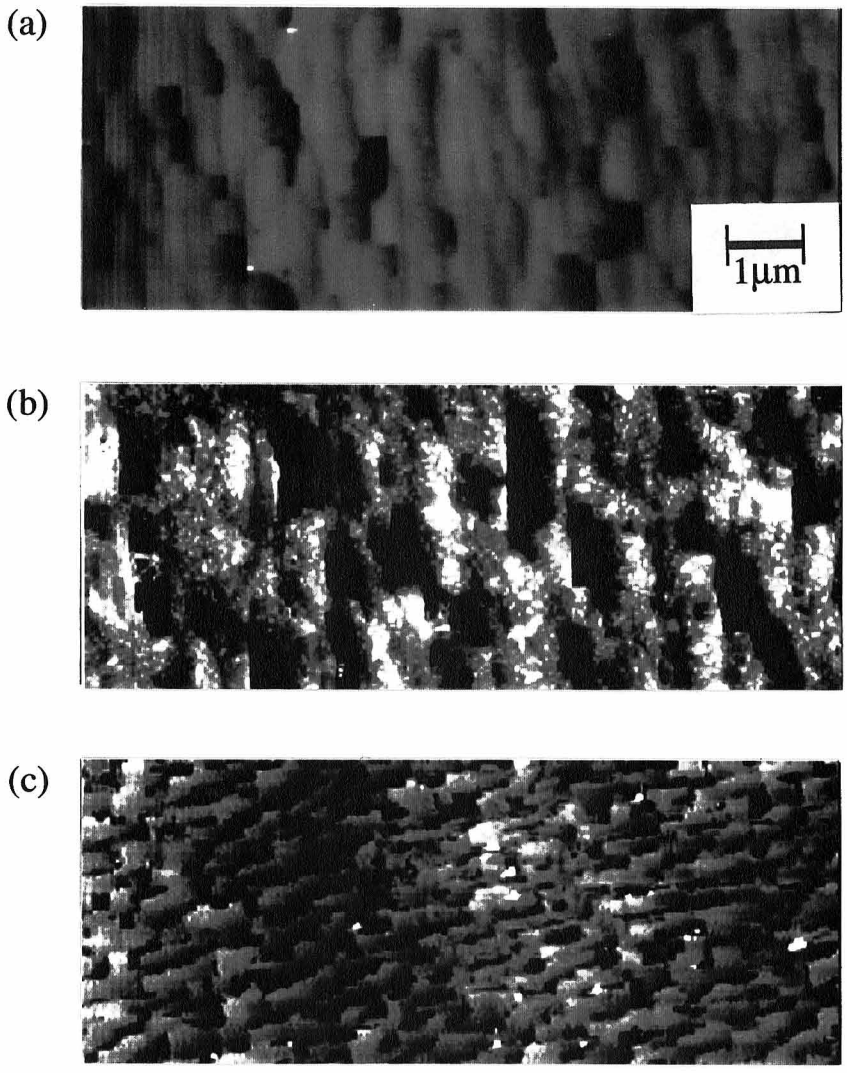

Fig. 2-6 The AFM images of $CaTiO_3$ thin films grown at T_{sub}=700°C and P_{NO2}=1×10^{-3}Pa. They are the images of the samples same with the (a), (b) and (c) of Fig. 2-4, respectively. It is found that the buffer layer of alkaline-earth metal oxides improve the surface morphology of $CaTiO_3$, although the particle separation is caused with respect to the buffer of BaO.

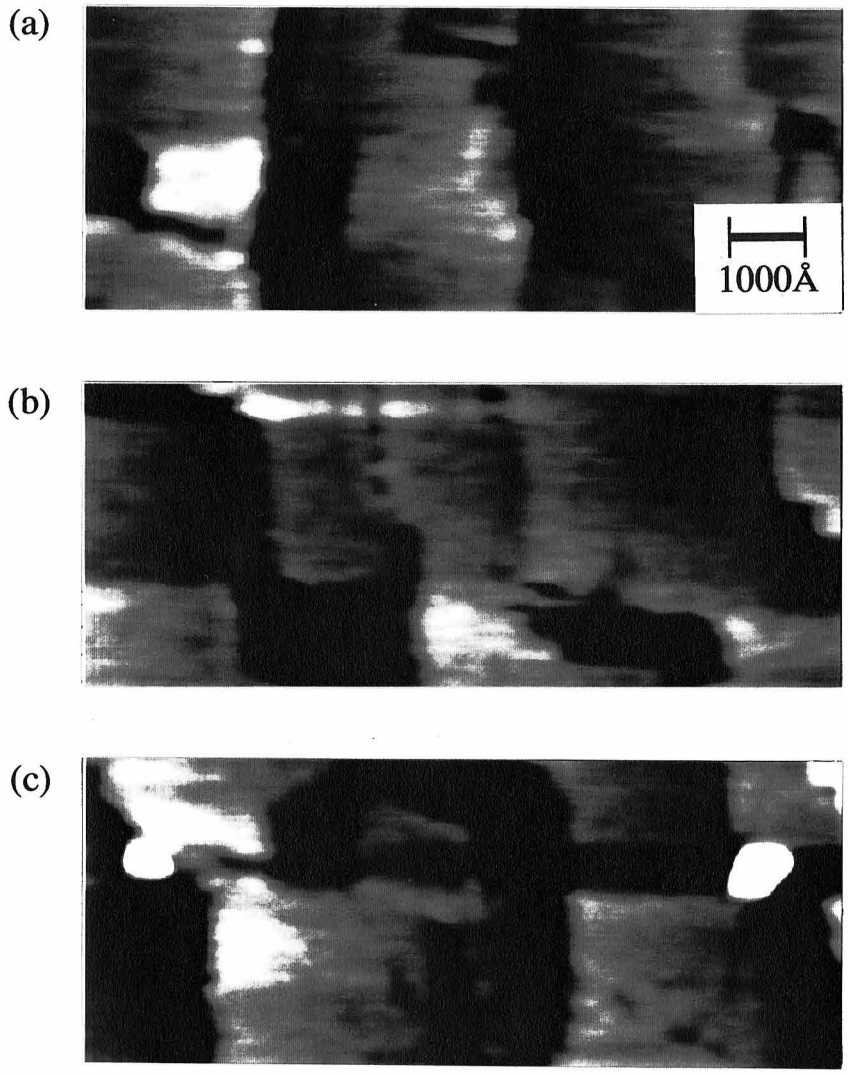

Fig. 2-7 The AFM images of $CaTiO_3$ thin films at T_{sub}=630°C and P_{NO2}=5×10^{-4}Pa. They are the images of the samples same with the (a), (b) and (c) of Fig. 2-5, respectively. By changing the growth condition, the surface smoothness is much improved, while the particle separation is occur on BaO terminated substrate.

$SrTiO_3(100)$ surface. In the comparison of the effect of three types of buffer, SrO gives the best results because there is no particle on the surface and the *in-situ* thickness control can be possible by using RHEED oscillation phenomenon. The retention of surface flatness for the highly lattice mismatched system of $CaTiO_3/SrTiO_3$ (~2.3%) will be a feature of ionic crystal. Namely, ionic bond is more flexible than rigid covalent-bond. This feature is large advantage compared with the highly covalent crystal such as Si and GaAs when the various functional materials are combined as heterostructure.

2-3-3. Growth of $La_{0.7}Sr_{0.3}MnO_3$ and $La_{0.7}Sr_{0.3}MnO_3/CaTiO_3$ bilayer on atomically flat $SrTiO_3(100)$ surface.

In this section, heteroepitaxial growth of $La_{0.7}Sr_{0.3}MnO_3$ and bilayered system of $La_{0.7}Sr_{0.3}MnO_3/CaTiO_3$ are investigated. $La_{0.7}Sr_{0.3}MnO_3$ may have unstableness due to mixed-valence of Mn, but lattice mismatch (~0.38%) with $SrTiO_3(100)$ is smaller than $CaTiO_3$. Thus, it is interesting to compare the results with those of $CaTiO_3$ thin films.

In Fig. 2-8(a), an AFM image is shown for $La_{0.7}Sr_{0.3}MnO_3$ film grown on SrO deposited oxygen-annealed $SrTiO_3(100)$ of type #2. The T_{sub} and P_{NO2} were 630°C and 5×10^{-3}Pa, respectively. The film thickness is 10 unit cell. It is found that the atomically flat surface is kept at the terrace. Furthermore, the oscillation of RHEED intensity can be seen during the

(a)

(b)

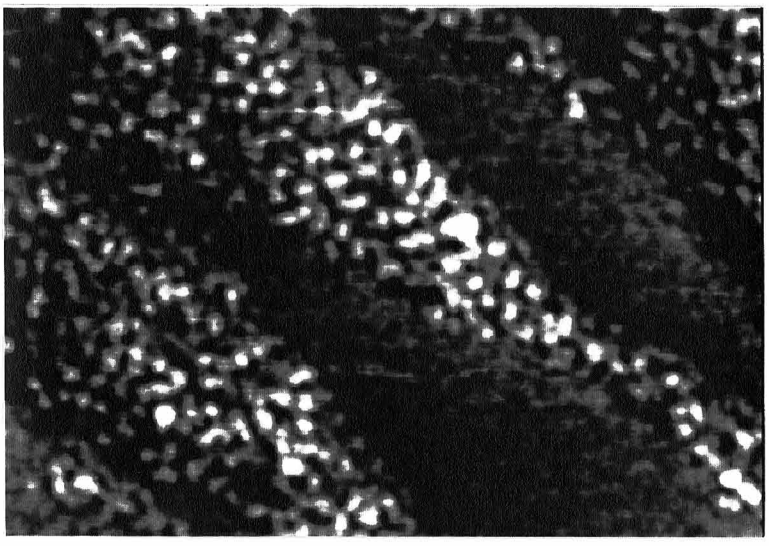

Fig. 2-8 (a) The AFM image of $La_{0.7}Sr_{0.3}MnO_3$ thin films prepared on the oxygen-annealed $SrTiO_3(100)$ of type #2 after the surface termination of SrO buffer layer. The atomically flat surface can be realized for the manganese oxide. (b) The AFM image of $La_{0.7}Sr_{0.3}MnO_3/CaTiO_3$ bilayer prepared on the oxygen-annealed $SrTiO_3(100)$ of type #1 after the surface termination of SrO buffer layer. Many particle can be seen on the terrace while the step structure is kept.

deposition of the film. In this system, i.e., $La_{0.7}Sr_{0.3}MnO_3$ on $SrTiO_3(100)$ substrate, small lattice mismatch will result in the atomic flatness. At the next step, $La_{0.7}Sr_{0.3}MnO_3/CaTiO_3/SrTiO_3(100)$ is prepared in order to study the effect of lattice mismatch. An atomic layer of SrO is also deposited before the growth of $CaTiO_3$ as the buffer. The thickness of each perovskite oxides is 10 unit cell. The T_{sub} was fixed at 630°C, while the P_{NO2} was changed, i.e., 5×10^{-4}Pa for $CaTiO_3$ deposition and 5×10^{-3}Pa for $La_{0.7}Sr_{0.3}MnO_3$ deposition. $CaTiO_3$ thin film grows with flat surface on $SrTiO_3(100)$ in this experimental condition. In this bilayer system, the lattice constant of manganese oxide is larger than that of $CaTiO_3$ and lattice mismatch is about 1.6%. Figure 2-8(b) is the AFM image of $La_{0.7}Sr_{0.3}MnO_3/CaTiO_3$/oxygen-annealed $SrTiO_3(100)$ of type #1. It can be seen that there are many particles with the height of 4~8Å corresponding to 1~2-unit cell of pseudo cubic. Namely, the surface of $La_{0.7}Sr_{0.3}MnO_3/CaTiO_3$ is quite rough than that of $CaTiO_3/SrTiO_3$ nevertheless the lattice mismatch is smaller than $CaTiO_3/SrTiO_3$ system. The result can be considered that the critical lattice mismatch in order to keep the atomically smooth surface is different between $CaTiO_3$ and $La_{0.7}Sr_{0.3}MnO_3$. The reason can be considered as follows. $CaTiO_3$ is the natural mineral, while the manganese oxide is an artificial material where the Mn valence is controlled by the chemical substitution. Thus $La_{0.7}Sr_{0.3}MnO_3$ will be less stable than $CaTiO_3$.

In conclusion, it is found out that small mismatch is the very important point for the preparation of atomically flat $La_{0.7}Sr_{0.3}MnO_3$ thin film.

2-3-4. In-situ monitoring of SrO growth on the atomically flat $SrTiO_3$(100) surface.

As discussed by the previous sections, SrO is the key material for the heteroepitaxial growth of perovskite type oxides with keeping the surface flatness. This important matter is very simple in the viewpoint that only one metal element is contained. Here, the growth process of this simple and important material is studied by *in-situ* RHEED observation as the first step of real-time growth control. In this section, structure and orientation of SrO on completely TiO_2 surface are analyzed by only *in-situ* RHEED pattern observation. Furthermore, the migration process of Sr supplied by laser ablation method is studied by using the time-resolved measurement of RHEED intensity.

First, SrO film is grown on the oxygen-annealed $SrTiO_3$(100) surface. The film thickness is ~100Å. The T_{sub} and P_{NO2} were 500°C and 1×10^{-3}Pa, respectively. During the deposition, an intensity oscillation of RHEED specular beam can be clearly seen just only in the first period. After that, RHEED pattern becomes spotty. It shows that SrO grows with layer-by-layer of only an atomic layer on the oxygen-annealed $SrTiO_3$(100)

and after that, the growth mode changes into islands growth. Namely, the growth mode of SrO is Stranski-Krastanov mode (see Appendix B). Figure 2-9 is the RHEED pattern of the SrO after the deposition. The incident electron beam is parallel to $SrTiO_3$[010] and [011] for Figs. 2-9(a) and 2-9(b), respectively. The very diffuse spots can be seen in both patterns. On the basis of these spotty patterns, the lattice constant and Bravais lattice are identified. Figures 2-9(c) and 2-9(d) are the schematic illustrations of the reciprocal-lattice corresponding to Figs. 2-9(a) and 2-9(b), respectively. It is found that the reciprocal-lattice patterned in the RHEED is a body-centered lattice. Therefore, the real-space lattice of this substance is face-centered lattice. The streak spacing of the RHEED pattern in Figs. 2-9(a) and 2-9(b) correspond to 7.3Å and 5.2Å in real space. The spot spacing along the streak for the patterns in Figs. 2-9(a) and 2-9(b) are 5.2Å. These experimental data show that the grown substance is the face-centered cubic with the lattice constant a of about 5.2Å and the [010] axis of the cubic cell is parallel to $SrTiO_3$[011]. These results agree well with the structure of cubic SrO with rock salt type whose lattice constant is a=5.16Å. Since the experiment was performed in the oxidation atmosphere, it is reasonable that the SrO grows. The atomic configuration along SrO[010] is same with that of the SrO layer in $SrTiO_3$ along the [011] direction. On the basis of above consideration, it is proved that the crystal structure, orientation and lattice constant of the grown substance are

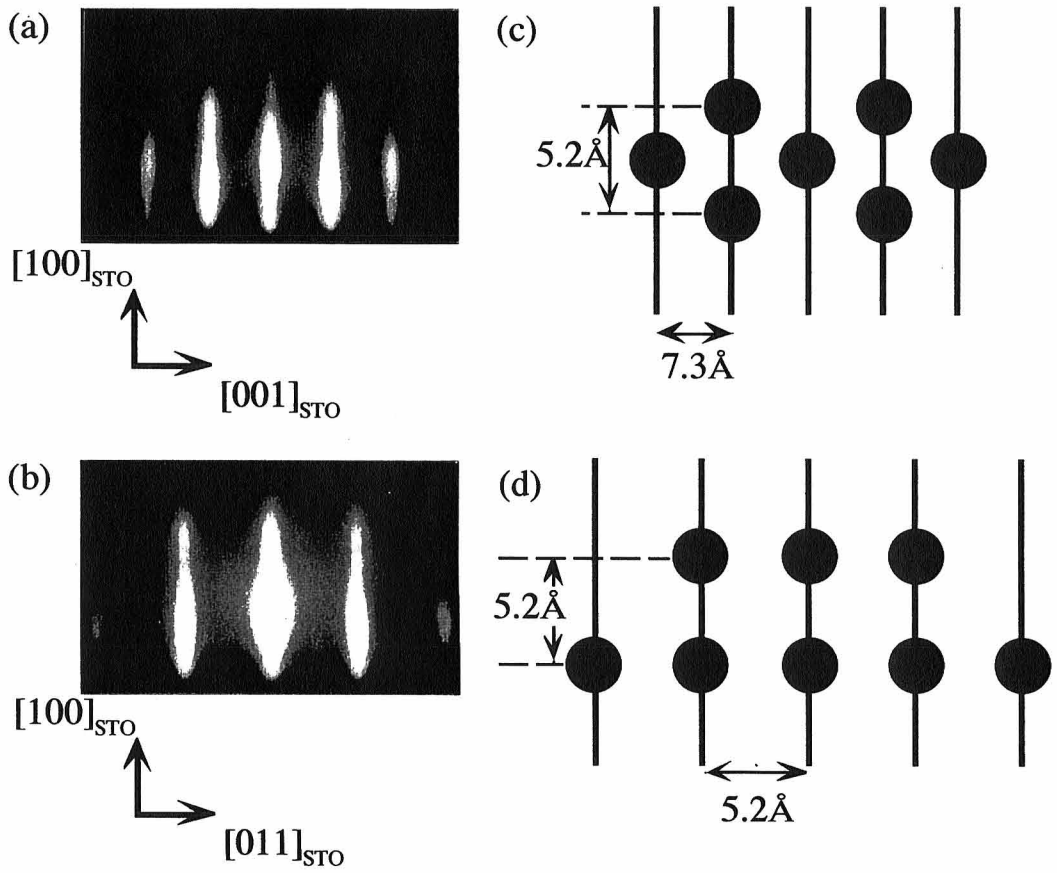

Fig. 2-9 RHEED patterns and its schematic illustrations of SrO with the thickness of ~100Å on the oxygen-annealed $SrTiO_3$(100). The incident direction of electron beam is [010] (a) and [011] (b), respectively. The (c) and (d) are schematic diagrams of reciprocal lattice corresponding to (a) and (b), respectively.

clarified by using only RHEED.

Figure 2-10 shows the time-resolved measurement of intensity variation of RHEED specular beam with the sampling interval of 50ms. The T_{sub} and P_{NO2} were 400°C and 1×10^{-3}Pa. The incident beam of RHEED is parallel to $SrTiO_3$[010]. The arrow mark shows the time of laser shot. The rapid decrease occurs at the same time with the laser shots and the exponential increase occurs just after the laser shots. The reason for the intensity decrease is that the substance just after arriving at the substrate is randomly deposited on the surface, i.e., there is no periodicity. Concerning the following recovery of RHEED intensity, Achuntharaman et al. have pointed out that the intensity increase has to be associated with the rearrangement of material by means of migration from a lower coordination site to a higher coordination site [11]. This idea agrees with a model where the increase of RHEED intensity is proportional to the decrease of the step density [12], because the step density of surface decreases with this process. Here, we assume that the atom and ion deposited by the ablation affect the RHEED intensity in similar manner with the surface step [13]. Thus, the variation of ([step] + [deposited material]) should be discussed during the crystal growth. The square bracket means its density. Deposited Sr atoms crystallize by two manners, one is combination with step site of the substrate and the other is construction of two-dimensional islands. Since the edge of the two-dimensional islands is

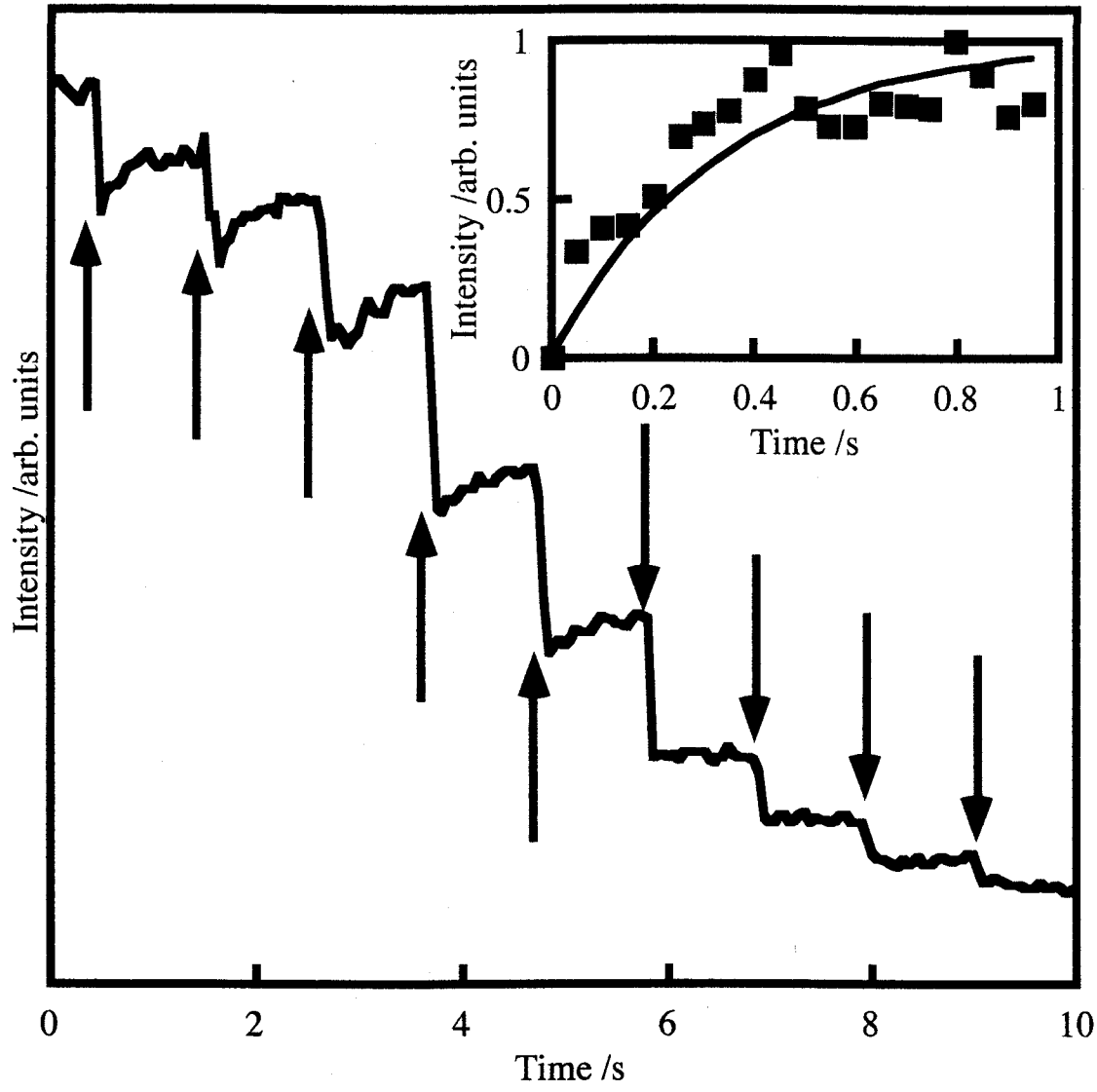

Fig. 2-10 Time-resolved measurement of RHEED intensity during the deposition of SrO. The sampling rate is 50ms. The arrow marks correspond to the laser shots. It can be seen that the rapid decrease is occurred at the same time with the laser shot followed by exponential increase. The inset is the fitting of the intensity variation corresponding to the first laser pulse by the equation, i.e., $I = I_0(1\text{-}e^{-k't})$.

step site, the Sr combination with two-dimensional island is same with the first manner above mentioned. Namely, the crystal growth proceeds by the atom capture at step sites except for the initial stage when the islands are constructed. The number of step site is, however, not changed by the Sr combination with step site. It is found that only [deposited material] should be treated in following discussion. The frequency of Sr combination with step site will be proportional to both densities, i.e., [step] and [deposited Sr]. Above consideration is summarized as following equation of reaction rate.

$$-\frac{d[a]}{dt} = k[S][a] \tag{2-1}$$

Where $[a]$ is the density of materials, $[S]$ is the density of step (constant) and k is the rate constant. The solution is following with $k[S] = k'$.

$$[a] = [a]_0 e^{-k't}. \tag{2-2}$$

The $[a]_0$ is Sr density just after the completion of small islands construction. As discussed above, variation of intensity of RHEED is proportional to that of $[a]$. The variation of $[a]$ is,

$$[a] - [a]_0 = -[a]_0(1 - e^{-k't}). \tag{2-3}$$

Thus, the RHEED intensity, $I(t)$, is,

$$I(t) = I_0(1 - e^{-k't}). \tag{2-4}$$

The experimental RHEED intensity is fitted by Eq. (2-4) for T_{sub}=350°C, 400°C and 450°C using the fitting parameter k'. Arrhenius plot is shown

in Fig. 2-11. The linear relationship in the graph shows that this fitting is reasonable. Since the slope of this plot is $(-E_a/k_B)$, the activation energy E_a for the migration on surface can be calculated. As the result, E_a is found to be 6.0×10^{-2}eV. This energy corresponds to the potential barrier for hopping of Sr from an Sr site to the neighboring site, i.e., related to the reconstruction of the chemical bond from a site to the neighboring. The activation energy of 6.0×10^{-2}eV for is quite small compared with Ga migration on GaAs (more than 1eV) [13]. The large difference of the actiovation energy is not from the binding energy between the adsorbed atom and the surface. The binding energies of Sr-O seems be comparable to or larger than that of Ga-As by the estimation using the decomposition temperature of the crystal as the guide. The melting point of $SrTiO_3$ is ~1900°C and the sublimation point of As for the GaAs is 1238°C (Here, the first layer of SrO on $SrTiO_3$ can be regarded as homoepitaxy. Thus the data of $SrTiO_3$ was used for the comparison). The origin of this difference will be the stress of the chemical bond between the migration atom and the surface during the reconstruction of the chemical bond. When the Ga atom migrates on GaAs, covalent Ga-As bond has large distortion with respect to the bond length and bonding angle. Since covalent bond is strict, the activation energy is large. In the relatively ionic system of $SrO/SrTiO_3$, the isotropic bonding nature will lower the activation energy of migration (Fig. 2-12).

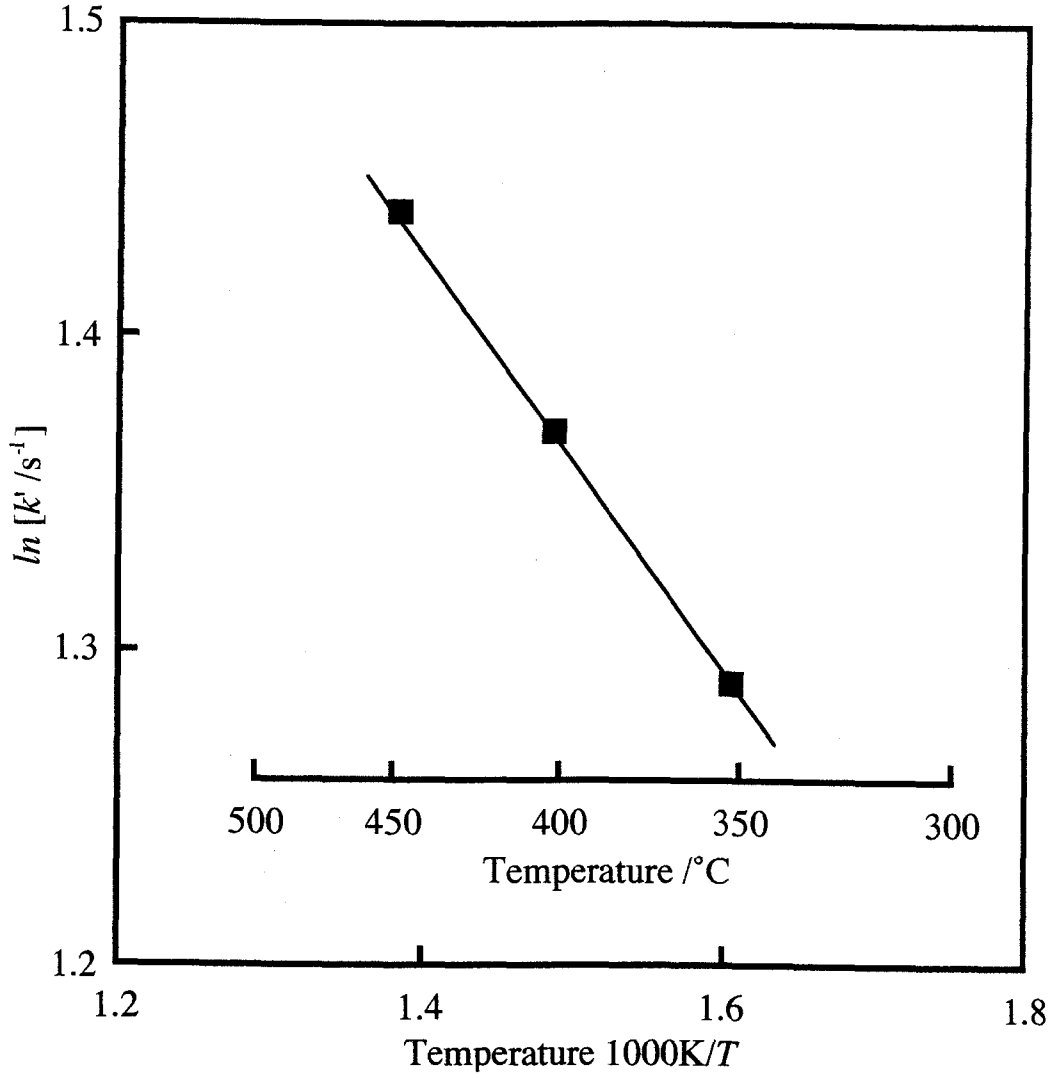

Fig. 2-11 The Arrhenius plot for the rate constants by curve fitting with Eq. (2-4). It is found that the activation energy of Sr migration is 6.0×10^{-2}eV.

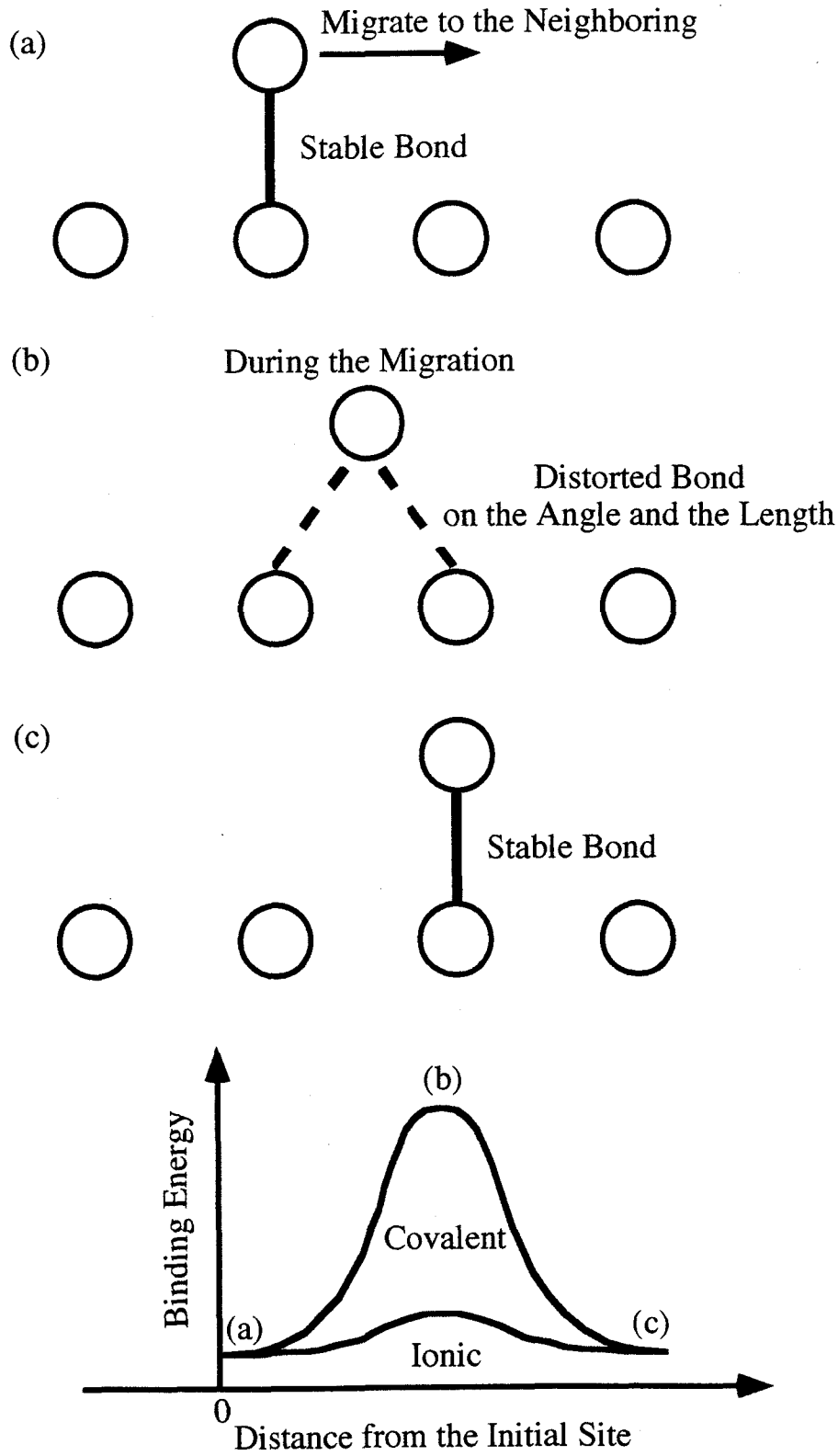

Fig. 2-12 During the migration, the chemical bond is distorted . The angle distortion increases the energy of covalent bond.

2-4. Conclusion.

In summary, the surface morphology has been investigated during the heteroepitaxy of perovskite-type oxides, i.e., $CaTiO_3$ and $La_{0.7}Sr_{0.3}MnO_3$, on atomically flat $SrTiO_3(100)$ surface by using RHEED and AFM as the observation methods. The direct deposition of $CaTiO_3$ on $SrTiO_3(100)$ leads to surface roughening. AO buffer (A=Ca, Sr and Ba) with the thickness of an atomic layer has been effective for improvement of flatness of the film surface. These results indicate that the film growth with the outermost surface of A element is much stable rather than that of B element. RHEED and AFM observation show that the SrO is the most suitable buffer for $CaTiO_3$ on $SrTiO_3(100)$. In the larger lattice mismatch system, $La_{0.7}Sr_{0.3}MnO_3/CaTiO_3/SrTiO_3(100)$, the surface of $La_{0.7}Sr_{0.3}MnO_3$ becomes rough while $La_{0.7}Sr_{0.3}MnO_3$ surface on $SrTiO_3(100)$ with small mismatch system keeps flatness. Namely, severe lattice matching is necessary to obtain atomically flat $La_{0.7}Sr_{0.3}MnO_3$ film compared with $CaTiO_3$. The growth process of SrO thin film has been monitored by using only RHEED. The results of RHEED pattern analysis indicate that epitaxial SrO which has a rock salt structure grows on $SrTiO_3(100)$ substrate. Time-resolved measurement of RHEED intensity has been analyzed from the standpoint of reaction rate. The consideration has revealed that the activation energy of the migration for the system of $SrO/SrTiO_3(100)$ oxygen-annealed is as low as 6.0×10^{-2}eV.

References

[1] For example, S. Hontsu, J. Ishii, H. Tabata and T. Kawai: Appl. Phys. Lett. **67** (1994) 554.

[2] T. Terashima, Y. Bando, K. Iijima, K. Yamamoto, K. Hirata, K. Kamigaki and H. Terauchi, Phys. Rev. Lett: **65** (1990) 2684.

[3] M. Kanai, T. Kawai and S. Kawai: Appl. Phys. Lett: **58** (1991) 771.

[4] J. G. Bednorz and K. A. Müller: Z. Phys. B **64** (1986) 189.

[5] M. Naito and H. Sato: Physica C **229** (1994) 1.

[6] M. Kawasaki, K. Takahashi, T. Maeda, R. Tsuchiya, M. Shinohara, O. Ishiyama, T. Yonezawa, M. Yoshimoto and H. Koinuma: Science **226** (1994) 1540.

[7] A. Asamitsu, Y. Morimoto, Y. Tomioka, T. Arima and Y. Tokura: Nature **373** (1995) 407.

[8] H. Karl and B. Stritzker: Phys. Rev. Lett. **69** (1992) 2939.

[9] M. Yoshimoto, T. Maeda, K. Shimozono, H. Koinuma, M. Shinohara, O. Ishiyama and F. Ohtani: Appl. Phys. Lett. **65** (1994) 197.

[10] M. Kawasaki, K. Takahashi and H. Koinuma: OYO BUTURI **64** (1995) 1124 [in Japanese].

[11] V. S. Achutharaman, N. C. Chaudrasekhar, O. T. Valls and A. M. Goldman: Phys. Rev. B **50** (1994) 8122.

[12] G. Lehmpfuhl, A. Ichimiya and H. Nakahara: Surf. Sci. **245** (1991) L159.

[13] Many Monte-Carlo simulations have also treated "deposited materials" as the step sites. Such as, T. Shitara, D. D. Vvedensky, M. R. Wilby, J. Zhang, J. H. Neave and B. A. Joyce: Phys. Rev. B **46** (1992) 6815.

Chapter 3

Measurements of Bloch Wall Width via Transport Property in Multilayered System of $CoFe_2O_4/Fe_3O_4/CoFe_2O_4$ Thin Film Crystals.

Abstract

In order to understand the variation of the spin configuration in the exchange coupled magnetic multilayered system, trilayered system of the spinel type structure $CoFe_2O_4/Fe_3O_4/CoFe_2O_4$ has been studied via magnetotransport property. The trilayered system can be prepared with the well-defined interfaces by laser MBE method. The Fe_3O_4 layer is studied with the thickness of 500Å, 1000Å and 1500Å while the $CoFe_2O_4$ layers are all 200Å. The magnetotransport property of the trilayered system including 1500Å Fe_3O_4 layer shows large difference from that of the other two samples, i.e., including thinner Fe_3O_4 layer than 1000Å. The borderline of the behavior, i.e., 1000Å well corresponds to the Bloch wall width for the Fe_3O_4. On the basis of the results, the variation of the spin configuration in the exchange coupled system can be picked up via the magnetotransport property.

3-1. Introduction.

Exchange coupling between two magnetic layers has been very noted since the discovery of the phenomenon [1-3]. In Fig. 3-1, the schematic illustration of the magnetic coupling is shown. In the multilayered system consisting of soft and hard magnetic materials, the exchange interaction through the interface fixes the interface spin of soft magnetic material. The intrinsic exchange interaction in soft layer makes the spin pinning at the interface propagate into the inside of the crystal. The spin pinning near the interface will coerce the spin rotation in the soft layer by the applied magnetic field which is the reverse direction to the spin pinned in the soft layer. Namely, the spin configuration in the soft layer is governed by the spin ordering configuration of the hard layer. Thus, the exchange coupling between soft and hard layer can artificially control the magnetic properties of the multilayered magnetic films. Such control of the magnetic properties has been studied especially from a standpoint of the giant magnetoresistance [4-6] for the applications as a magnetic head. In the previous studies, the control has been succeeded in many multilayered systems. One is a magnetically soft metallic ferromagnet NiFe alloy deposited on an antiferromagnet such as MnFe alloy [4, 7-10]. One of the other example is an antiferromagnet multilayered system of CoO/NiO [11, 12]. In those systems, the whole spin in the soft layer is completely fixed via the exchange coupling between soft and hard layer. The spin in the

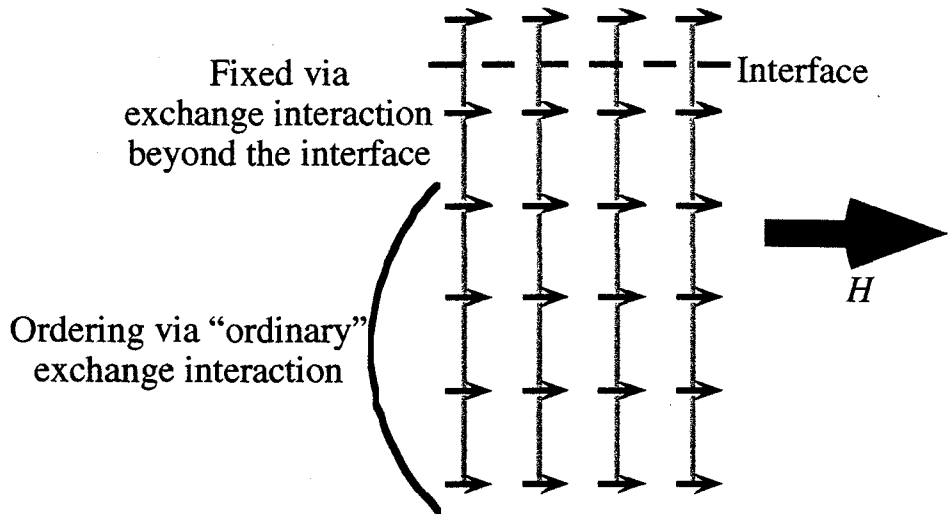

Fig. 3-1 The schematic illustration for the exchange coupling between two magnetic layers in the multilayered thin film. The spin configuration of the interface in the one layer is fixed by the adjacent layer.

inside of the soft layer far from the interface, however, may rotate by the applied magnetic field which is the reverse direction to the spin pinned in the soft layer. Namely, the spin rotation region will be formed in the soft magnetic layer. In the theoretical studies [13-16], it has been predicted that the formation of the spin rotation region is related to the thickness and Bloch wall width of the soft layer. The spin farther from the interface than the Bloch wall width can response freely in the soft layer. Namely, the prediction has claimed that the spin pinning propagation from the interface is limited to the Bloch wall width. This prediction has not been directly proved yet because the measurements of the magnetic properties can not directly "observe" the spin configuration of the crystal inside [17]. If the prediction is correct, however, it can be an important guideline in order to understand the behavior of the exchange coupled system.

For the study of the spin rotation, it is tried that the magnetotransport properties is used. In the ferro- or ferrimagnet, the electric resistance correlates with the magnetization of the crystal because of "spin-dependent scattering" of the carrier [18]. Namely, the resistivity is varied as the order / disorder of the spin configuration in the magnetic field (see Fig. 3-2). The combination of hard insulative magnet and soft conductive magnet makes the spin rotation study be possible via magnetotransport property because the resistivity can be measured for only the soft layer in which the variation of the spin configuration is studied.

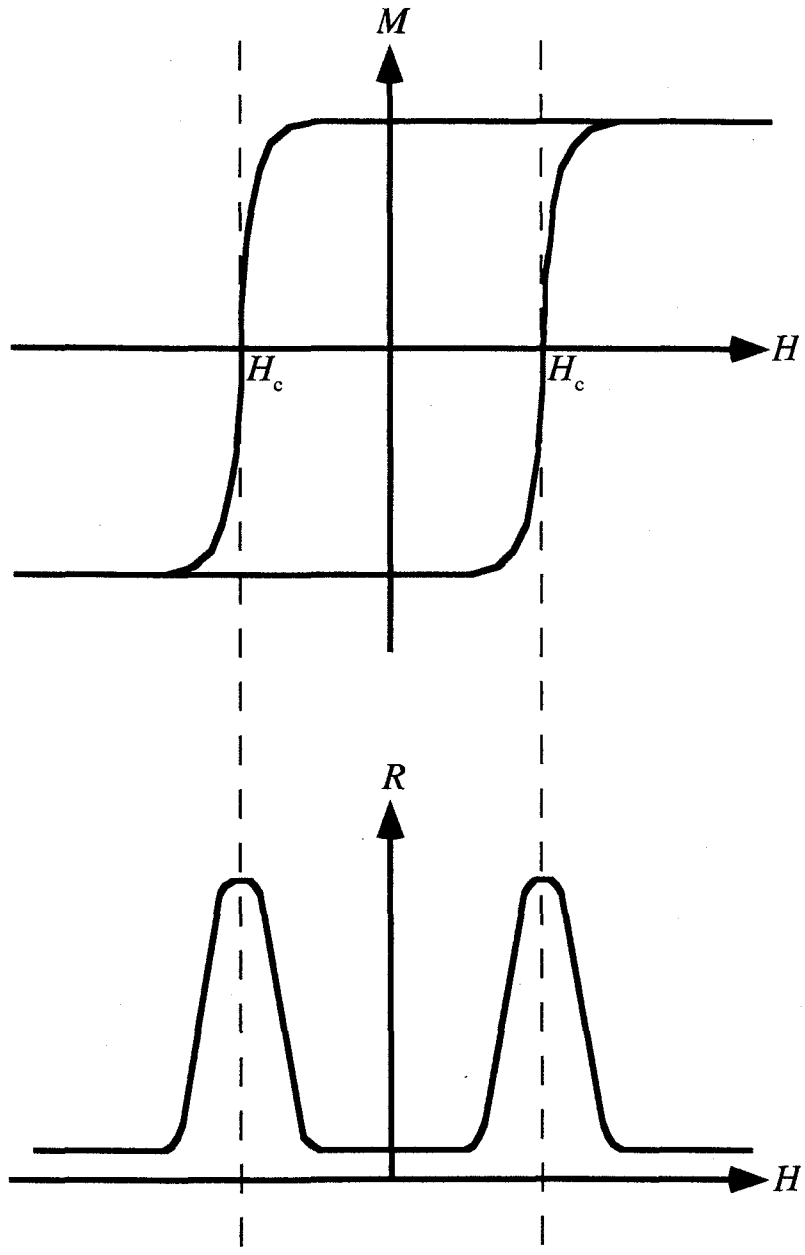

Fig. 3-2 The schematic diagram of the relationship between the resistivity and the magnetization of the ferro- / ferrimagnetic material. At the magnetic field of H_c, the resistivity has maximum because of the most disordered of the spin configuration.

The important factor for the above combination is preparation of the epitaxial multilayer with the well-defined interface since the exchange interaction is a short range [19]. Magnetic oxide material can satisfy the demand while it is impossible for the metallic ferromagnetic multilayered system. The author has chosen Fe_3O_4 as the conductive soft ferrimagnet, i.e., the spin fixed system and $CoFe_2O_4$ as the insulative hard ferrimagnet, i.e., spin pinning system with the spinel type structure (see Fig. 3-3). The very close lattice constant (Fe_3O_4: cubic spinel of a = 8.396Å and $CoFe_2O_4$: cubic spinel of a = 8.3919Å. The lattice mismatch is ~0.05%) of this system is effective for the epitaxial thin film crystals with the well-defined interfaces.

In this study, trilayered system of $CoFe_2O_4/Fe_3O_4/CoFe_2O_4$ has been prepared by laser MBE method in order to try to pick up the variation of the spin configuration in the conductive soft ferrimagnet Fe_3O_4. The spin rotation in the Fe_3O_4 caused by the applied magnetic field may pick up via the magnetotransport property of the Fe_3O_4. Since the Bloch wall width of the single layered crystal of the Fe_3O_4 is ~500Å [16], the behavior of the trilayered system may vary at the thickness for the Fe_3O_4 layer of ~1000Å, i.e., the Bloch wall is formed from the both interfaces. With respect to this trilayered system, the relationship between the thickness of the Fe_3O_4 layer and the Bloch wall formation is discussed on the basis of the results for the magnetotransport property.

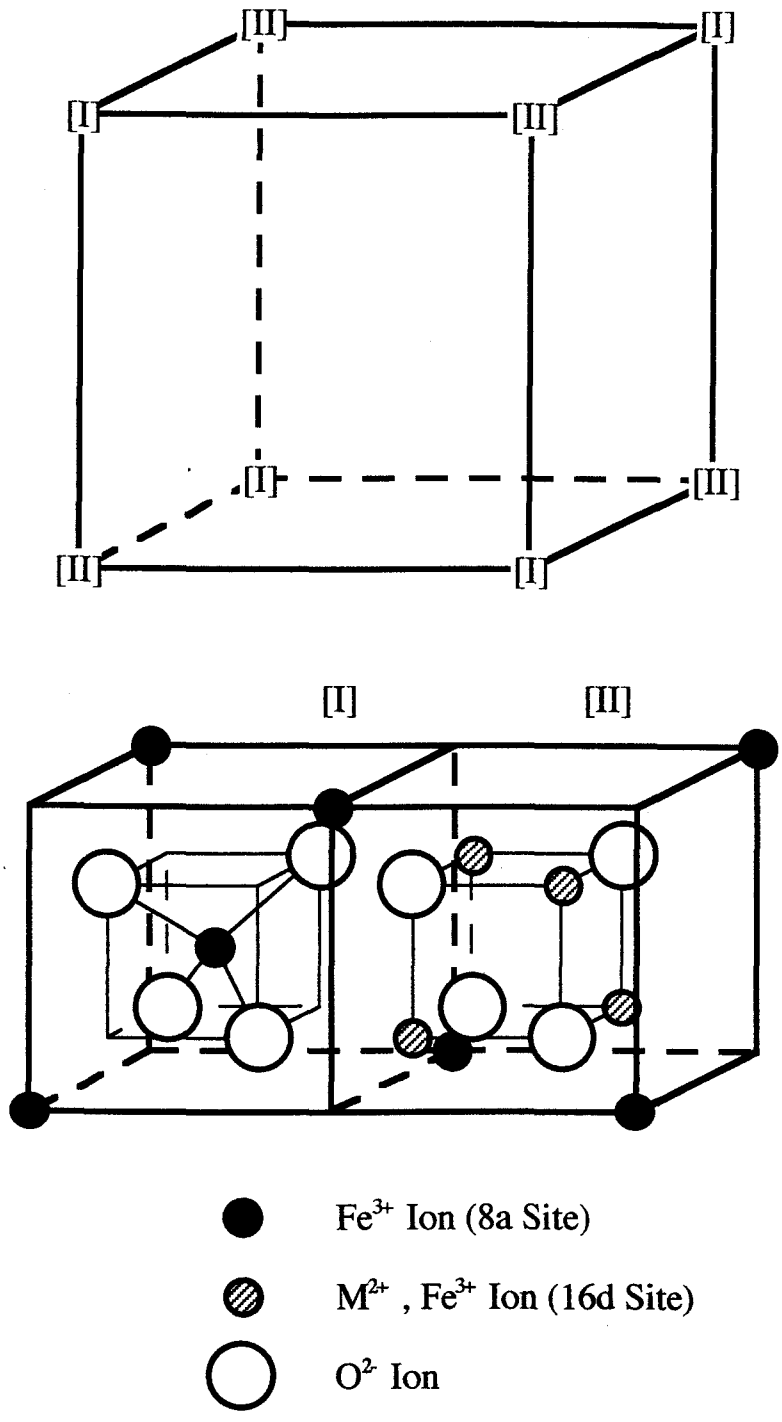

Fig. 3-3 The crystal structure of the spinel type oxide.

3-2. Experimental.

The multilayered thin film crystals were prepared by the laser MBE method in a vacuum chamber (see Fig. 2-1(a)). An ArF excimer laser (Lambda Physics: COMPEX-102, λ=193nm) was used as a light source with the fluence of about 1J/cm^2. The substrates were MgO(100) single crystals (Shinkosha: one side polished). Here, the lattice mismatch is ~0.3% and ~0.4% for the Fe_3O_4 and $CoFe_2O_4$, respectively. During the deposition, the substrate was heated up to the temperature (T_{sub}) of 450°C. The temperature was monitored by an optical pyrometer (Optex: VF-850G). In order to clean the substrate surface, NO_2 gas was introduced to the growth chamber with the pressure of 1×10^{-3}Pa while it was stopped during the growth. The thicknesses of the two $CoFe_2O_4$ layers were fixed at 200Å and that of the Fe_3O_4 layer was 500Å, 1000Å and 1500Å. A RHEED (Tosei Engineering: RHG-1000) with the acceleration energy of 15keV was used for the *in-situ* monitoring of the structure and the morphology for the surface of the films. The RHEED pattern on fluorescent screen was acquired by a CCD camera (Hamamatsu photonics: C3077). The x-ray diffraction apparatus (Rigaku: RAD-RC system, Cu K_α line) was used for the characterization on the structure and orientation of the prepared film by the conventional θ-2θ scanning. Real-space measurement of the surface morphology of the grown film was performed by an *ex-situ* AFM (Digital Instruments: Nanoscope E) in air.

The magnetization-magnetic field (*M-H*) hysteresis loop for the parallel direction to the film surfaces was measured by using a superconducting quantum interference devices (SQUID) (Quantum Design: MPMS-5) with the magnetic field of ±10kOe. The magnetotransport property was measured by the standard four probe technique in the magnetic field of ±10kOe with the direction of the parallel to the film surfaces. The field was applied by electromagnet (Lake Shore: electromagnet system). Both of the *M-H* hysteresis loop and the magnetotransport were measured at 300K, i.e., room temperature.

3-3. Results and Discussion.

3-3-1. Structures and magnetic/transport properties of Fe_3O_4 and $CoFe_2O_4$ single layered thin film crystals.

In this section, the single layered systems of Fe_3O_4 and $CoFe_2O_4$ are studied with respect to the structure and the magnetic/transport properties. Figure 3-4 shows the RHEED patterns for the single layered thin films of Fe_3O_4 and $CoFe_2O_4$. The thicknesses of those films are 500Å and 200Å for the Fe_3O_4 and the $CoFe_2O_4$, respectively. The both pictures show the sharp streaky pattern with the clear specular spot. This means that the qualities of the grown thin films have the good surface flatnesses and the crystallinities. The spacing of the streak, i.e., ~8.4Å^{-1}, well corresponds to the lattice constant of those crystals. In the x-ray

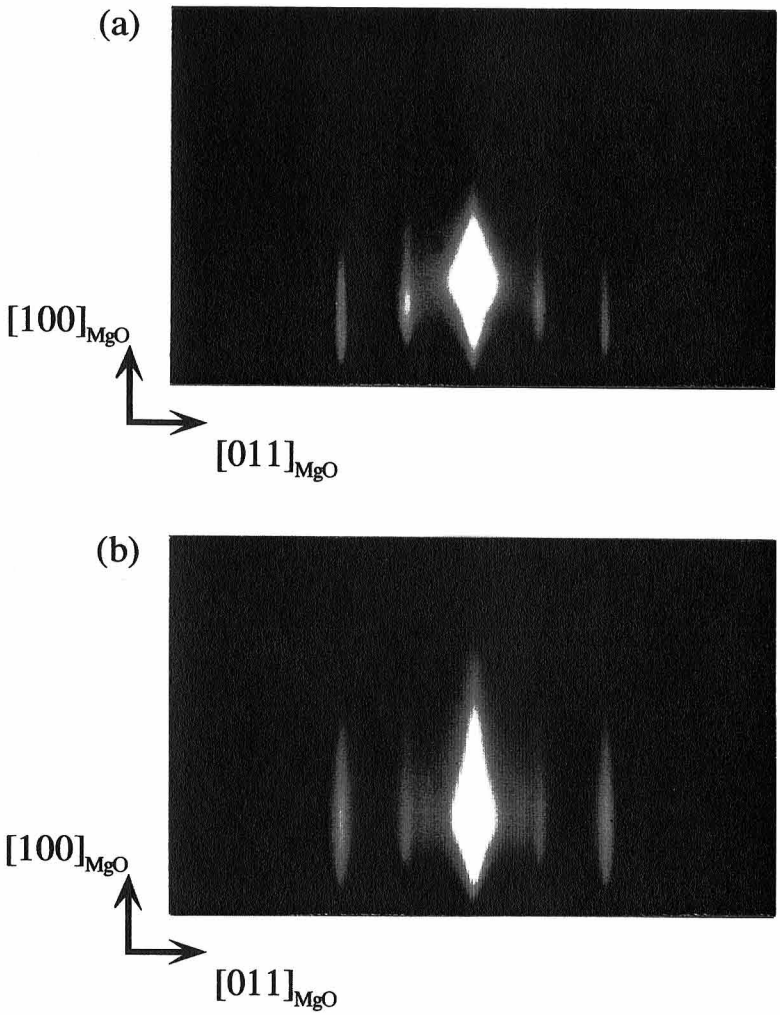

Fig. 3-4 The RHEED pattern of the single layered Fe_3O_4 with the thickness of 500Å (a) and $CoFe_2O_4$ with the thickness of 200Å (b) grown on the MgO(100) substrates. Each pattern has sharp streak and clear specular spot. This means that the qualities of the grown film have good surface flatness and the crystallinities.

diffraction patterns, there are only (1600) peak of the spinel structure for each sample. The (400) peak will overlap the (200) peak of the MgO substrate [20, 21]. From the results of those diffraction techniques, it is found that the Fe_3O_4 and $CoFe_2O_4$ can be prepared on the MgO(100) substrates as the single crystal with the *a*-axis oriented epitaxial thin films. In Fig. 3-5, the AFM images are shown for the same samples. The surfaces are consist of atomically flat terraces. The surface flatness is consistent with the RHEED pattern. Such flatness will be satisfied for the formation of the well-defined interfaces. On the basis of those results, it is considered that the multilayered system consist of such good quality layers will show the intrinsic properties with respect to the interlayer exchange coupling.

Figure 3-6 shows the *M-H* hysteresis loop and the variation of the resistivity as the applied field for the Fe_3O_4, which is the same sample with shown in above. In Fig. 3-6(b), the resistivity is shown as the relative variation to the resistivity at 10kOe, i.e., the most ordered state of the spin. Fig. 3-6(a) shows that the coercive force (H_c) of the sample is ~200Oe. This value is similar to the previous report of the Fe_3O_4 thin film [22]. Furthermore, the magnetotransport property in Fig. 3-6(b) well corresponds to the *M-H* hysteresis loop, i.e., the large variation is caused at the same magnetic field with the large variation of the magnetization. Since the spin configuration is the most disordered state at the field of H_c, it

(a)

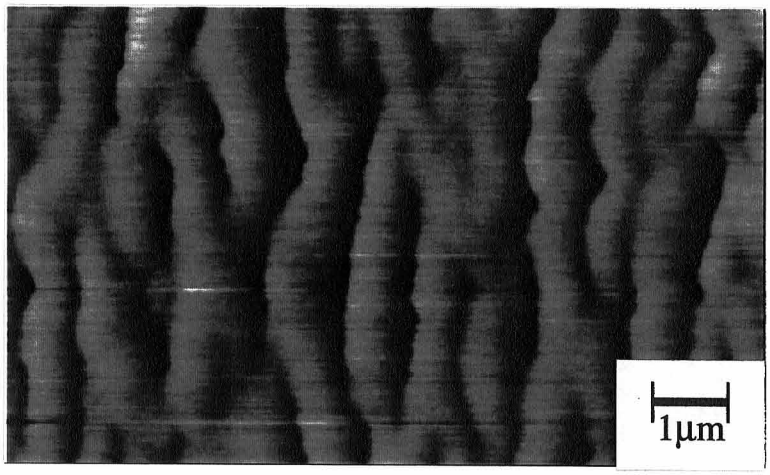

(b)

Fig. 3-5 The AFM images of the single layered Fe_3O_4 (a) and $CoFe_2O_4$ (b). Those are the images of the same samples shown in Fig. 3-4.

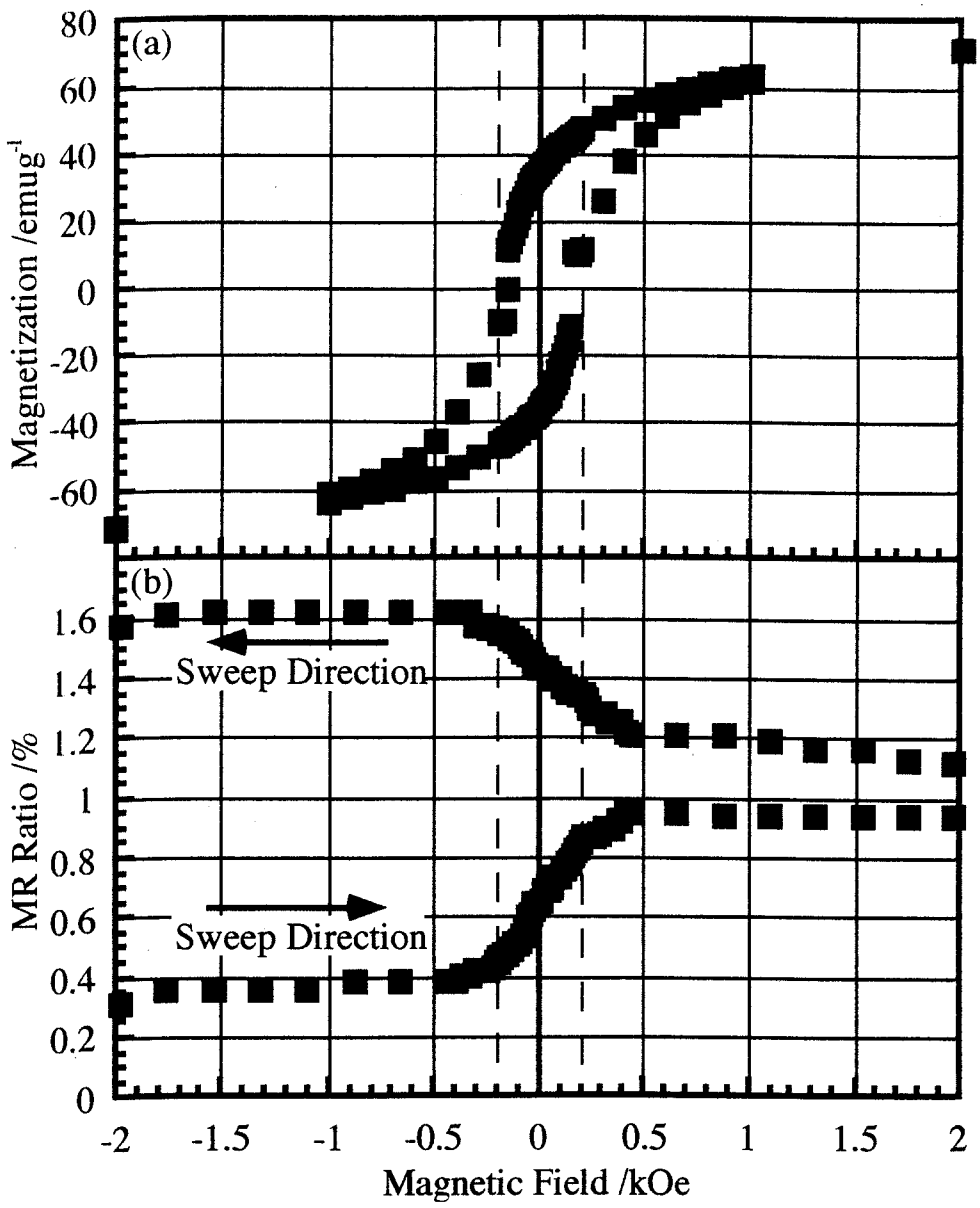

Fig. 3-6 (a) The measured *M-H* hysteresis loop of the single layered Fe_3O_4 thin film crystal. The H_c is ~200Oe. (b) The measured variation of the resistivity in the magnetic field. The vertical axis is shown as the relative variation to the resistivity at 10kOe, i.e., the most spin ordered state. The sweep of magnetic field is ±10kOe while only the result in ±2kOe is shown for (a) and (b). The results of (a) and (b) are shown for the sample that has been evaluated with respect to the structure in Figs. 3-4 and 3-5.

means that the transport property is sensitive to the spin configuration in the Fe_3O_4. The absolute resistivity at 300K is ~$10^{-2}\Omega$cm without applying the magnetic field.

Figure 3-7 shows the *M-H* hysteresis loop of the $CoFe_2O_4$ which is the same sample evaluated with respect to the structure in above. It is found that the H_c of the sample (~500Oe) is low compared to the previous article (~30kOe) [16] while the reason has not been understood. The absolute value is, however, larger than that of the Fe_3O_4 prepared in this study. Since the H_c is one of the most important reference of the magnetic hardness, it is considered that the difference of H_c will fix the spins in the Fe_3O_4. The resistivity of the sample is larger than $10^6\Omega$cm at the zero filed. Such high resistivity does not disturb the measurement of the spin configuration of the Fe_3O_4 in the multilayered system via the magnetotransport property.

In summary of the section, the qualities about the structure and the magnetic/transport properties have been evaluated for the single layered Fe_3O_4 and $CoFe_2O_4$. The surface flatness of each epitaxial single crystal thin film is suitable for the formation of the well-defined interfaces. The magnetotransport property of the prepared Fe_3O_4 is sensitive to the spin configuration in the crystal. The $CoFe_2O_4$ spin at the interface will fix the spin of the Fe_3O_4 because of the larger H_c than that of the Fe_3O_4. The resistivity of the $CoFe_2O_4$ is much higher than that of Fe_3O_4. On the basis

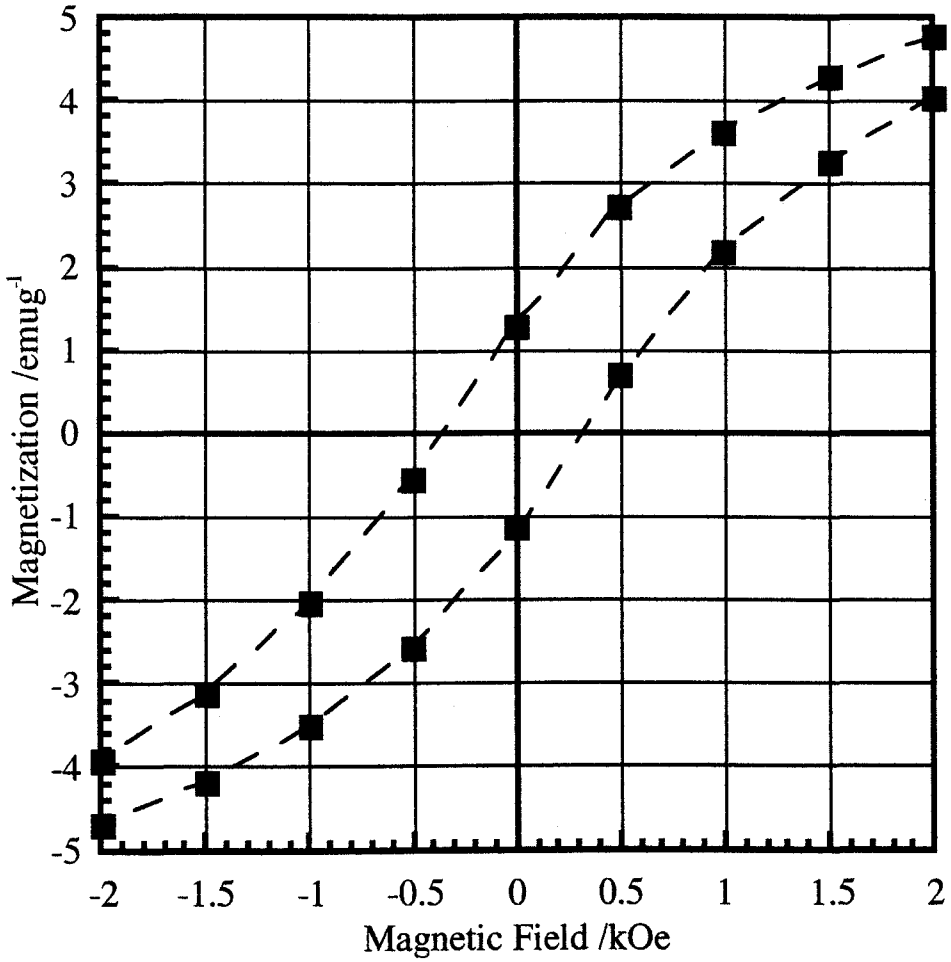

Fig. 3-7 The *M-H* hysteresis of the $CoFe_2O_4$ thin film crystal shown in Figs 3-4 and 3-5. The sweep of magnetic field is ±10kOe while only the result in ±2kOe is shown. The larger H_c than that of Fe_3O_4 is found.

of the results with respect to each single layered system, it is considered that the spin configuration controlled artificially in the trilayered system of $CoFe_2O_4/Fe_3O_4/CoFe_2O_4$ can be investigated via the magnetotransport property of the Fe_3O_4.

3-3-2. The magnetic and magnetotransport properties of the trilayered system of $CoFe_2O_4/Fe_3O_4/CoFe_2O_4$ thin film crystal.

In this section, the magnetic and magnetotransport properties are measured for three types of the trilayered system of $CoFe_2O_4/Fe_3O_4/CoFe_2O_4$, i.e., the thickness of the Fe_3O_4 layer is 500Å, 1000Å and 1500Å while the thickness of all $CoFe_2O_4$ layers are fixed to 200Å.

Figure 3-8 is the *M-H* hysteresis loop of the trilayered system with the thickness of (a) 500Å, (b) 1000Å and (c) 1500Å for the Fe_3O_4 layer, respectively. The H_c of the system becomes smaller as the Fe_3O_4 layer is thicker, i.e., *M-H* hysteresis loop becomes slightly sharp. The "hardness" of the multilayered system seems to vary with the thickness of the Fe_3O_4 layer. If the spin on the Fe_3O_4 interface is fixed by the spin of the $CoFe_2O_4$, the spin of the Fe_3O_4 is hard to rotate with the applied magnetic field because of the magnetic hardness of the $CoFe_2O_4$. The spin in the Fe_3O_4 layer far from the interface is not so strongly influenced by the $CoFe_2O_4$. Thus, the variation of the H_c as the thickness of the Fe_3O_4 layer can be understood.

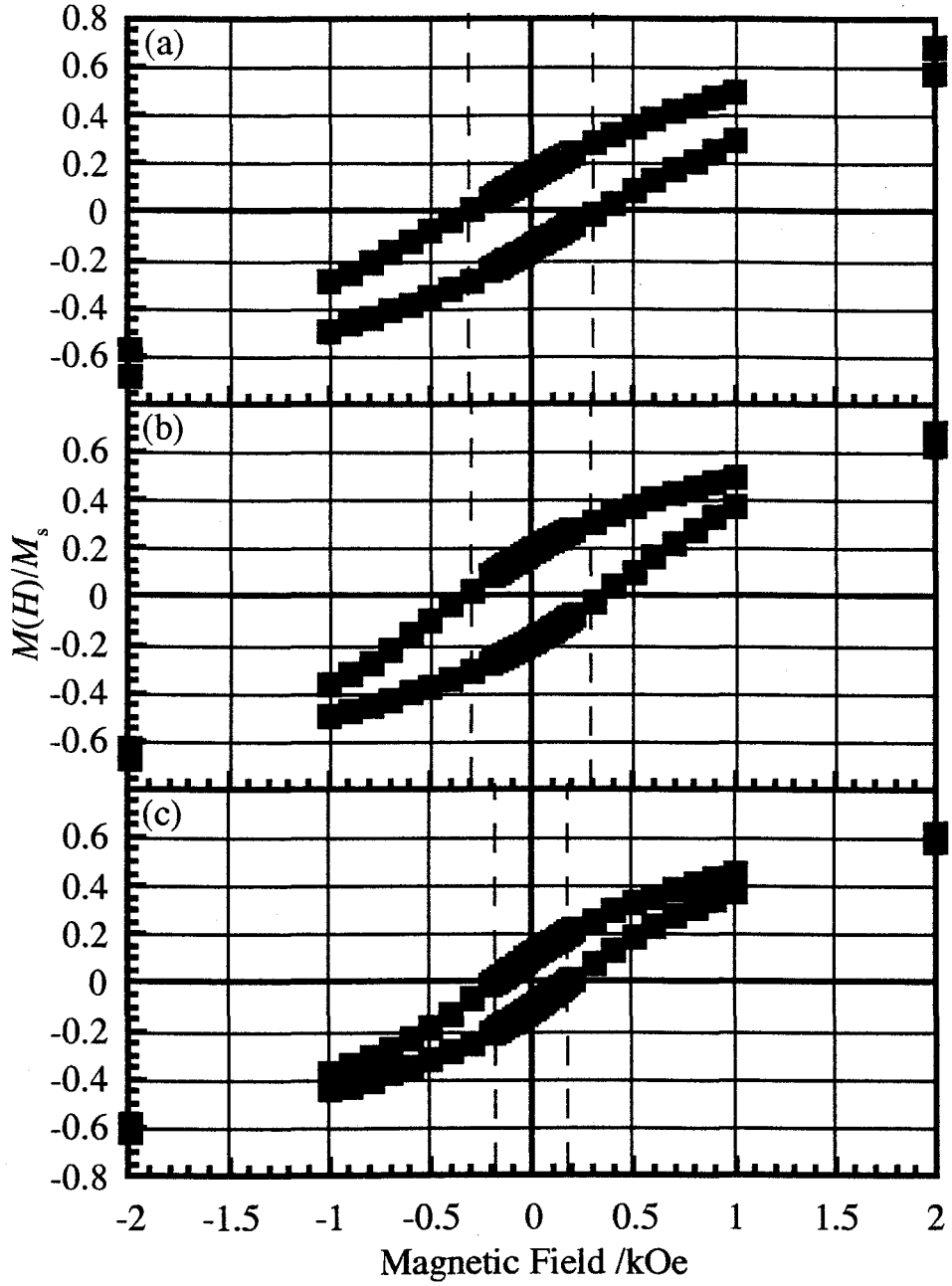

Fig. 3-8 The *M-H* hysteresis loop for the $CoFe_2O_4/Fe_3O_4/CoFe_2O_4$ trilayered system with the Fe_3O_4 thickness of 500Å (a), 1000Å (b) and 1500Å (c), respectively. The sweep of magnetic field is ±10kOe while only the result in ±2kOe is shown. The H_c of the system becomes small as the Fe_3O_4 layer is thicker.

The existence of the spin rotation, i.e., artificial Bloch wall has, however, not been clearly understood in this result. Since the two *M-H* hysteresis loops overlap, namely that of Fe_3O_4 and $CoFe_2O_4$, the variation of the *M-H* hysteresis loop for the trilayered system may occur by means of the property variation of the $CoFe_2O_4$. The magnetotransport property can separate the influence of the $CoFe_2O_4$, because this technique cannot pick up the insulative $CoFe_2O_4$ property.

If the theoretical study [13-16] is correct, the magnetotransport property should show drastic change whether the thickness of the Fe_3O_4 layer is thinner than 1000Å or not. The difference is caused by the formation of the Bloch wall from the both interfaces of the Fe_3O_4 sandwiched by two $CoFe_2O_4$. Since the Bloch wall width of Fe_3O_4 are ~500Å, the trilayered system including the thicker Fe_3O_4 layer than ~1000Å has free spin to the applied field in the inside of the crystal while whole spin is fixed by the $CoFe_2O_4$ in the trilayered system including the thinner Fe_3O_4 than ~1000Å. Namely, the magnetotransport property is independent of the applied magnetic field for the system including the thinner Fe_3O_4 than ~1000Å. In the system that the Fe_3O_4 layer is thicker than ~1000Å, the magnetotransport property will varies as the applied field. In Fig. 3-9, the magnetotransport property of the same sample with Fig. 3-8 is shown. In those results, it is found that the variation of the resistivity as the applied field is quite small in the two samples, i.e., the thickness for the Fe_3O_4 of

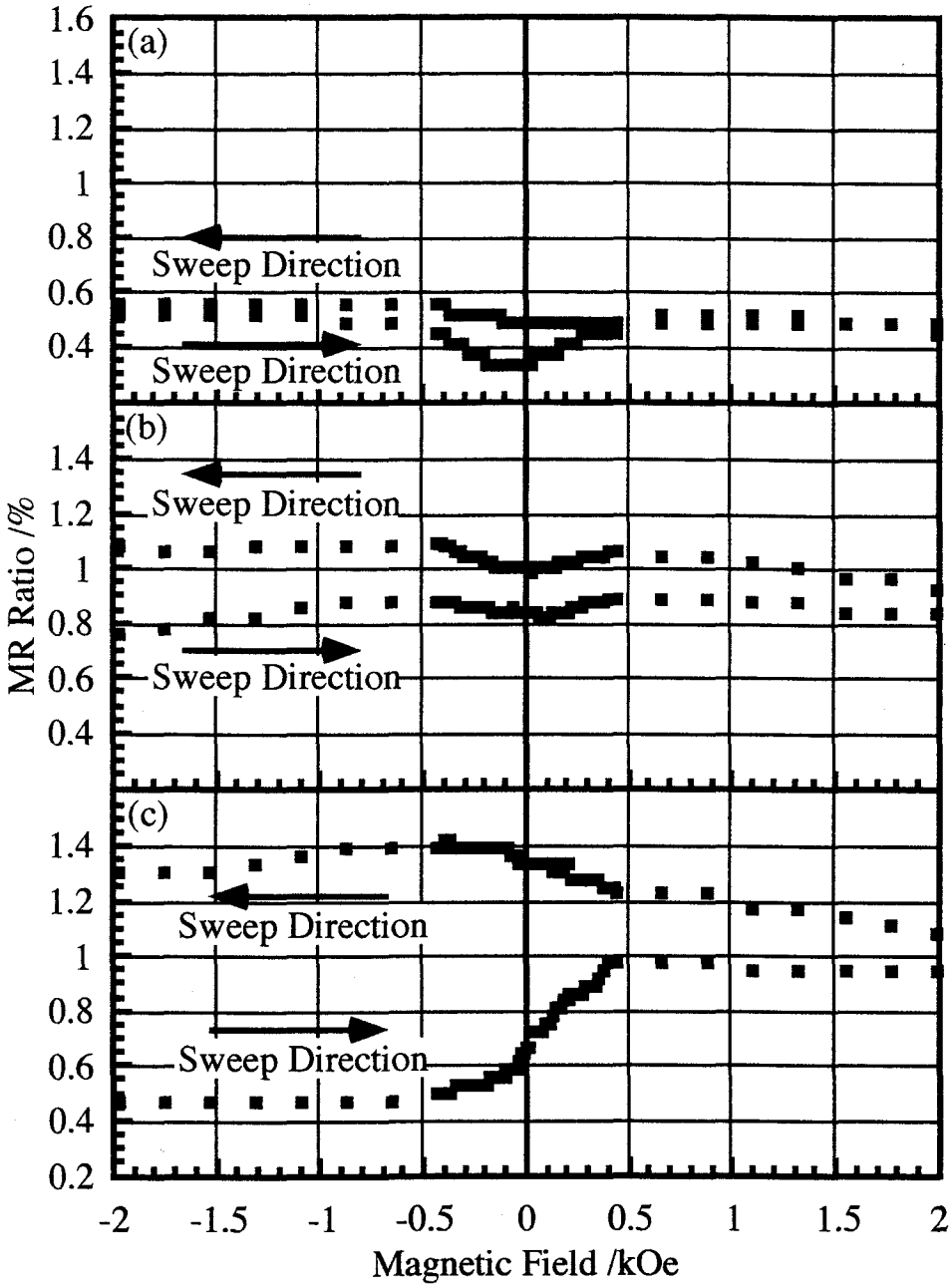

Fig. 3-9 The measured variation of the resistivity in the magnetic field for the $CoFe_2O_4/Fe_3O_4/CoFe_2O_4$ trilayered system with the Fe_3O_4 thickness of 500Å (a), 1000Å (b) and 1500Å (c), respectively. The sweep of magnetic field is ±10kOe while only the result in ±2kOe is shown. The vertical axis is shown as the relative variation to the resistivity at 10kOe, i.e., the most spin ordered state. In (c), the large variation of the resistivity can be seen while that is almost independent of the magnetic field in (a) and (b).

500Å and 1000Å while that for the system including the 1500Å Fe_3O_4 layer shows large dependence on the magnetic field. The variation of the resistivity with the applied field comes from the spin-dependent scattering of the carrier. The result suggests that the spin in the whole Fe_3O_4 crystal is almost fixed independent of the field in the trilayered system with the thickness of 500Å and 1000Å for the Fe_3O_4 layer while the spin can reply to the field for the system including 1500Å Fe_3O_4. On the basis of the result, it is considered that the spin rotation can be caused only in the system including the thicker Fe_3O_4 layer than 1000Å and the whole spin is fixed independent of the field for the system including the thinner Fe_3O_4 layer than 1000Å. Since this value agrees with the twice of the predicted value by the Bloch wall width for the single layered Fe_3O_4 crystal, the magnetotransport property can pick up the formation of the Bloch wall, i.e., the spin rotation region in the inside of the crystal.

The schematic interpretation for the result is illustrated in Fig. 3-10. The influence of the spin pinning by the $CoFe_2O_4$ reaches to the inside of the Fe_3O_4 with the length of about Bloch wall width, i.e., ~500Å from the interface. Thus, the system including the thicker Fe_3O_4 than ~1000Å forms the Bloch wall in the inside of the Fe_3O_4 layer as the applied magnetic field. In this system, the spin-dependent scattering can work effectively, i.e., the magnetotransport varies with the spin rotation. The whole spin in the Fe_3O_4 crystal is, however, fixed for the trilayered system

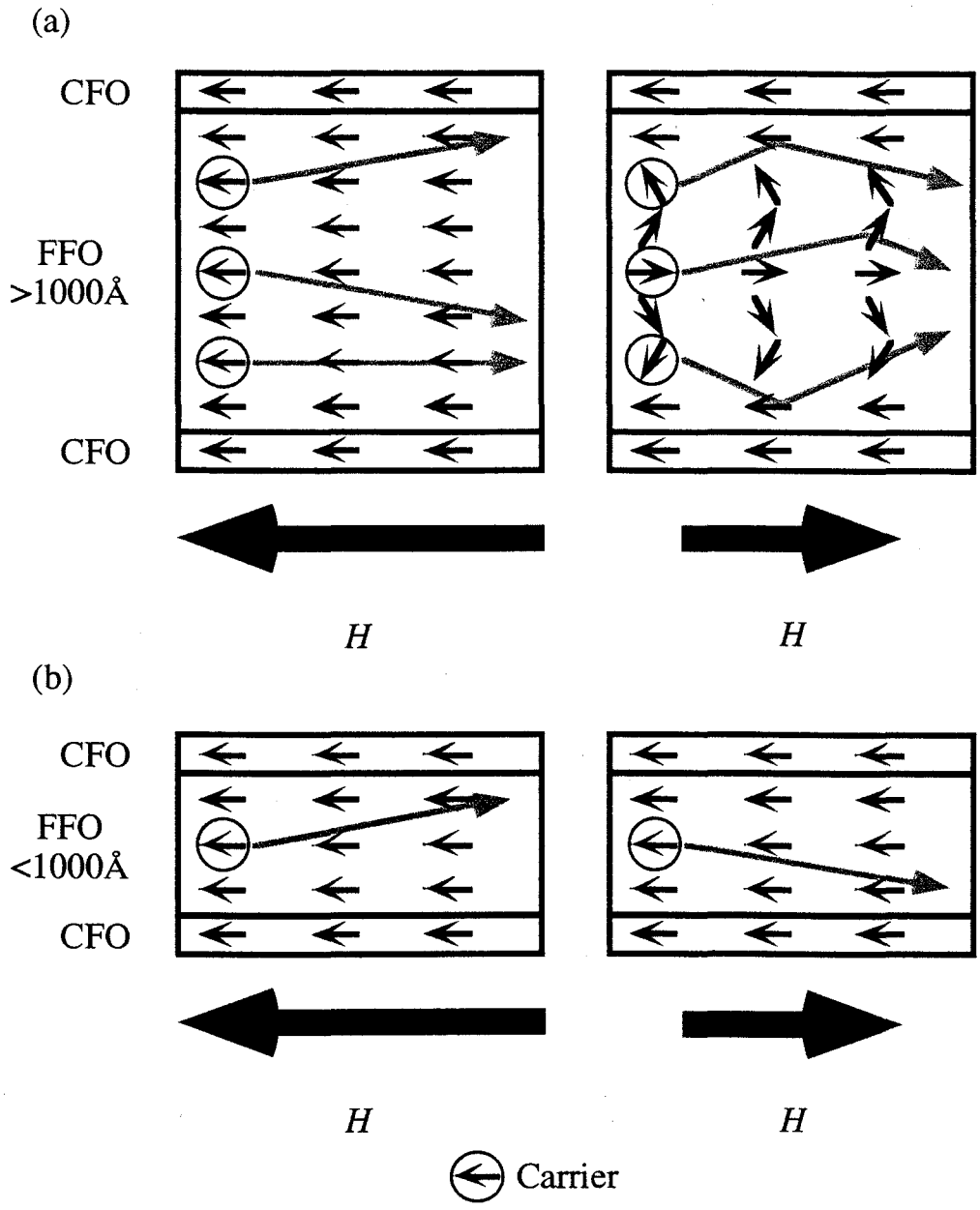

Fig. 3-10 The schematic interpretation for the result in Fig. 3-9. (a) In the thicker Fe_3O_4 layer than the twice of the Bloch wall width, the spin rotation region is formed in the inside of the Fe_3O_4 layer. In such situation, the spin-dependent scattering of the carrier can work. (b) In the thinner Fe_3O_4 layer than the situation (a), the whole spin in the Fe_3O_4 layer is fixed by the $CoFe_2O_4$ layer. Thus, the resistivity is independent of the magnetic field.

with the thinner Fe_3O_4 layer than ~1000Å. In such system, the spin configuration in the Fe_3O_4 is fixed to the same direction to that of the $CoFe_2O_4$ and independent of the applied magnetic field, i.e., the spin-dependent scattering of the carrier does not work effectively.

3-4. Conclusion.

In summary of the chapter, the Bloch wall formed artificially has been tried to pick up via magnetotransport property. The $CoFe_2O_4/Fe_3O_4/CoFe_2O_4$ trilayered thin film crystal prepared by laser MBE method has well-defined interfaces on the basis of the results of RHEED and AFM. On the trilayered systems including the 500Å, 1000Å and 1500Å Fe_3O_4 layer, the magnetotransport property shows clear difference at the 1000Å for the Fe_3O_4 thickness as the borderline. Namely, the resistivity of the trilayered system does not so vary as the magnetic field when the Fe_3O_4 is thinner than 1000Å, while it varies when the Fe_3O_4 is 1500Å . Since the Bloch wall width of the Fe_3O_4 is ~500Å, the behavior of the Fe_3O_4 sandwiched by the $CoFe_2O_4$ agrees well with the formation of the Bloch wall. The result shows that the spin rotation of the conductive magnetic materials can be picked up via magnetotransport property.

References

[1] W. H. Meiklejohn and C. P. Bean: Phys. Rev. **102** (1956) 1413.

[2] W. H. Meiklejohn and C. P. Bean: Phys. Rev. **105** (1957) 904.

[3] W. H. Meiklejohn: J. Appl. Phys. **33** (1962) 1328.

[4] R. D. Hempstead, S. Krongelb and D. A. Thompson: IEEE Trans. Magn. **MAG 14** (1978) 521.

[5] C. Tsang: IEEE Trans. Magn. **MAG 25** (1989) 3672.

[6] W. C. Cain, D. C. Markham and M. H. Kryder: IEEE Trans. Magn. **MAG 25** (1989) 3695.

[7] C. Tsang, N. Heiman and K. Lee: J. Appl. Phys. **52** (1981) 2471.

[8] P. Lambin and F. Herman: Phys. Rev. B **30** (1984) 6903.

[9] N. H. March, P. Lambin and F. Herman: J. Magn. Magn. Mater. **44** (1984) 1.

[10] C. Schlenker, S. S. P. Parkin, J. C. Scott and J. K. Howard: J. Magn. Magn. Mater. **54-57** (1986) 801.

[11] M. Takano, T. Terashima and Y. Bando: Appl. Phys. Lett **51** (1987) 205.

[12] M. J. Carey and A. E. Berkowitz: J. Appl. Phys. **73** (1993) 6892.

[13] E. Goto, N. Hayashi, T. Miyashita and K. Nakagawa: J. Appl. Phys. **36** (1965) 2951.

[14] A. P. Malozemoff: Phys. Rev. B **35** (1987) 3679.

[15] A. P. Malozemoff: J. Appl. Phys. **63** (1988) 3874.

[16] Y. Suzuki, R. B. van Dover, E. M. Gyorgy, J. M. Phillips and R. J. Felder: Phys. Rev. B **53** (1996) 14016.

[17] J. Unguris, R. J. Celotta and D. T. Pierce: Phys. Rev. Lett. **67** (1991) 140.

[18] J. Inoue, A. Oguri and S. Maekawa: J. Phys. Soc. Jpn. **60** (1991) 376.

[19] J. Kanamori: *Magnetism* (Baifu-kan, Tokyo, 1969), p. 53 [in Japanese].

[20] D. M. Lind, S. D. Berry, G. Chern, H. Mathias and L. R. Testardi: Phys. Rev. B **45** (1992) 1838.

[21] S. A. Oliver, C. Vittoria, G. Balestrino, S. Martellicci, G. Petrocelli, A. Tebano and P. Paroli: IEEE Trans. Magn. **MAG 30** (1994) 4933.

[22] D. M. Lind, S. P. Tay, S. D. Berry, J. A. Borchers and R. W. Erwin: J. Appl. Phys. **73** (1993) 6886.

Chapter 4

General Conclusion.

The laser ablation mechanism and its application to the formation of multilayered oxide thin films have been studied in this work. The laser ablation mechanism has been studied as a new subject in the field of photochemistry. In the next, the surface morphology has been controlled with the atomic level for the formation of the high quality multilayered oxide thin films. The exchange coupling system of the ferrimagnetic oxides has been studied with respect to the spin configuration as an example for the advantage of the high quality multilayered oxide thin films.

In chapter 1, the laser ablation mechanism has been studied for three alkaline earth metals of Ca, Sr and Ba. The experiments have been performed with various laser conditions, i.e., wavelength, fluence and effective pulse duration have been varied. In this systematic investigation, the author has found three results which can not be explained by the simple thermal evaporation mechanism. They are, 1: the ion desorption with quite low fluence than that predicted by the thermal evaporation mechanism, 2: the highly nonlinear relationship between the amount of the desorbed ion and the fluence and 3: the termination of the ablation phenomenon within several ns. On the basis of the results, it is concluded that the ablation mechanism of the metal is not simple thermal evaporation mechanism but core electron excitation by multiphoton photochemical reaction. In this work, the studies on the laser ablation mechanism have been developed by means of a new reliable model construction for the metallic bond crystal.

In chapter 2, the *in-situ* RHEED monitoring and the *ex-situ* AFM observation has been performed for the surface morphology control of perovskite type oxides, i.e., $La_{0.7}Sr_{0.3}MnO_3$ and $CaTiO_3$ grown on the atomically flat $SrTiO_3(100)$ by the laser MBE method. During the crystal growth, the important points are the surface stability and the lattice matching. In this study, several conditions have been examined for both surface stability and lattice matching in order to clarify the most suitable condition for the formation of the atomically flat surface. The systematic study with respect to the surface stability has revealed that best condition is the growth on SrO terminated $SrTiO_3(100)$ for perovskite type oxides. The lattice matching is severe for the $La_{0.7}Sr_{0.3}MnO_3$ in which the Mn valence is artificially controlled. In those works, the thin film growth technique of transition-metal oxides has been very improved. This result supports the developments for the formation of many new multilayered or superlattice oxide systems.

Finally, the trilayered system consisting of conductive soft ferrimagnet Fe_3O_4 and insulative hard ferrimagnet $CoFe_2O_4$, i.e., $CoFe_2O_4/Fe_3O_4/CoFe_2O_4$, has been studied with respect to the variation of the magnetotransport property by several thickness of the Fe_3O_4 layer in chapter 3. The result shows large variation with the Fe_3O_4 thickness at twice of the Bloch wall width. The behavior of the Fe_3O_4 sandwiched by the $CoFe_2O_4$ result can be understood as the formation of the Bloch wall

from the both interfaces to the inside of the crystal. In this study, it is proposed that the magnetotransport property can be used as a new technique for the picking up the variation of the spin configuration in the inside of the crystal. This technique will be one of the most powerful tools for the investigation of the spin configuration state.

Throughout the whole investigation, the study for the laser ablation has been progressed not only one of the techniques for the thin film formation but also a subject in the field of physical chemistry. Furthermore, the technique has been developed for the formation of multilayered oxide thin film crystals. On the basis of the results, the author's study has contributed to the realization of harmonic integration of functional oxides by using laser MBE method.

Acknowledgments.

The author expresses his appreciation and gratitude to Professor T. Kawai of ISIR-Sanken, Osaka University for his encouragement and continuous guidance throughout the course of this investigation. The author is very grateful to Dr. M. Kanai for his valuable discussions and helpful suggestions during this study. The author thanks Professor G. Szabo of JATE University for his helpful assistance on "double pulsed laser ablation experiment" in chapter 1. Thanks are due to Assistant Professor H. Tabata of ISIR-Sanken, Osaka University, Dr. T. Matsumoto, Dr. H. Tanaka and Mr. H. Tanaka for their helpful discussions and encouragement. The author is thankful to Dr. J. J. Dubowski for his useful comments on the work in chapter 1. The author wishes to thank students belonging to the laboratory under the direction of Professor T. Kawai of ISIR-Sanken, Osaka University.

Finally, the author expresses his special thanks to Dr. H. Lee, Mr. K. Koguchi and again Mr. H. Tanaka for their assistance both officially and privately.

List of Publications.

1. H. Nishikawa, M. Kanai, T. Kawai and S. Kawai, "Laser-Ablation Mechanism of Sr Metal Investigated by Time-of-Flight Mass Spectroscopy.": Jpn. J. Appl. Phys. **33** (1994) L1090.

2. H. Nishikawa, M. Kanai and T. Kawai, "Laser Ablation of Alkaline Earth Metals Investigated by Time-of-Flight Mass Spectroscopy: Ion Desorption by Core-Electron Excitation.": Jpn. J. Appl. Phys. **35** (1996) L425.

3. H. Nishikawa, G. Szabo and T. Kawai, "Time-Resolved Studies of Ion Desorption from Ca Surfaces Using Double-Pulsed Laser Ablation Technique.": Jpn. J. Appl. Phys. **35** (1996) L985.

4. H. Nishikawa, W. Guan, T. Matsumoto, M. Kanai and T. Kawai, "Mechanism and Dynamics of Laser Ablation for Alkaline Earth Metals.": Trans. IEE of Japan **117-C** (1997) 1213 [in Japanese].

5. H. Nishikawa, M. Kanai and T. Kawai, "Heteroepitaxy of Perovskite-Type Oxides on Oxygen-Annealed $SrTiO_3$(100): Important Factors for Preparation of Atomically Flat Oxide Thin Films.": J. Cryst. Growth **179** (1997) 467.

Appendix A

The Proposed Models for UV Laser Ablation Mechanism.

A-1. Ionic Bond Crystal.

In the low fluence region less than several tens of mJ/cm^2, desorption of the surface atom is caused by the photon irradiation. On the photodesorption condition, "ion desorption by core hole Auger decay mechanism", i.e., Knotek and Feibelman (K-F) model [1, 2], has been believed. The schematic diagram of the model is shown in Fig. A-1. The first process of the desorption is core electron excitation of cation. In this process, the localized charge is produced in a cation site. The excited core hole can not decay via intra-atomic process since there are no valence electron on the cation site. Inactivation process of the core hole starts with the inter-atomic decay from the valence electron on the neighboring anion site. Namely, the localized charge is transferred from a cation site to the neighboring anion site. The next step of the inactivation, the Auger process occurs. The second localized charge on an anion site is produced in the step. At the same time, cascade Auger process is caused with the probability of ~10%, thus the localized (positive) charge may exceed the valence of the anion. After the Auger process, several anions are turned into ions with positive charge. In this situation, the bond between the ion which is originally anion and the neighboring cation will be broken. This is the driving force of the desorption in the mechanism.

In the higher fluence situation, "defect induced ablation mechanism" is reliable for the ionic bond crystals [3]. The experimental

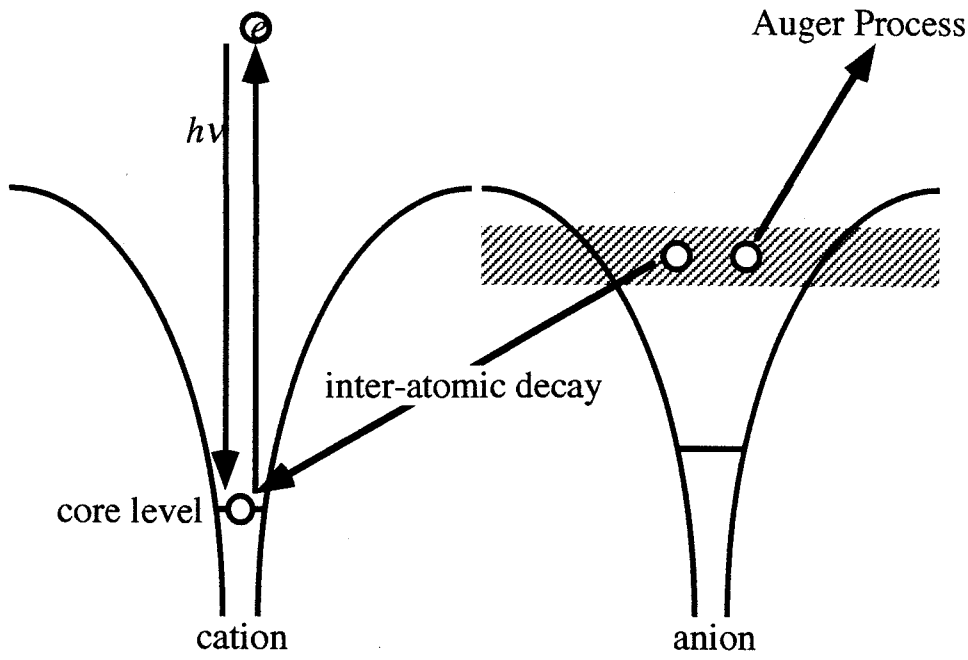

Fig. A-1 The ion desorption by core hole Auger decay mechanism. The core hole produced core hole is decayed via inter-atomic process. The decay causes the Auger process. By means of those processes, two holes are localized on an anion site.

results have shown that the ablation is enhanced by increasing defect near the surface region. The electron in valence band can be excited to conduction band via defect level even if the band gap is larger than irradiated photon energy. Since the hole in the valence band is on the anion site, the driving force of the bond break may be same with K-F model while it is not mentioned in the previous articles.

A-2. Covalent Bond Crystal.

For covalent bond crystal, "electron-hole plasma mechanism" has been proposed [4, 5]. In the nascent process, valence electron excitation by the photon irradiation produces electron-hole plasma. Electron or hole produced in the process can be localized at defect site although such charged particle is conventionally delocalized. With respect to two localized holes, if the Coulomb repulsion force is screened, the holes can be close to each other. The high density electron-hole plasma may results in the screening the Coulomb repulsion. The other mechanism for the approach of two holes is stabilization of electrostatic potential by stretch of the bond between the surface and atom on the hole localized site. The potential curve is shown schematically in Fig. A-2. The one horizontal axis in the diagram indicate the distance r_h between two holes near the surface and the other is Q_R of an atom being ejected from the surface. The vertical axis shows the energy E. The zero point for r_h means that two holes are localized on a

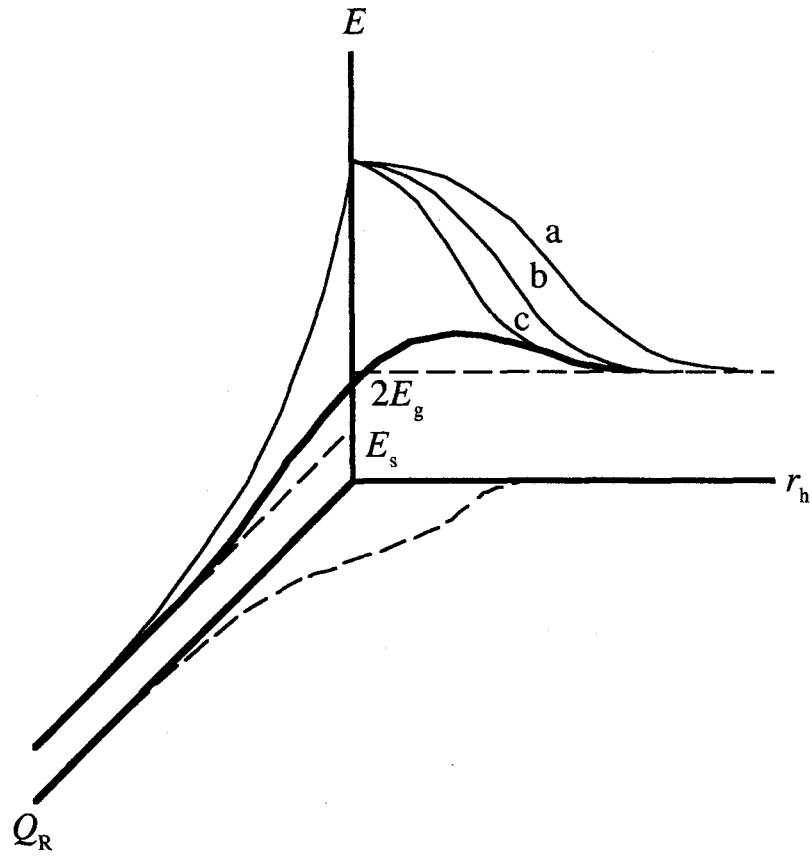

Fig. A-2 The schematic potential curve representing the desorption induced by the two hole localization in an electron-hole plasma. The E-r_h lines, a, b and c at $Q_R = 0$ are the screened Coulomb potential (electron-hole plasma concentration increases in the order a, b and c) and the E-Q_R line represents the desorption potential for the surface atom.

single site. As the distance between two holes decrease, the lattice will start relaxing or an atom start being desorbed from the surface. In terms of the potential curve, this means the transition from the E-r_h valley to the E-Q_R valley. When the density of the electron-hole plasma is high, the two holes may be combined on a single atom as shown by curve (c), inducing the atom desorption.

A-3. Metallic Bond Crystal.

For metal ablation, "thermal evaporation mechanism" is generally believed [6, 7] while the problem has been left in the present stage. The first step of the model is that the excitation of the plasma oscillation in free electron. The plasma oscillation is decayed via the collision to phonon. The time scale of the process is ~ps. Namely, the injected energy to the free electron is transferred to phonon within very fast time of ~ps. Finally, the surface temperature reaches the melting or boiling point.

In the model, the problem is the absorption coefficient of the free electron in metal. Generally, UV laser can transmit the metallic bond crystal. The absorption coefficient is ~10% [8]. The calculation of the target temperature by using such parameter indicates that the fluence more than 1J/cm^2 is needed for the evaporation [7]. The low fluence in which the temperature does not exceed the melting or boiling point, however, can cause the ablation [9].

By means of recognition for above problem, "plasmon excitation mechanism" has been proposed [9, 10]. In this model, the nascent process of the ablation foe metal is excitation of plasmon in the free electron gas, whole the relaxation process and the driving force for the desorption have not been understood at all. The evidence for the proposal of such model is just the agreement between the plasmon energy and the translational energy of desorbed chemical species. Namely, the model has not been established yet. A new reliable model is needed for the ablation mechanism of the metallic bond crystal by systematic experiments.

References

[1] M. L. Knotek and P. J. Feibelman: Phys. Rev. Lett. **40** (1978) 964.

[2] M. L. Knotek: *PHYSICS TODAY SEPTEMBER 1984* (1984) 24.

[3] R. L. Webb, L. C. Jensen, S. C. Langford and J. T. Dickinson: J. Appl. Phys. **74** (1993) 2323.

[4] N. Itoh and T. Nakayama: Phys. Lett. A **92** (1982) 471.

[5] R. F. Haglund Jr.: *AIP Conf. Proc. 288*, eds. J. C. Millor and D. B. Geohegan (American Institute of Physics, New York, 1994) p. 335.

[6] R. W. Dreyfus: J. Appl. Phys. **69** (1991) 1721.

[7] A. Vertes, R. W. Dreyfus and D. E. Platt: IBM J. Res. Develop. **38** (1994).

[8] L. K. Ang, Y. Y. Lau, R. M. Gilgenbach and H. L. Spindler: Appl. Phys. Lett. **70** (1997) 696.

[9] H. Helvajian and R. Welle: J. Chem. Phys. **91** (1989) 2616.

[10] H. S. Kim and H. Helvajian: J. Phys. Chem. **95** (1991) 6623.

Appendix B

Observation of Thin Film Growth by Using RHEED.

B-1. RHEED Pattern of the Typical Surfaces.

The schematic diagram of RHEED observation is shown in Fig. B-1. The RHEED method has a low incident angle of the electron beam in a few degree, so this method is very sensitive to the surface atoms [1]. In Fig. B-2, typical three types of the RHEED patterns are shown [1], i.e., the pattern corresponding to "rough surface" (a), "terraced surface" (b) and "atomically flat surface" (c). The schematic explanations are following.

(a) "rough surface". This surface is characterized by tall three-dimensional islands. The transmission electron diffraction can occur by the islands. The reciprocal-lattice points of the surface represents three-dimensional periodicity of the lattice since the electron observes the crystal as three-dimensional lattice via the transmission process. The Bragg condition can be satisfied at the position where the reciprocal-lattice points and the Ewald sphere intersect. The RHEED pattern consists of spots as shown in Fig. B-2(a).

(b) "terraced surface". In this case, there are flat terraces on the surface. The pattern is dominated by the reflection electron diffraction rather than the transmission diffraction. The reciprocal-lattice points become rod-shape because of the two-dimensionality of the surface (Note that the electron beam can not penetrate so deeply since the incident angle is quite low. This means that the electron beam does not pick up the periodicity with respect to the normal direction to the surface. Thus, the

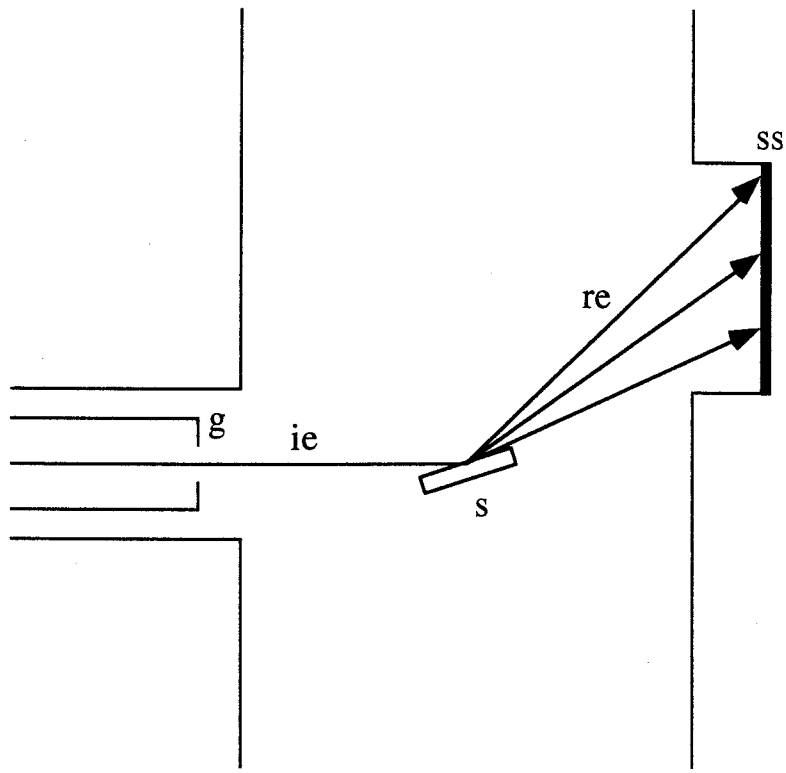

Fig. B-1 Schematic diagram of RHEED observation. Here, g: electron gun, s: sample, ie: incident electron beam, re: reflected electron beam and ss: fluorescent screen.

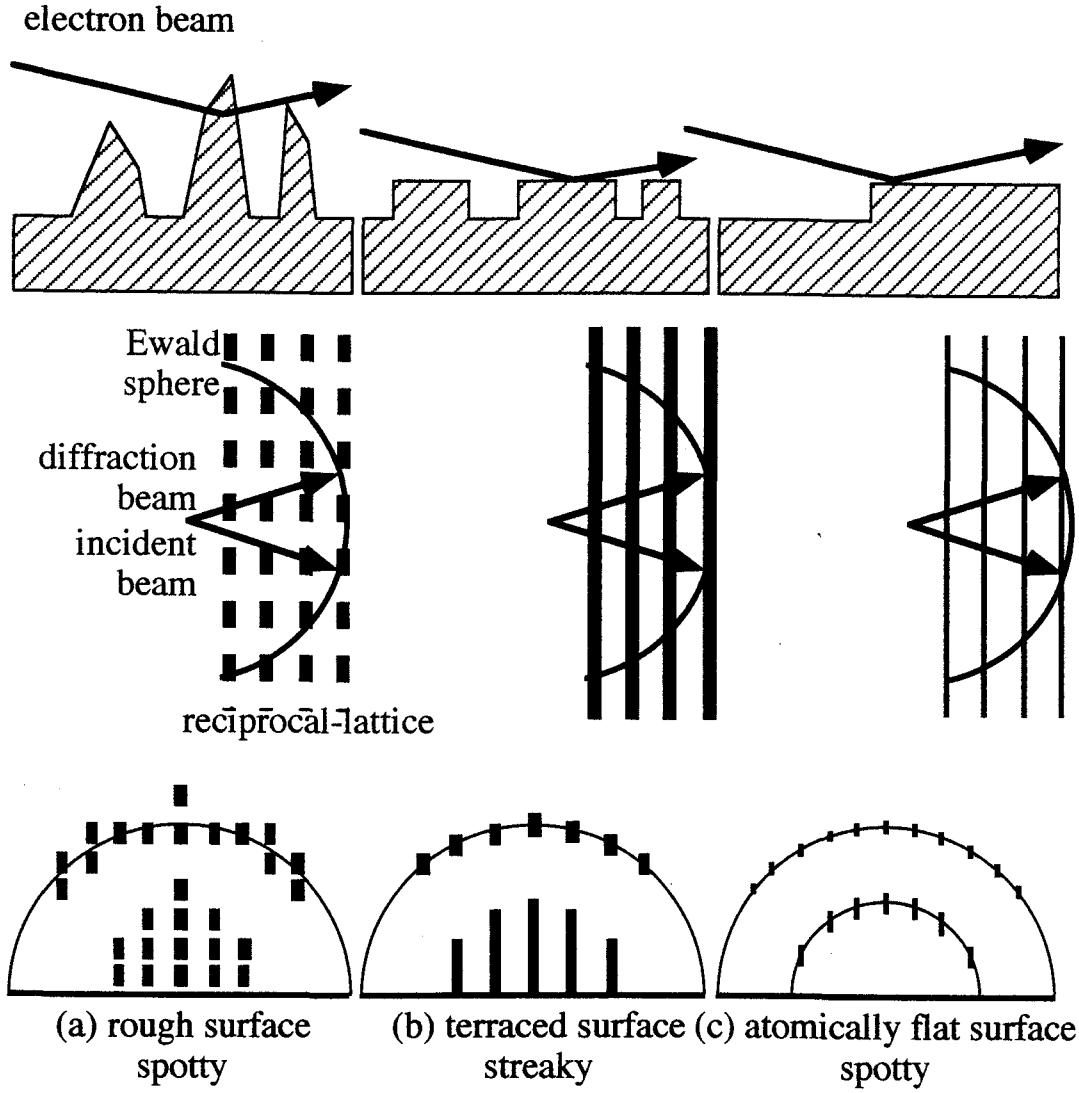

Fig. B-2 The schematic illustrations of typical RHEED patterns. The pattern of "rough surface" consisting of tall islands (a), "terraced surface" consisting of flat terraces separated by step (b) and "atomically flat surface" consisting of large terrace (c).

periodic information is limited to the two-dimension). The rods have finite thickness resulting from the finite area of the terrace. The RHEED shows streaky pattern in the 0th Laue zone and streaky spots in the higher order Laue zones as shown in Fig. B-2(b).

(c) "atomically flat surface". As the surface becomes flat much more than (b), the thickness of the rod in the reciprocal-lattice becomes thinner. Thus, the RHEED pattern varies into spotty just on Laue circles because of the decrease of the overlap between the rod and the Ewald sphere. Figure B-2(c) shows the example of the RHEED pattern in this situation.

B-2. Typical Growth Modes of Thin Film Crystals and Intensity Oscillation of RHEED Specular Spot.

There are three types in the growth mode for thin film crystals, i.e., (a) two-dimensional layer-by-layer growth (see Fig. B-3(a)), (b) three-dimensional island growth (see Fig. B-3(b)) and (c) two-dimensional layer-by-layer growth followed by three-dimensional island growth (see Fig. B-3(c)) [2]. In the mode of (a), the RHEED pattern keeps "terraced surface" pattern because the growth manner in the mode is the repetition of creation of terrace (two-dimensional island) and two-dimensional growth of the terrace. This mode is called "Flank-van der Merwe" mode. The oscillation of RHEED specular spot intensity (RHEED oscillation) is often observed on this growth mode. The refraction model at the step edge as

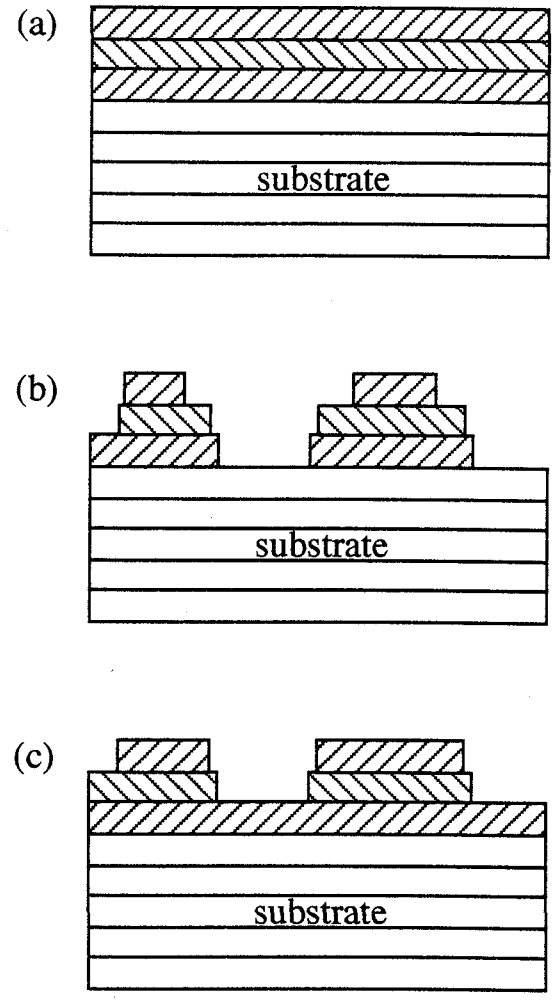

Fig. B-3 Typical three modes for the thin film growth. Two dimensional layer-by-layer mode (a) and three-dimensional growth mode (b) and two-dimensional mode followed by three-dimensional growth (c).

the explanation of the phenomenon [3] is introduced while the mechanism has not been enough established. The schematic illustration for the refraction model is shown in Fig. B-4. Due to refraction by a step, intensity is scattered away from the detector. Since the decrease of the intensity will be proportional to the step density, the periodic variation of the step density during the film growth is observed as the RHEED oscillation. On the mode of (b), the RHEED pattern is "rough surface". This mode is called "Volmer-Weber" mode. With respect to the mode (c), the RHEED pattern varies from "terraced surface" to "rough surface". This mode is called "Stranski-Krastanov" mode. On this growth mode, RHEED oscillation can be observed during the two-dimensional growth.

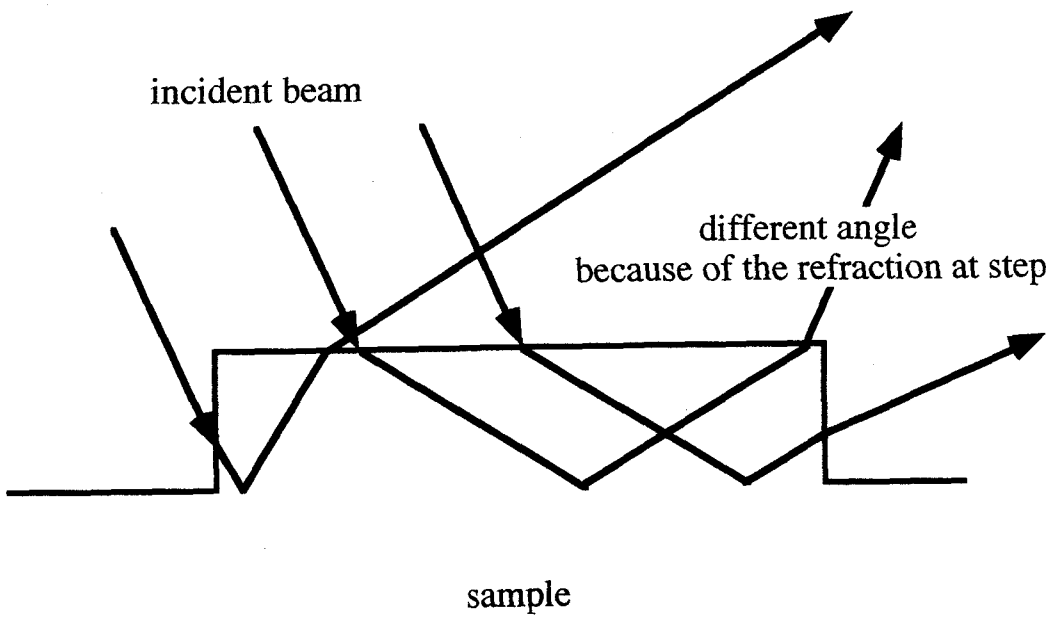

Fig. B-4 Schematic refraction of electron beam path by a step.

References

[1] S. Ino: *Crystallography by Using Diffraction Technique*, ed. S. Hirabayashi (Maruzen, Tokyo, 1981), Chap. 7, p. 307 [in Japanese].

[2] J. S. Horwitz and J. A. Sprague: *Pulsed Laser Deposition of Thin Films*, eds. D. B. Chrisey and G. K. Hubler (John Wiley & Sons, Inc., New York, 1994), Chap. 8, p. 229.

[3] G. Lehmpfuhl, A. Ichimiya and H. Nakahara: Surf. Sci **245** (1991) L159.